SIGNIFICANCE OF HEAT DISSIPATION IN THE CATHODE CATALYST LAYER ON THE LIFETIME AND RELIABILITY OF POLYMER ELECTROLYTE FUEL CELLS

by

Jaimilla Motay

A thesis submitted to the

Department of Chemical Engineering

in conformity with the requirements for

the degree of Master of Applied Science

Queen's University

Kingston, Ontario, Canada

(September, 2016)

Abstract

To study the dissipation of heat generated due to the formation of pinholes that cause local hotspots in the catalyst layer of the Polymer Electrolyte Fuel Cell, a two-phase non-isothermal model has been developed by coupling Darcy's law with heat transport. The domain under consideration is a section of the membrane electrode assembly with a half-channel and a half-rib. Five potential locations where a pinhole might form were analyzed: at the midplane of the channel, midway between the channel midplane and the channel wall, at the channel or rib wall, midway between the rib midplane and the channel wall, at the midplane of the rib. In the first part of this work, a preliminary thermal model was developed. The model was then refined to account for the two-phase effects. A sensitivity study was done to evaluate the effect of the following properties on the maximum temperature in the domain: Catalyst layer thermal conductivity, the Microporous layer thermal conductivity, the anisotropy factor of the Catalyst layer thermal conductivity, the Porous transport layer porosity, the liquid water distribution and the thickness of the membrane and porous layers. Accounting for the two-phase effects, a slight cooling effect was observed across all hotspot locations. The thermal properties of the catalyst layer were shown to have a limited impact on the maximum temperature in the catalyst layer of new fuel cells without pinhole. However, as hotspots start to appear, thermal properties play a more significant role in mitigating the thermal runaway.

Keywords: hotspots, pinholes, two-phase flow, heat transport, thermal conductivity, non-isothermal, anisotropy, sensitivity study

Acknowledgements

Foremost, I would like to thank my supervisor, Dr. Brant A. Peppley, for giving me the opportunity to work on this project to join the fuel cell community. His patience, guidance and support have been invaluable in this work. This research has been made possible through the funding from the Catalysis Research for Polymer Electrolyte Fuel Cells (CaRPE-FC) Network and the NSERC CREATE Program for Distributed Generation in Remote Communities. I greatly appreciate the collaborative environment offered by the community at Queen's University and the fuel cell research group. I am grateful to have Sophie and Nishant, as my family away from home. Finally, I would like to express the deepest gratitude to my parents for their unconditional love and encouragement and to my siblings, Roubeena and Darren, for always being by my side despite the time-zone difference.

Table of Contents

List of Figures

List of Tables

List of Abbreviations

PEFC Polymer Electrolyte Fuel Cell

CL Catalyst layer

CCL Cathode Catalyst layer

ACL Anode Catalyst layer

PTL Porous Transport layer

MPL Microporous layer

ML Membrane layer

MEA Membrane Electrode Assembly

PTFE Polytetrafluoroethylene

HOR Hydrogen Oxidation Reaction

ORR Oxygen Reduction Reaction

RH Relative Humidity

Nomenclature

[-] No Unit

ρ Density [kg/m^3]

$\rho_{dry,mem}$ Density of dry Nafion membrane [kg/m^3]

μ Dynamic Viscosity [Pa·s]

C_P Specific heat capacity [J/(kg K)]

ε Volume fraction [-]

u Velocity [m/s]

k Thermal conductivity [W/ m K]

T Temperature [K]

λ Water Content (ratio of the number of water molecules to the number of charged sites in the Nafion)[-]

$Q_{rev,ACL}$ Reversible heat source at ACL [W/m^3]

$Q_{rev,CCL}$ Reversible heat source at CCL [W/m^3]

$Q_{irrev,ACL}$ Irreversible heat source at ACL [W/m^3]

$Q_{irrev,CCL}$ Irreversible heat source at CCL[W/m^3]

ΔS_{ACL} Entropy change at ACL[J/mol K]

ΔS_{CCL} Entropy change at CCL[J/mol K]

δ_{ACL} Thickness of ACL[m]

δ_{CCL} Thickness of CCL[m]

η_{ACL} Overpotential at ACL[V]

η_{CCL} Overpotential at CCL[V]

α_a Transfer coefficient at Anode[-]

α_c Transfer coefficient at Cathode[-]

j Current density[A/m^2]

j_o Exchange Current density [A/cm^2]

n Number of moles of electrons transferred [-]

F Faraday's Constant [C/mol

V_o Thermodynamic potential [V]

a Water vapor activity [-]

V_{cell} Cell Voltage [V]

R Gas Constant [J/mol]

EW Equivalent Weight of Nafion [g/eq]

P_{sat} Water saturation pressure [Pa]

k_{abs} Absolute permeability of porous media [m^2]

k_{rl} Relative permeability for a phase [m^2]

s Saturation [-]

s_{irr} Irreducible saturation [-]

V_l Pore volume occupied by liquid water [m^3]

V_{pore} Pore Volume [m^3]

τ Tortuosity [-]

r Mean radius of pore size [m]

$\varnothing$ Porosity [-]

γ Surface tension [N/m]

θ Contact Angle [°]

P_C Capillary pressure [Pa]

P_{nw} Pressure of non-wetting phase [Pa]

P_w Pressure of wetting phase [Pa]

a_{lv} Liquid water-vapor interfacial surface area per unit volume $\left[\mathrm{cm^2 cm^{-3}}\right]$

$K_{e/c}$ Evaporation/Condensation rate constant [$\mathrm{Pa^{-1}\ s^{-1}}$]

ΔH_{lv} Heat of condensation/evaporation [KJ/mol]

Chapter 1 General Introduction

1.1 Background

Fuel cells present an attractive greener alternative to fossil fuels with low emissions and high efficiency, by converting the chemical energy of hydrogen rich compounds to electrical energy. Different types of fuel cells have been developed for diverse applications: Polymer Electrolyte Fuel Cell (PEFC) for transportation, alkaline fuel cells for space power and water generation, direct methanol fuel cells for portable power generation and solid oxide fuel cell, molten carbonate fuel cell and phosphoric acid fuel cell for stationary power generation. The PEFC is the fuel cell of interest in this study, since it the most commonly used for automobile applications.

A single cell of the PEFC, as shown in Figure 1, consists of an electron conducting anode, a polymer electrolyte, which is usually the Nafion membrane, and an electron conducting cathode. On each side of the anode and cathode, there are the Catalyst Layers (CL), Microporous Layers (MPL), Porous Transport Layers (PTL) and bipolar flow field plates. The porous transport layer (PTL) is synonymous to the gas diffusion layer (GDL), a term used in other works. For this study, the microporous layer (MPL) is considered to be a separate layer from the PTL. The PTL allow the transport of reactants to the CL and remove of the gaseous products and liquid water. In addition, the PTL serve as a conducting substrate to the CL and also provide mechanical support to the cell. The MPL, with a pore size in between that of the CL and the PTL, is a highly hydrophobic coating between the CL and the PTL used to improve water transport[1]. Hydrogen from the channels on the anode side and Oxygen/Air from the channels on the cathode side are transported by diffusion through the PTL and MPL to the catalyzed electrode layers where the electrochemical reaction take place. At the Anode Catalyst Layer (ACL), hydrogen is broken into

protons and electrons. The Nafion membrane enable the protons to travel from the anode to the cathode. The protons combine with the oxygen in the Cathode Catalyst Layer in an exothermic reaction to form water. Water and waste heat must be continuously eliminated, else they can cause significant concerns in the PEFC.

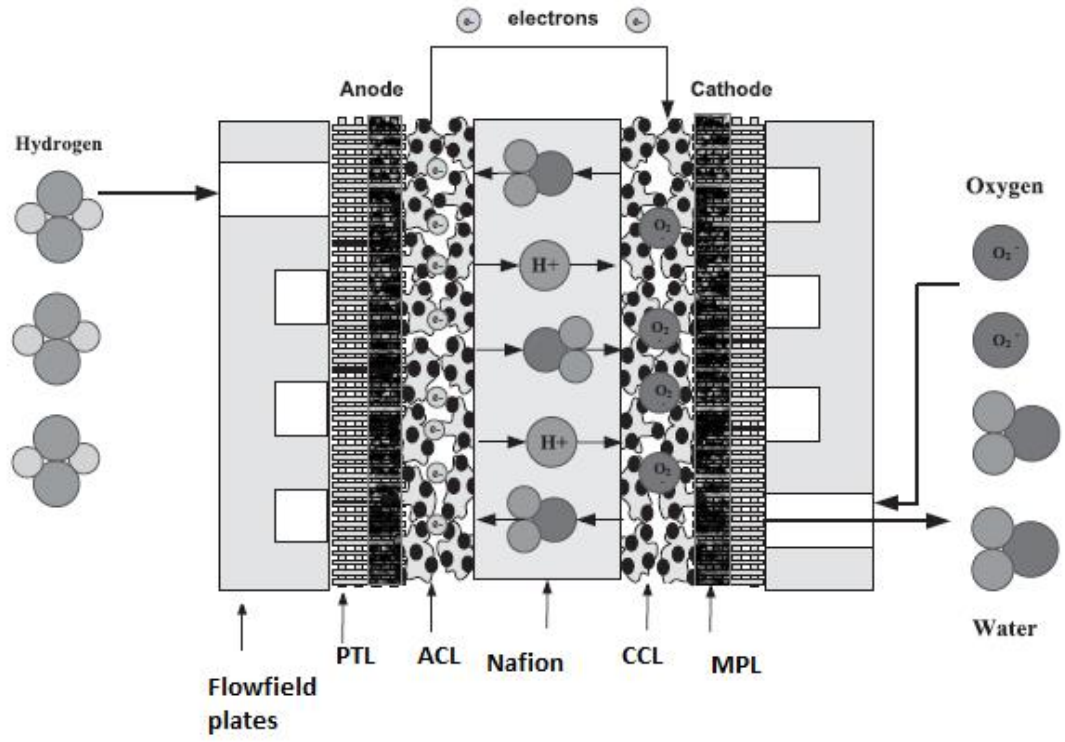

Figure 1: Schema of a PEFC[2]

Indeed, thermal management is one of the most critical issues that must be addressed to enable the mass commercialization of polymer electrolyte fuel cells. In fact, the amount of waste heat generated by a PEFC is the same as its electrical power output, resulting in an energy efficiency of only 50%. Thermal management is important at both the lower and upper limits of the operating temperature range, that is at sub-zero during cold start-up and winter climate conditions and at

elevated temperature[3]. When the PEFC is operated below 60°C, the electrochemical reaction kinetics is reduced and water condensation can results in cathode flooding. Although an elevated temperature is favorable for waste heat utilization, electrochemical reaction kinetics, efficiency, water management and tolerance against contaminants and carbon monoxide poisoning, it also has detrimental consequences on the PEFC [3], causing the following issues:

- **Electrolyte dehydration leading to reduced proton conductivity:** The operating temperature range depends on the properties on the electrolyte, in this case the polymer electrolyte membrane Nafion. At high temperatures, there is less water absorbed by the membrane resulting in reduced proton conductivity. As a consequence, there is a decrease in the performance and efficiency due to higher resistive losses.
- **Irreversible damage to Electrolyte (Nafion):** Bauer *et al.*[4], found that when Nafion is in contact with liquid water, there is a significant drop in the value of the E-modulus as temperature increases between 90°C and 95°C. When liquid water is easily accessible to a membrane with a reduced E- modulus, swelling will result in permanent degradation. Nafion modified with additive such as Zirconia can be more resistant to swelling at higher temperature.
- **Corrosion of carbon based catalyst support:** On the cathode side predominantly, the solid carbon atoms in the catalyst layer can react with oxygen atoms and/ or water to form either carbon monoxide or carbon dioxide which leaves the fuel cell as gaseous products[5]. This lead to a gradual corrosion of the cathode catalyst layer.
- **Lower performance at temperature above 80°C:** In the long term, the beneficial effects of an elevated temperature are superseded by the negative effects on the performance and

durability. The redistribution, sintering and agglomeration of the platinum catalyst particles lead to an overall degradation at high temperatures[3]. The maximum operating temperature of PEFC is often limited to 80°C due to the glass transition temperature of the Nafion membrane being between 80-120°C and also because more stress is placed on the membrane to maintain a relative humidity of 100%[6].

- **Non Uniform Temperature distribution:** The non-uniform temperature distribution exists not only in the through plane direction but also in-plane, along the flow channels. Barriers to a uniform temperature distribution are the asymmetry of the entropy change and overpotentials between the anode and the cathode, anisotropy of the different component layers, the coupled heat and water transport due to the rate of phase change being dependent on the local temperature (Evaporation/Condensation, heat pipe effect, saturation vapor pressure due to nanoscale dimension of pores) and regions of higher current density such as the inlet which degrades faster. At low current density, it was found experimentally that the temperature distribution within the PEFC was uniform while at higher current density, that is, low potential, there is a temperature variation of 2°C over the MEA region[7]. This interrelation between the current and temperature density was greater at the cathode inlet of serpentine flow plates. Alaefour[7], found experimentally a difference of 12 °C between the inside cell temperature and the surroundings or the endplates which could lead to hotspot formation if not cooled appropriately. Recently, Raileanu Ilie *et al.*[8], have embedded tantalum thermal sensors to obtain in-situ temperature measurements of the active catalyst layer. The presence of the overheats within the MEA has been demonstrated with a maximum of 10°C difference between the active catalyst layer and the bipolar plates[8].

Apart from performance and efficiency, an elevated operating temperature is linked to another significant design criteria, durability. Indeed, durability of fuel cell for automobile applications is a United States Department of Energy target which has not been reached yet. 6000 to 20000 hours is required for mobile vehicles while 40000 hours is the objective for stationary applications. According to a report published by U.S Drive, the system durability target as per the Figure 2 is the most challenging, with only close to 35 % achieved[9][10]. Even the objective for the system cost has been achieved up to 80 %[9][10].

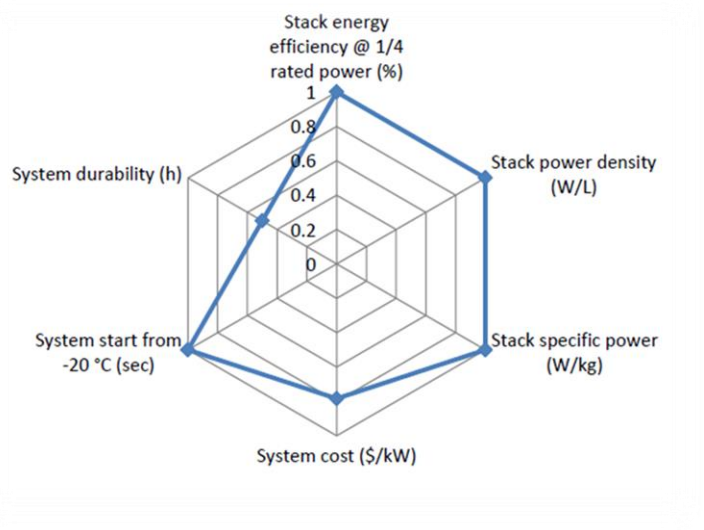

Figure 2: US Department of Energy targets[11]

Thermal transients situations such as the shut-down, start-up dynamics, heat accumulation and overshoot in temperature can lead to local hotspots due to changing local reaction rates according to Banerjee and Kandlikar[12]. These local hotspots can lead to the formation of pinholes in the membrane. Pinhole, in this work, refer to a breach throughout the membrane from the anode to the cathode side. Pinholes further increase the degradation rate and reduce the overall durability of the PEFC. Pinholes can also be the result of membrane corrosion, improper manufacturing of the

MEA, non-uniform stress distribution, intrinsic membrane material defects and contaminant particles. Pinholes through the membrane leads to gas crossover between the anode and the cathode. A highly exothermic reaction occurs due to the combustion of hydrogen, resulting in hotspots. Pinhole formation and hence gas crossover is further accentuated, causing accelerated degradation of the MEA and eventually catastrophic failure of the whole PEFC cell.

Effective thermal management in the catalyst layer, has the potential to improve platinum utilization and provide a more stable level of humidity throughout the stack since the electrochemical performance and water management of fuel cells is interwoven with the thermal management. It is indeed important to understand the sensitivity of the electrodes' properties on the temperature distribution in the cell to further the development of electrodes with optimal parameters to operate at higher temperatures, instead of the usual 65°C -70°C. In turn, this will enable the stack to sustain an elevated temperature through self-dissipation. As a result, this lowers the cooling system requirement which can occupy less volume and; hence, reduces gas consumption in vehicles, which are the prominent application of PEFC. The additional heat generated can also be used for a combined heat and power scheme for remote communities. Through an optimization using response surface methodology while considering both system efficiency and power output, Jeon *et al.*[13], showed that the optimal operating parameters were a high temperature of 90.6°C, a fully humidified feed with 100% R.H and 2.07 stoichiometric ratio between air and hydrogen.

1.2 Research Objectives

The present research work will focus on the study and modelling of the dissipation of heat generated due to the formation of local hot spots in the catalyst layer of the PEFC air electrodes. An emphasis has been placed on the catalyst layer since it is a region where most of the heat generation happens.

The role of the thermal conductivity of the catalyst layer, as an intrinsic parameter in the heat dissipation of hotspots such as “pinholes” which occur close to this layer, will be studied. The purpose is to determine whether the thermal conductivity is just as important as electrochemical properties of new catalyst layers. For example, new composite materials containing titanium additives can modify the thermal conductivity of the layer. The extent to which the ratio of the in-plane to the through-plane thermal conductivity (in other words, anisotropy) of the catalytic electrode layer influence the maximum temperature of the hotspot will be also be investigated.

In addition to demonstrating the importance of the thermal conductivity of the catalyst layers in the polymer electrolyte fuel cell, parametric studies will be performed on other variables such as, the thickness of the different constituent electrode layers, the effect of water percolation and the porosity of the porous transport layers. A comparison is performed to determine whether another parameter, other than the thermal conductivity provides a better pathway for heat dissipation. By observing how the thermal signature differs from one case study to the other, we can assess the significance of a specific property. Since the electrochemical performance and water management of fuel cells is interwoven with the thermal management, a two-phase model will also be developed

to investigate the thermal effect of varying water content in the porous transport layer, microporous layer and catalyst layer. Eventually, this study should enable the determination of whether the thermal properties are a significant parameter for heat dissipation in new fuel cells and fuel cells with pinholes. Sensitivity studies are only done on parameters which can be feasibly engineered. The range of the simulated values is also based on actual literature or commercial values.

1.3 Thesis Outline

The thesis is organized as follows: Chapter 2 provides an overview of the literature data for the properties of interest, the thermal conductivity as well as interfacial regions which provide additional thermal resistance. Previous non-isothermal modelling works and their limitations are also compared and discussed in that section. Chapter 3 contains the description of the physics for the primary single-phase model, geometric dimensions of the domain, heat sources and sinks, boundary conditions, assumptions and model parameters for the base case scenario. The two-phase model with liquid water percolation based on Darcy's Law is presented in Chapter 4. In that chapter, the effect of various properties on the thermal distribution and the parameter of interest, the maximum temperature in the domain, are explored. The parametric studies are done on the thermal conductivity of the catalyst layer and microporous layer, the anisotropy factor of the thermal conductivity of the catalyst layer, the thickness of the MEA layers, porosity of the PTL, varying water content in the porous layers on the cathode side. These are studied under both stagnant condition and with superficial liquid velocity through the porous layers.

Finally, the major conclusions drawn from the parametric studies are summarized in Chapter 5. The future steps to improve this study are also recommended. Following the conclusions of this research thesis work, the contributions should provide additional insights in devising the most appropriate strategies to dissipate the heat generated due to the formation of local hotspots such as pinholes in the membrane so as to reduce the degradation rate and; therefore, improve the overall durability of PEFCs.

Chapter 2 Literature Review

Following the review of the current status of thermal management issues in PEFC stack, Kandlikar *et al.*[14], came to the conclusion that the electrochemical performance of fuel cell cannot be dissociated from the heat transfer mechanism and that one of the critical areas of research in thermal management is obtaining accurate experimental data for the thermal conductivity of the components as well as studying the multidimensional effects of the anisotropic thermal properties. Pharoah *et al.*[15], have demonstrated the importance of considering anisotropic models compared to isotropic. Even though both result in identical polarization curves in experimental validation, the current density distribution is completely different.

2.1 Thermal conductivity

Consistent thermal conductivity values are required for non-isothermal single phase and two phase modelling since the thermal conductivity has an important effect on the overall temperature distribution. The thermal conductivity of the catalyst layer is the parameter of interest in this study for heat dissipation.

Catalyst layers, having a thickness between 10 and 20 um and being made by thin-film methods, can be considered as thin-film. Thin films can have radically different properties compared to their bulk materials[16]. Thermal conductivities of thin films can be several orders of magnitude lower than the bulk material due to the following reasons[17]: increased impurities, disorder, and grain boundaries due to the synthesis methods and decreased thermal conductivity as a result of photon leakage, boundary scattering and related interactions. When the catalyst film layer thickness approach the same length scale as the mean free path or wavelength of the heat carriers, that is the photons and electrons, it has a significant impact on the thermal conductivity of the film as there is a modification in the fundamental properties of the heat carriers, such as the velocity and density states[16].These effects can even happen for an atomically perfect thin film[17]. These defects contribute to a difference in the in-plane and through-plane transport leading to an anisotropic thermal conductivity even though the bulk material is isotropic. In-plane refers to the property measured in the direction parallel to the film plane while cross-plane/through-plane is perpendicular to the film plane, as illustrated in Figure 3.

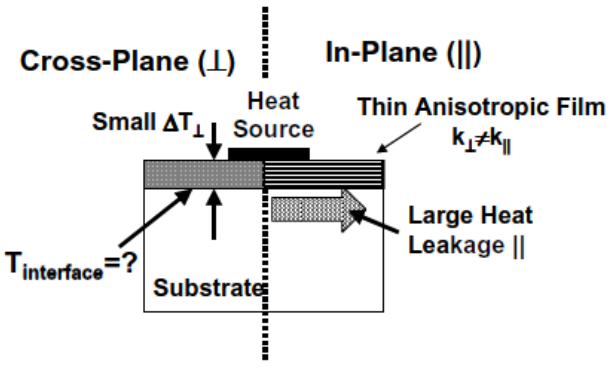

Figure 3: In-plane and through-plane/cross-plane direction for thin film[16]

Measurement of the thermal conductivities of thin films is challenging and conventional methods used for the bulk materials are not applicable. For the through-plane direction, the difficulty lies in creating a reasonable temperature drop across the film without creating a large temperature rise in the substrate[16]. While for the in-plane, there is potentially heat leakage through the substrate which makes the measurement of the actual heat flow in the plane of the film particularly challenging. Currently, the thermal conductivity measurement of thin film falls in two categories which can be distinct or combined [16]:Electrical heating and sensing and Optical method. The 3ω method, optical pump-probe, optical calorimetry are the most commonly used[16].

Several authors have reported values for the through-plane thermal conductivity of the catalyst layers as listed in Table 1, though the most frequent techniques for determination of the thermal conductivity of thin-film have not been used. Apart from one literature source in Table 2, there is a lack of experimental data available for the in-plane value of the catalyst layer. In-plane and through-plane values have also been reviewed for the Nafion membrane and the anisotropic gas diffusion layers that is, the porous transport layer and the microporous layer. Unlike the catalyst layers, these have been well-researched and consistent values are available as listed in Table 1 and Table 2. In comparison, thermal conductivity values for the catalyst layers range from a through plane value of 0.04 W/m K[18] to an in-plane of 0.39 W/ m K[19]. Due to the physical characteristics and fabrication method of the catalyst layers, the anisotropic nature of the thermal conductivity will be considered.

2.1.1 Through-Plane

Table 1: Literature review of measured thermal conductivity values (W/ m K)

	Khandelwhal and Mench[20]	**Vie and Kjelstrup**[21]	**Burford and Mench** [22]	**Ramousse *et al.***[23]	**Burheim *et al.***	**Karimi *et al.***	**Zamel *et al.***[24]	**Andisheh-Tadbir *et al.***[25]
Method	Ex-situ Steady State Through plane	In-situ temperature gradient	In-situ Micro-thermocouples	Thermostated bath Steady state Unidirectional flux	Ex-situ Through plane Rig Constant flux	Guarded heat flux meter	Thermal capacitance method(Slug)	Transient Plane source
Membrane Nafion®		-	0.025–0.25					
Dry	0.16±0.03	-			0.177±0.008[26]			
Fully humidified	0.29±0.03	-			0.254±0.016[26]			
Gas diffusion layer (Porous Transport layer)	1.80±0.27 (Toray Carbon Paper 26˚C, 2MPa)		0.13–0.19	0.36-1.36 (Quintech(190μm) 20˚C)	0.27[26] (Dry PTL 4.6 bar)	0.26-0.70 (0.7-13.6 bar)70 ˚C	0.1-0.5(Low deformation, PTFE 0%, 60%)	
	1.24±0.19 (Toray Carbon Paper 73 ˚C, 2MPa)	-	-	0.20-0.30 (Quintech(230μm)) with PTFE	0.36[26] (Dry PTL 9.3 bar)		0.8-1.8(High deformation, PTFE 0%, 60%)	
	0.48±0.09 (SIGRACET®(0%PTFE))	-	-	0.33-0.59 (Quintech(280μm))	0.40[26] (Dry PTL 13.9 bar)			
	0.31±0.06 (SIGRACET®(5%PTFE)	-	-	0.26-0.34 (SGLcarbon(420μm)) With PTFE				
	0.22±0.04 (SIGRACET®(20%PTFE)	-	-					
	0.22±0.04 (ETEK ELAT at 33 ˚C)							
Microporous layer	-	-	-	-	0.60(estimate)[26] (0.05-0.12) from 4-16 bar [27]	0.3-0.5(0-15 bar)Solvicore PTL with 30% PTFE and MPL		0.13-0.17 (1-6 bar) Effective value
Catalyst layer	0.27±0.05 (0.5mgcm^{-2} platinum)	0.2±0.1 (Catalyst layer and PTL)	-	-	0.50(estimate)[28] 0.04-0.08(4.6bar) 0.07-0.11(16.1bar) [18]			

General trends for PTL

An increasing concentration of PTFE in the PTL reduces the thermal conductivity [20] [26]. For temperature below 35°C, a decrease in the through-plane thermal conductivity is observed for an increased PTFE loading due to the overall increase in thermal resistance and reduced fibre to fibre contact[24]. However, above 35°C, the thermal conductivity value becomes independent of the PTFE content. Zamel *et al.*[24], attribute this finding to a change in the PTFE structure at higher temperature coupled with the high deformation which could result in a contact area between the contact fibers. The through-plane thermal conductivity increases with an increase in compression pressure due to the overall reduced contact resistance between the carbon fibers[20] [24] [26] [29]. However, the compression effect on the thermal conductivity is not that significant according to the work of Sadeghi and al.[30][31], Nitta *et al.*[32] and Radhakrishna *et al.*[33]. Burheim *et al.*[26], demonstrated that liquid water also led to increase of the through-plane thermal conductivity. They also observed that different thermal conductivity was obtained for different thickness of the sample due to the probable manufacturing process of stacking thinner layers to produce thicker ones. The temperature of the PTL itself influence the value of the thermal conductivity. Zamel *et al.* [24] found by using a thermal capacitance method that the effective thermal conductivity of the PTL(PTL) in the through-plane direction for a temperature range of -50 to +120 °C is given by the following empirical relationship, in which T is in degrees Celsius :

$$k_{through}\left(\frac{\mathrm{W}}{\mathrm{m\,K}}\right) = M\left(-7.166\times10^{-6}T^{3} + 2.24\times10^{-3}T^{2} - 0.237T + 20.1\right) \qquad (1.1)$$

By fitting the data from the study of Zamel *et al.*[24], Bhaiya *et al.*[34], obtained the below expression for M, the heat barrier resistance coefficient, where the temperature T is in degrees Celsius :

$$M = -1.495\times10^{-11}T^{5} + 2.601\times10^{-9}T^{4} - 6.116\times10^{-8}T^{3} - 9.829\times10^{-6}T^{2} + 8.754\times10^{-4}T + 0.0664 \qquad (1.2)$$

General trends for MPL

Burheim *et al.*[27], reported for the first time separate measurement of the thermal conductivity of the MPL itself while previous studies were for the MPL combined with the PTL. It was demonstrated in that study that the parameter which affects the thermal conductivity is the compaction pressure and not the PTFE content. The thermal conductivity increases irreversibly as the compression pressure increases. Despite improving conductivity, a higher compaction pressure can also have an adverse effect on the reactant/gas transport[27].

Thermal conductivity of the MPL, being quite low, can have an important impact on the overall temperature distribution. Through a 1D thermal model, Burheim *et al.*[27], showed that the integration of the MPL into the PTL and a wet or dry condition affect the temperature increase contribution of the MPL. The temperature rise is highest for a thick partly integrated MPL in wet condition.

General trends for Catalyst layers

Burheim *et al.*[18], reported for the first time separate measurement of the thermal conductivity of the catalyst layers. In this study, they found that for the dry catalyst layers, the only parameter which has an effect on the thermal conductivity is the compaction pressure. For real life applications, only values at a compaction pressure above 10 bars should be considered since the PTL, being very porous and compressible compared to the CL, will take up most of the compression while the CL thickness stays the same. Burheim *et al.*[18], also claim that the catalyst layer composition (Carbon: Nafion, Pt/C) has no impact on the thermal conductivity. In the case of catalyst layers with a water content, Burheim *et al.*[18], demonstrate qualitatively that neither the compaction pressure nor the catalyst content affect the thermal conductivity values. However, for the Catalyst Layer (CL) with higher ionomer content, the thermal

conductivity values seem to be much larger. For the CL saturated to its maximum value, the thermal conductivity value can be expected to increase by 50% when the ratio of Nafion to CL nanoparticles is 1:1 [18]. Burheim *et al.*[18], established that the thermal and mechanical properties of the MPL and CL are very similar. Kawase *et al.* [35] obtained a through-plane value of 0.073 W/m K at a temperature of 50°C and 50% RH by steady-state heat flux method. They found that the moisture content of the ionomer, due to a change in % RH, has little impact on the thermal conductivity and hence, the thermal conductivity is mostly due to the carbon black particles.

Thermal conductivity of Nafion

The thermal conductivity for Nafion is a function of the water content λ. At a temperature of 295±2K, this relationship is given by Burheim *et al.*[26]:

$$k_{Nafion}\left(\frac{\mathrm{W}}{\mathrm{m\,K}}\right)=\left(0.177\pm0.008\right)+\left(3.7\pm0.6\right)10^{-3}\lambda \tag{1.3}$$

The water content λ is defined as the ratio of the number of water molecules to the number of charged sites in the Nafion, and hence it has no unit [5]. The membrane has a water content of around 0.5 when in dry condition, 12 to 14 when exposed to water saturated gas (100% RH) but is contradictorily around 22 when exposed to liquid water(commonly referred to a case of Schrodinger paradox in the literature since it should have the same value in both saturated gas and liquid water condition) [34,35]. The observation can be explained due to the presence of liquid water which makes the surface more hydrophilic. It has been hypothesized that liquid water with no interfacial resistance overtakes the water sorption/desorption when the water content exceeds 14 in the presence of liquid water[36]. However, interfacial resistance is present during water exchange between the Nafion membrane and the unsaturated vapor[36].

2.1.2 In-plane

For Nafion, the in-plane thermal conductivity is not significantly different from the through-plane according to Alzhami *et al.*[19]. As the temperature increases, there is a slight decrease in the thermal conductivity values as shown in the Table 2.

Table 2: Literature review of measured thermal conductivity (W/ m K) values for In-plane direction

	PTL	MPL	Nafion	Catalyst layers
Sadeghi *et al.*[37]	17.5			
Teerstra *et al.*[22]	3.54-15.1 (SpectraCarb, Toray and Solvicore)	3.20, 3.87 (Solvicore with 30 % PTFE + MPL)		
Zamel *et al.*[38]	10.1- 14.7 (PTFE 0% -50%)			
Alzhami *et al.*[19]	12.75-17.75 (0-30%PTFE, 35°C) 15-17.75 (65 ˚C-3°C, 30% PTFE)		0.188 – 0.135 (35°C-65°C)	0.32-0.39 (0.41-0.51 mg cm^{-2} Pt, 35°C)

In-plane thermal conductivity of PTL

An effective in-plane thermal conductivity of the gas diffusion layers , k≈17.5 Wm^{-1} K^{-1}, has been determined by Sadeghi *et al.*[37] , and this remains constant over a wide range of PTFE content, and its value is about 12 times higher than that for through-plane conductivity. In previous modelling work, Burheim *et al.*[26] estimated an in-plane thermal conductivity to be 10x through plane while Ramousse *et al.*[23], estimated the parallel-plane thermal conductivity to be from 1.5 up to 3.5 times larger than the through-plane thermal conductivity. For different types of carbon paper (SpectraCarb, Toray and Solvicore) with varying PFTE content, Teerstra *et al.*[39], reported an in-plane thermal conductivity between 3.54 and 15.1 W/m K. The maximum of 15.1 W/m K was obtained for Toray paper with 30% PTFE. For the solvicore paper with 30 % PTFE and an MPL layer, values of 3.20 and 3.87 W/m K were

obtained. Alzhami *et al.*[19],also found that the thermal conductivity of the PTL decreases as the temperature increases from 35°C to 65°C due to the presence of PTFE/ polymeric resin whose thermal conductivity drops as the temperature rises. Addition of PTFE causes an increase in the thermal conductivity due to reduced thermal resistance between the fibres leading to transfer of heat along the fibres and replacing air with PTFE. Samples with MPL also had a higher value due to the higher concentration of carbon which is highly conductive.

Zamel *et al.*[38], obtained in-plane thermal conductivity values for the PTL between 10.1 and 14.7 W/m K for a PTFE content varying between 0% and 50% and fitted the following empirical correlation between the in-plane thermal conductivity of the PTL and the temperature T in degrees Celsius:

$$k_{through}\left(\frac{\mathrm{W}}{\mathrm{m\,K}}\right) = -7.166\times10^{-6}T^3 + 2.24\times10^{-3}T^2 - 0.237T + 20.1 \qquad (1.4)$$

Both an increase in the PTFE content and the temperature lead to a decrease in the thermal conductivity[38]. However, for a PTFE content of 5%, an increase in temperature does not result in significant decrease of the thermal conductivity compared to the concentration of 0%, 20% and 50%[38].

In-plane thermal conductivity of catalyst layers

With regards to the catalyst layer, it is not clear whether the thermal conductivity exhibits anisotropy based on the experimental data,. For instance, the in-plane value by Alzhami *et al.* [19] seems to be quite close to through-plane value by Khandelwal and Mench[20]. The in-plane thermal conductivity of the catalyst layer is not dependent on temperature and increased with platinum loading according to a study by Alzhami *et al.*[19]. However, this value is not determined directly but estimated from the thermal

conductivity of the MEA in which the thermal contact resistance between the membrane and the catalyst layer has been ignored, similarly to the value reported by Khandelwal and Mench[20].

2.1.3 Summary of trends in thermal conductivity of the layers of the PEFC

Table 3: Trends in thermal conductivity of through-plane layers of the PEFC

Through-Plane k	PTFE ↑	Compaction Pressure ↑	Water content ↑
PTL	↓	↑	↑
MPL	-	↑	Unknown
Catalyst	-	↑(dry)	↑
Membrane	-	Unknown	↑

Table 4: Trends in thermal conductivity of in-plane layers of the PEFC

In-Plane k	PTFE ↑	Temperature ↑	Pt% ↑
PTL	↓[38] ↑[19]	↓	-
MPL	Unknown	Unknown	-
Catalyst	-	-	↑
Membrane	-	↓ (slight)	-

Except for the contradicting effect of the PTFE content on the in-plane PTL thermal conductivity, there are some clear trends in Table 3 and Table 4 regarding the factors which influence the thermal conductivity of the different layers. The effect of PTFE content and temperature on the in-plane thermal conductivity value of the MPL have not yet been studied while the influence of the water content on the through value has yet to be investigated. For the through plane value of the membrane, no literature sources contained the impact of the compaction pressure. Other factors which could affect the thermal conductivity of the CL but which have not been looked into yet are : the ionomer content(% Nafion), type of solvent with different dielectric constant(glycerol, normal butyl acetate, IPA, ethylene glycol, etc),type of synthesized Pt supported on carbon nanoparticles. For instance, the type of catalyst ink solution obtained, precipitation,

colloidal or solution, is dependent on the value of the dielectric constant of the solvent. On drying, this has an impact on the microstructure of the catalyst layer.

2.2 Contact resistance PTL-Backing

Table 5: Literature values of the contact resistance between the PTL and backing (rib)

Authors	Contact resistance value(m^2KW^{-1})	Compression pressure	Material and location
Khandelwhal and Mench [20]	2.0×10^{-4}	2MPa	Toray carbon paper with smooth aluminium bronze surface
Burheim *et al.* [26]	2.1×10^{-4}	4.6 bar	
	1.8×10^{-4}	9.3 bar	
	1.1×10^{-4}	13.9 bar	
Burheim *et al.* [28]	3.9×10^{-4}		Between the PTL and the current collector
Burheim *et al.* [27]	0.7×10^{-4}		Between the backing and the PTL. Used in model for a wetted interface(a region of 5 um with a thermal conductivity of 0.7 W K^{-1} m^{-1})
Karimi *et al.* [29]	2.4×10^{-4}	0.7 bar	Between SpectraCarb PTL and Smooth Iron surface
Karimi *et al.* [29]	0.7×10^{-4}	13.8 bar	Between SpectraCarb PTL and Smooth Iron surface

The value of the contact resistance between the PTL and backing is consistently on the order of 10^{-4} m^2KW^{-1} as per the studies in Table 5, involving different types of PTL and backing material. According to Burheim *et al.*[26], PTL-PTL contact thermal resistance is negligible. Thermal contact resistance and the end effects are found to increase with the PTFE content as a result of increased number of PTFE coated fibers[37]. The value of the contact resistance can also vary depending on the humidity, wet or dry conditions [40].

2.3 Interfacial region between MPL and PTL

Burheim *et al.* [41] found that the interfacial region between the MPL and PTL consists of a composite layer with a thermal conductivity much higher than either the PTL-only region or the MPL-only region, with the MPL having the lowest thermal conductivity among the three. As a result, temperature differences in this interface are negligible. The possible reason which can explain this observation is a possible alignment of fibers in the in-plane direction. An estimate of $0.7 \pm 0.4 \times 10^{-4}$ K m^2 W^{-1}[41] for the thermal resistivity of the MPL-PTL composite layer was proposed[41]. There is a large uncertainty in the estimation value.

2.4 Non-Isothermal Modeling

Non-isothermal mathematical models for the polymer electrolyte fuel cell with different levels of complexity have been developed during the past few years. The main variations in the modelling work are:

- Geometry (1D, 2D,3D)
- Level of coupling of physics (mass, momentum, species, charge, energy, sorbed water, etc)
- Validation with experimental works
- Transient versus steady-state
- Parameters under study(Current density, Temperature, Water Content, Cell Voltage, Efficiency, etc)
- Heat sources and heat sinks(irreversible, ohmic, phase change, heat of vaporization, reversible, sorption/desorption)

- Non-isothermal effects (anisotropic heat transport, thermal osmosis)
- Single-phase or two-Phase flow
- Type of boundary conditions considered
- Use of commercial or open-source modelling software
- Stack or single cell

One of the earliest 3D mathematical models was proposed by Maggio *et al.*[42], to study the influence of geometrical and operating parameters on the temperature and current distribution in PEFC. A uniform temperature distribution with a gradient of less than 4°C in individual bipolar plates was achieved through the selection of appropriate operating conditions[42]. A transient single-phase 2D thermal model for a stack consisting of 2 cells has been proposed by Shan *et al.*[43]. Subsequently, a dynamic model for a stack of 20 cells and accounting for two-phase effects was developed by Park *et al.*[44]. In that work, the cells on each end demonstrated a temperature gradient between 4-10°C while the temperature distribution in the middle of the stack was rather uniform. Most of the non-isothermal modelling works have considered the thermal conductivity for all the porous layers to be isotropic. Authors have also used a wide range of thermal conductivity values as shown in Table 6. A single combined value has often been used for the gas diffusion layers consisting of the PTL and MPL despite the fact that these two layers have distinct properties.

Table 6: Literature review of estimated thermal conductivity values (W/m K) used in non-isothermal models

Authors	Membrane	PTL	MPL	CL	Flow field plates
Ju *et al.* [45]	0.95	0.5, 1.0, 2.94	n/a	n/a	n/a
Vie and Kjelstrup [21]	0.1±0.1	n/a	n/a	n/a	n/a
Berning *et al.* [46]	0.67	n/a	n/a	n/a	n/a
Hwang *et al.* [47]	0.5	1.7	n/a	n/a	n/a
Rowe and Li [48]	0.34	1.5	n/a	1.6	n/a
Burheim *et al.* [27]	0.25	0.96	0.10	0.1	200(Al)

Bhaiya *et al.*[34], provide a thorough literature review of the heat sources/sinks effects included in previous non-isothermal models. For the first time, thermal osmosis has been considered in their work. Reversible, Irreversible and Ohmic heating have been considered in most of the works while the sorption/desorption effect has been mostly neglected. It was demonstrated that at a high current density, the irreversible heating inside the cathode catalyst layer, the ohmic heating and heat of sorption accounted for approximately 60%, 25% and 10% respectively of the heat generated inside the cell[34].Hence, the heat due to the absorption of water into the Nafion membrane(heat of sorption) has an important influence on the temperature distribution inside the catalyst layers and membrane. On the other hand, Ju *et al.*[45], demonstrated that the irreversible heat generation due to the chemical reaction resulting from losses due to overpotentials at each electrode and reversible entropic heat due to the departure of the cell voltage from the standard state in the cathode catalyst layer are the main contributors to heat generation in the PEFC, contributing to approximately 80 to 90% of the total waste heat released. In the single phase thermal model developed by Ju *et al.* [36], the effects of the PTL thermal conductivity, the feed gas relative humidity, and the operating cell voltage were investigated.

Bapat[49] developed a 2D thermal model to study the effect of the PTL thermal conductivity. However, water management was neglected in that work and the heat transport properties are no longer relevant

based on current literature values. The temperature distribution in a 2D model considering the state of water has been studied by Pharoah *et al.*[40], where the focus was on distinguishing parameters which are critical in determining the maximum temperature generated within a fuel cell. It was shown that ohmic heating due to I^2R heating caused by membrane resistance due to proton current, is the smallest heat source. Since the ohmic resistance is dependant on the proton conductivity in the membrane which in turn depends on the water content, the latter can be considered homogeneous. The heat source/ sink contribution is also in contradiction with Bhaiya *et al.*[34], with sorption/desorption having the largest effect. In most of the non-isothermal models, the heat of desorption of water from the membrane to the gas phase is considered comparable to the heat of vaporization[34][40][50]. Indeed, for a water content greater than 5, there is negligible interaction between the membrane and water which results in the heat of desorption being equal to the heat of vaporization[51].The water profile was not solved directly but instead two variables, the net drag of water at the anode and the water produced at the cathode, were used to vary the state of water. A thermal conductivity of 0.5 W/ m K, which is larger than typically used by others, was used for both the MPL/ CL. The anode overpotential, in the irreversible heating source term, was considered to be independent of the local current density distributions. The influence of the thermal conductivity of the catalyst layers and microporous transport layers on a 1D temperature profile of a PEFC has been studied by Burheim *et al.*[18][27]. It was shown that the maximum temperature reached in the cell was dependent on the thermal conductivity values of the MPL and CL. However, none of the previous works have considered the impact of hotspots due to gas crossover through the membrane on the thermal distribution in the cell and how some intrinsic parameters, namely the thermal conductivity and water content play a role in heat dissipation in the presence of such thermal stress conditions.

Chapter 3 Thermal Model Development

3.1 Base case scenario

3.1.1 Geometric dimensions of domain

The domain under which the study will be performed is illustrated in **Error! Reference source not found.** and Figure 5. It is a section of the membrane electrode assembly with half a channel and half a rib. The main layers composing a polymer electrolyte fuel cell and which are considered in this model are the: bipolar plates, gas channels, gas diffusion layers, catalyst layers and membrane. The grooves in the flow field plates form the channels and the ribs are the regions in between the channels. In the Figure 4, the section of the diagram on the left is not to scale and has been expanded to show the different layers with more clarity.

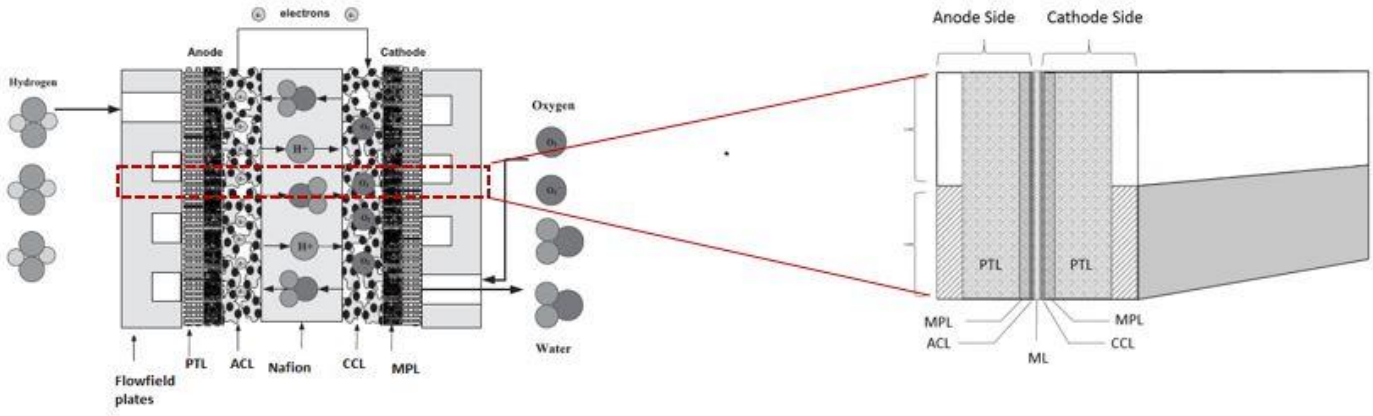

Figure 4: Domain under study: PEFC section with half a channel and half a rib

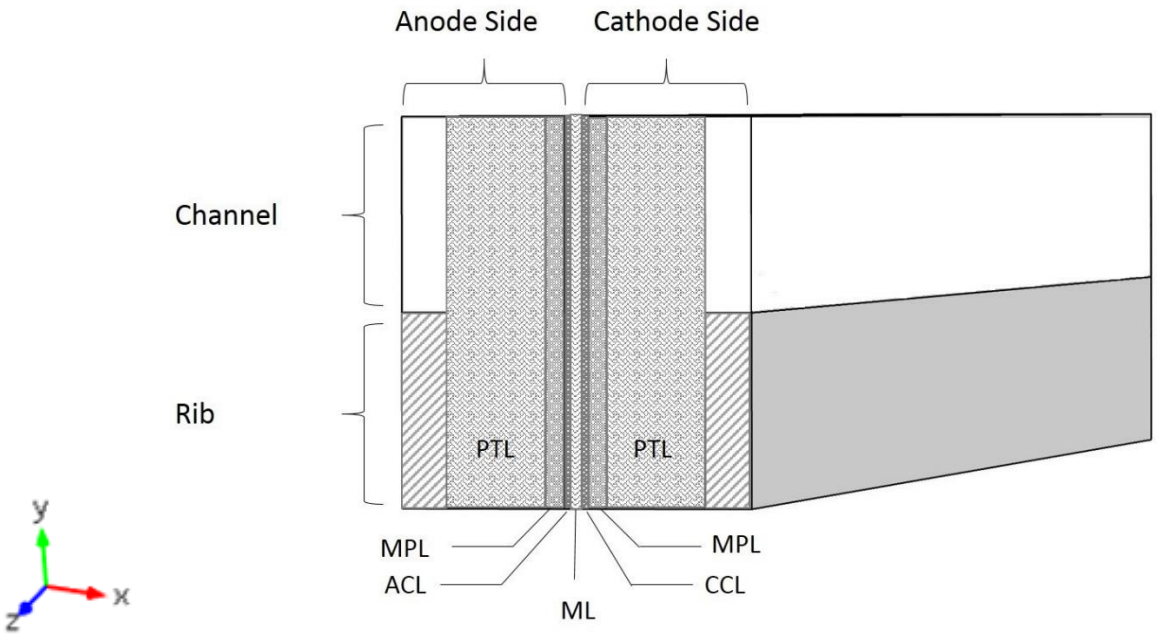

Figure 5:3D Model Domain

The thickness of each layer used in the base case scenario of the computational domain is given in the Table 7 :

Table 7: Dimensions of the PEFC layers

Layer	Thickness δ_i(m)
Rib	120 x 10^{-6}
Channel	120 x 10^{-6}
Porous transport layer(PTL)	255 x 10^{-6}
Microporous layer(MPL)	45 x 10^{-6}
Anode Catalyst layer(ACL)	10 x 10^{-6}
Membrane layer(ML)	30 x 10^{-6}
Cathode Catalyst layer(CCL)	20 x 10^{-6}

The length of the cell is 0.001 m and the depth of the cell is 0.01 m. The hotspot is modelled as a 20 µm wide cylindrical pinhole through the membrane and CCL and the five possible locations of the pinhole where the hotspots would be located are illustrated in the Figure 66. Based on the faster diffusion rate of hydrogen compared to oxygen, the heat generation due to the hotspot takes place in the CCL[52].

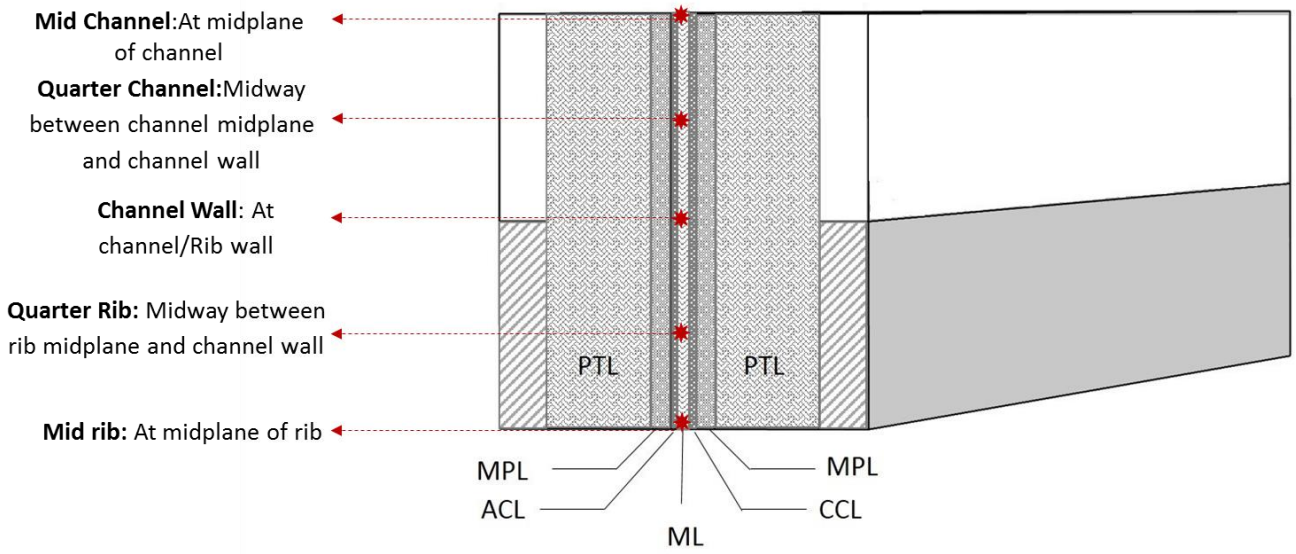

Figure 6: Location of hotspots under study

3.1.2 Model assumptions

The assumptions made in the base case scenario of the model are as follows:

- The model has reached steady state and; therefore, all the time derivatives are set to zero.
- The mass of the species leaving is equal to the mass of species entering the anode and cathode channels. The mass balance using the Stefan-Maxwell multicomponent equation (in appendix A.4)

and the energy balance were done using the modules in COMSOL by considering incompressible and laminar flow in the porous layers and the gas channels.

- Mass transport is only in the through plane direction where there is an overall mass balance through plane where the mass of species entering the region is equal to the mass of species leaving the region. There is no other path for mass to enter or leave the system for the simplified model since down the channel fluid velocity is negligible.
- Pressure gradients are negligible; hence, derivation of pressure in the conservation of energy equation can be dropped.
- Contact resistance is considered only between the PTL and MPL and between the PTL and rib since the contact resistances between the CL and Nafion and between the CL and MPL are considered to be negligible. Previous non-isothermal models have actually only considered a contact resistance between the PTL and rib only or no contact resistance at all[40][49][50][53].
- Due to the large electric conductivities of the PTL, MPL, CL and bipolar plates, the ohmic joule heating source has been neglected in those layers.
- Only heat transfer by conduction and convection is considered in the porous layers and in the channels while radiation heat transfer is negligible due to the low operating temperature of the PEFC. Indeed , Radiation only become significant for molten carbonate and solid oxide fuel cells[1].
- The heat generation resulting from viscous dissipation can be neglected since velocity gradients are not significant. The Brinkman number, which is the ratio between heat produced by viscous dissipation and heat transported by molecular conduction, is assumed to be small.

- Local equilibrium of the temperature for all the phases at a given point can be considered since the gas, liquid and solid phases within the porous layers are in close contact. Hence, products and reactants are assumed to be at the same temperature as the PEFC component layers that they flow through.
- Soret and Dufour effects (when concentration gradients produce a heat flux and the reverse for the Soret effect) are neglected since at the operating temperature range of the PEFC, thermal diffusion is negligible according to Weber *et al.*[54]

An initial assumption that was later modified as part of the parametric study:

- A single fluid phase consisting of humidified air and in which no heat sink or heat source due to phase change, such as condensation and evaporation is considered.

3.1.3 Model Parameters Values

The modelling work has been performed using COMSOL version 5.2. The base case scenario of the model considers the following common operating parameters for a PEFC: a current density j of 10000 A/m^2 (1 A/cm^2), a water content λ of 10.7, that is the ratio of the number of water molecules to the number of charged sites in the Nafion is 10.7, an initial temperature of 343.15 K in the whole domain and an average gas velocity of 0.25 m/s in the channel at the anode and cathode in the downstream direction only. The average gas velocity in the channels in the downstream direction is not varied throughout this study.
The through-plane thermal conductivity used for each layer is as follows:

Table 8: Through-plane thermal conductivity of the PEFC layers

Layer	k_i(W $k^{-1}m^{-1}$)	Source
Plate	200	[55]
Channel (air) on anode side	0.0299	[56]
Channel (H_2) on cathode side	0.182	[55]
Porous transport layer(PTL)	0.54	[26]
Microporous layer(MPL)	0.0084	[27]
Anode Catalyst layer(ACL)	0.1	[18]
Membrane layer(ML)	$0.177+ (3.7)\ 10^{-3}\lambda$	[4]
Cathode Catalyst layer(CCL)	0.1	[18]

Except for the MPL and the PTL, all the other layers are considered isotropic in the base case scenario. This means that the value of the in-plane thermal conductivity will be equivalent to the through-plane value. As mentioned previously in the literature review, it has been reported by a number of researchers that the gas diffusion layers are anisotropic[22] [37] [38]. Hence, for the PTL and MPL layers, the in-plane thermal conductivity has been set as 10 times the value of the through plane. A compaction pressure of 9.3 bar for a humidified PTL and an MPL consisting of 25% PTFE are considered for the initial simulation[26] [27]. Hence, the corresponding experimental PTL and MPL thermal conductivities for these conditions have been used for the modelling. The anisotropic effect of the catalyst layers is investigated in the parametric studies but in the initial base case simulation, they are considered to be isotropic with an assumed thermal conductivity of 0.1 W/m K.

A constant thermal conductivity value of 0.58 W/m K has been applied for the liquid water, which partially fills the porous layers of the CL, MPL and PTL in a typical PEFC [57] [58]. For the range of the simulated

operating temperature and pressure, the thermal conductivity change for water is not significant unless there is liquid to vapor phase change.

3.1.4 Solver configuration

In this work, COMSOL, is the modelling software used to solve the finite-element model. The preordering algorithm used for the current model is the PARDISO (parallel sparse direct solver) with nested dissection multithreaded developed by Olaf Schenk *et al.*[59]. This solver is usually used for solving large sparse symmetric and non-symmetrical linear systems of equations.

3.1.5 Meshing

A mesh refinement study was done to ensure that the solution is grid-independent. The parameter of interest is the maximum temperature in the domain which is the output parameter that is tracked as the mesh size is varied. The selected customized mesh specifications are shown in Table 9.

Table 9: Mesh Parameters

Name	Value
Maximum element size	200
Minimum element size	2
Curvature factor	0.2
Resolution of narrow regions	1
Maximum element growth rate	1.2

Figure 7 shows the variation in mesh density as the grid becomes more refined near the boundaries of the sub-domains.

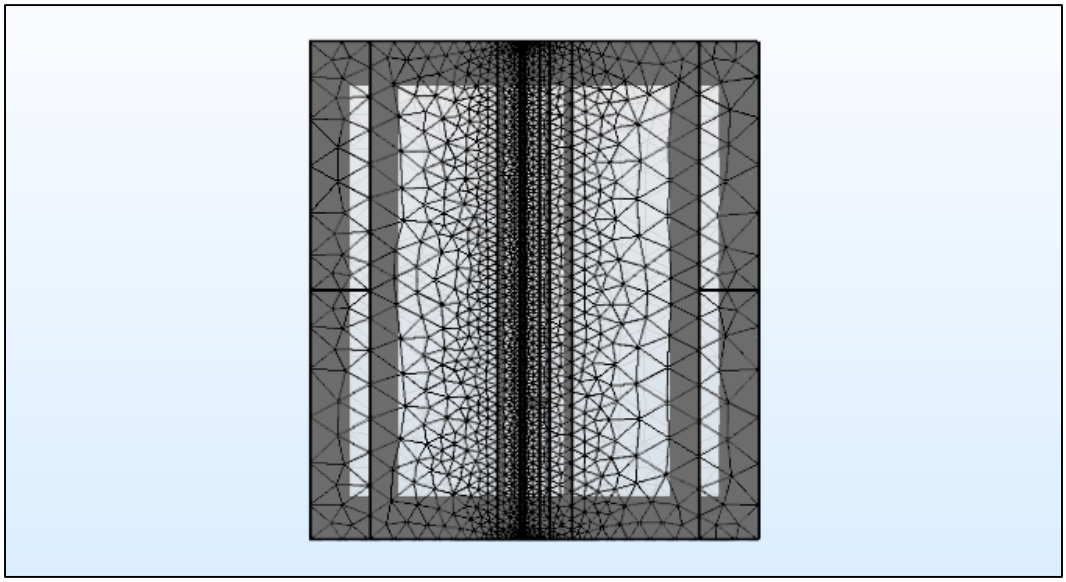

Figure 7: Meshing for the Quarter rib pinhole which is located midway between the rib wall and the midplane of rib

3.2 Thermal model development

The energy balance in this study is described in this section while the details of the mass balance can be found in Appendix A.4. The solution from the steady state mass transport equation was used as an input to the thermal model.

3.2.1 Heat transport theory in fuel cells

The thermal model can be described with the following conservation of energy equation:

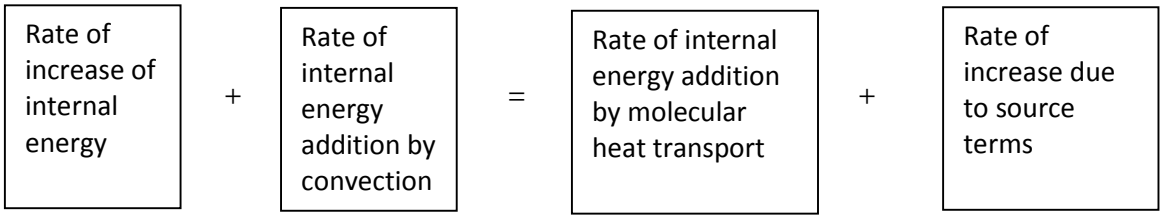

$$\frac{\partial}{\partial t}\left(\rho C_P T\right)+\nabla\left(\varepsilon\rho u C_p T\right)=\nabla\left(k_i\nabla T\right)+Q_i \tag{2.1}$$

According to the energy conservation equation, the total energy changes in a controlled volume equals the sum of the energy flux at the boundaries and the internal energy sources. The energy flux at the boundaries consists of the conductive heat transfer across the fuel cell and the convective heat transfer occurring between bipolar plates with the coolant and the reactants. In view of the assumptions of steady state and negligible velocity gradient (stagnant condition), the energy conservation equation reduces to the following:

$$\nabla\left(k_i\nabla T\right)+Q_i=0 \tag{2.2}$$

The balance of the heat generation (heat sources) and heat removal (heat sinks) determines the temperature distribution in the fuel cell. The same conservation of energy equation can be applied for all layers of the PEFC. The only variation is due to the different heat sources and sinks in each layer.

3.2.2 Heat sources and sinks

The heat produced in an electrochemical reaction consists of reversible Peltier heats and irreversible heat. The internal energy source is composed of the entropy loss and the chemical energy required for protons to overcome the barrier of the over-potentials in both catalyst layers.

3.2.2.1 Reversible Entropic heat source-Peltier heats

The maximum electrical work obtainable from the electrochemical reaction, is related to the Gibbs free energy change of the reaction ΔG.

By the principles of thermodynamics, the differential change in the Gibbs free energy, ΔG can be written as:

$$\Delta G = \Delta H - T\Delta S$$

$$\Delta G - \Delta H = -T\Delta S$$

The reversible heat generated due to entropy change, results from the difference between the maximum electrical work and the total available potential work. It is also referred to as Peltier heating.

For a reversible system, the overall heat released can be written as:

$$\Delta Q = -T\Delta S$$

The rate of consumption of the reactant, n_{H_2} is given by:

$$n_{H_2} = \frac{I}{nF} A$$

Hence, the reversible heat source expression can be derived as follows,

$$Reversible\,heat\,source = Q_{rev} = \left(-T\Delta S\right) n_{H_2} = \left(-T\Delta S\right) \frac{I}{nF} A \qquad (2.3)$$

Reversible heat source expression at the ACL:

$$Q_{rev,ACL} = \frac{T\Delta S_{ACL}}{\delta_{ACL}} \frac{j}{nF} \tag{2.4}$$

Reversible heat source expression at the CCL:

$$Q_{rev,CCL} = \frac{T\Delta S_{CCL}}{\delta_{CCL}} \frac{j}{nF} \tag{2.5}$$

The distribution of the entropy of reaction between the anode and cathode is ambiguous. As Ramousse *et al.* [60] points out in a literature review of the possible entropies at the ACL and CCL, charged species(H+ and e-) must be considered for the half reactions entropy. Hence, this is hard to separate since a solution of cations will always contain anions. Some values of the entropy for the anode reaction are estimated to be: +0.6 J/mol K, -0.104 J/ mol K[50],-226 J/mol K[60]. Estimates of the entropy of the cathode reaction include the following : -82 J/mol K [28], +163.16 J/mol K[50], +62.8 J/mol K[60].This situation is further complicated if the gas dilution is taken into account when assuming that water is produced in the liquid phase. The expression for the change in entropy depends on the activity of the hydrogen and oxygen[60]. In the present model, the following entropies of the electrode half-cell reactions have been used:

$$\Delta S_{ACL} = -0.104 \text{ J / mol K}$$

$$\Delta S_{CCL} = +163.16 \text{ J / mol K}$$

3.2.2.2 Irreversible heat source

The irreversible heat generation is due to cell operated at a voltage different V_{cell} from the thermodynamic potential V_o. Hence, it is the activation, ohmic and concentration polarizations or overpotentials η which give rise to the irreversible heat generation.

The overpotential η can be expressed as,

$$\eta = \left(V_o - V_{cell}\right)$$

Hence, the general expression for the general heat source can be written as,

$$Irreversible\ heat\ source = Q_{irrev} = \left(V_o - V_{cell}\right) I\ A \tag{2.6}$$

Irreversible heat source expression at the ACL, $Q_{irrev,ACL}$:

$$Q_{irrev,ACL} = \frac{\eta_{ACL}}{\delta_{ACL}}\, j \tag{2.7}$$

Irreversible Heat source expression at the CCL, $Q_{irrev,CCL}$:

$$Q_{irrev,CCL} = \frac{\eta_{CCL}}{\delta_{CCL}}\, j \tag{2.8}$$

Activation overpotentials for irreversible heat source

The activation polarisation loss/ overpotential can be described by the classical Butler-Voltmer equation, in which the electrochemical process is limited by the charge transfer of electrons[1]:

$$j_{cell} = j_o\left[\exp\left(\frac{\alpha_a F}{RT}\right)\eta - \exp\left(\frac{-\alpha_c F}{RT}\right)\eta\right] \tag{2.9}$$

It should be noted that the current density j_{cell} is in A cm^{-2} in the above equation. To decrease the computational cost, simplified explicit expressions of the Butler-Volmer equation for the overpotential at the anode and the cathode have been used here[1].

Facile kinetics at the Anode

The HOR at the anode is much more facile than the ORR at the cathode, hence less activation losses occurs there.

In this case we can linearize the Butler-Volmer equation by posing $x = \left(\frac{\alpha F}{RT}\right)\eta$ as per Mench *et al.*[1]. A power series expansion can be considered for exp (x), e^x:

$$e^x = 1 + x + \frac{x^2}{2!} + \frac{x^3}{3!} + \ldots \tag{2.10}$$

For small values of x, the higher order terms can be neglected,

$$j_{cell} = j_o\left[\left(\frac{\alpha_a F}{RT}\eta + 1\right) + \left(\frac{-\alpha_c F}{RT}\eta + 1\right)\right] \tag{2.11}$$

Hence, at the anode for a facile HOR kinetics, by rewriting the expression for the over potential as a function of the current density and considering $\alpha_a = \alpha_c = 0.5$, then ($\alpha_a + \alpha_b$) =1[1],

$$\eta_{ACL} = \pm\frac{j}{j_o}\frac{RT}{(\alpha_a + \alpha_c)nF} = \frac{j}{j_o}\frac{RT}{nF} \tag{2.12}$$

This applies for when the exchange current density is very high and the current is low, that is, the electrode polarization is very small[1].

Tafel Kinetics at the Cathode

For the slower kinetics at the cathode, the cathodic branch of the Butler-Volmer equation with a negative overpotential η will exponentially increase. On the other hand, the anodic branch will be a decreasing term. As a result, the latter can be neglected, and the Butler Volmer equation reduces to the Tafel Kinetics model[1]:

$$j_{cell} = j_o \left[\pm \exp\left(\frac{\pm \alpha_a F}{RT} \right) \eta \right] \tag{2.13}$$

The Tafel simplication is then rearranged to provide the cathodic overpotential:

$$\eta_{CCL} = \left(\frac{RT}{\alpha F} \right) \ln \frac{j}{j_o} \tag{2.14}$$

It should be noted that this Tafel approximation applies for operation of cell above 0.55 V according to Burheim *et al.* [28].

The values of the parameters used in the above equations for the base case model are:

R: Molar gas constant $= 8.314 \frac{\text{J}}{\text{mol K}}$

F: Faraday's constant =96485 C/mol

α: Transfer coefficient for both ACL and CCL =0.5

j_o: Exchange current density at both anode and cathode, $j_o = 5 \times 10^{-4}$ A cm^{-2}

The transfer coefficient α is 0.45 and 0.483 from a thermal signature and a classical approach respectively [61]. At a temperature of 323 K, Burheim *et al.* [61] use an exchange current density of

$j_o = 5.36\times10^{-4}$ A cm^{-2} (thermal) or $j_o = 4.24\times10^{-4}$ A cm^{-2} (Classical). In Mench[1], typical exchange current densities for an acid electrolyte at 300 K, 1 atm and with Pt as catalyst, are listed as j_o = 1 x 10^{-3} A cm^{-2} for the HOR and j_o = 1 x 10^{-9} A cm^{-2} for the ORR.

The exchange current density j_o refers to the equilibrium rate at which reactant and product species are exchanged. This is applicable for an absence of activation overpotential and a high value indicates a fast reaction while a low value indicates a slow reaction[5]. Indeed, the exchange current density depend on several factors, namely the temperature, the electrode active catalyst area and morphology, concentration and it varies for the HOR at the anode and the ORR at the cathode[1]. Because these discussed parameters are difficult to obtain experimentally or analytically, sensitivity studies could be done to determine their impact on the results in this study.

3.2.2.3 Ohmic losses heat source-Joule heating

Ohmic losses, in other words, joule heating caused by the transport of electrons and protons in the cell have been considered as a heat source in the Nafion membrane.

$$Q_{ohmic} = \frac{I^2}{\sigma} \tag{2.15}$$

The ionic/proton conductivity σ is given by Springer *et al.* [62]:

$$\sigma = (0.5139\lambda - 0.326)\exp\left[1298\left(\frac{1}{303} - \frac{1}{T}\right)\right] \tag{2.16}$$

The water content λ can be expressed as:

$$\lambda = 0.043 + 17.81a - 39.85a^2 + 36.0a^3 \quad for\ 0 < a \le 1 \tag{2.17}$$

$$\lambda = 14 + 1.4(a - 1) \ for\ 1 < a \le 3 \tag{2.18}$$

Where the water activity $a = \frac{C_W RT}{P_{sat}(T)} = \frac{y_v P}{P_{sat}(T)}$ and the equivalent water concentration in the membrane is given by $C_W = \frac{\rho_{dry,mem}\lambda}{EW}$

EW [g/eq] is the equivalent weight of Nafion membrane. It is given by the following expression, where *y* is the number of tetrafluoroethylene groups per polymer chain[1]:

$$EW = 100y + 446$$

Hence, the EW is proportional to the amount of inert backbone relative to the conducting side chains. For Nafion 111 used in this model, the EW is 1100[1].

The relative humidity is equivalent to the water activity when vapor and temperature equilibrium are attained[63].

The water saturation pressure, $P_{sat}(T)$, is dependent on the temperature and the relationship given by Motupally *et al.*[64] and Songprakorp[65]:

$$Log\left(P_{sat}(T)\right) = -2.1794 + 0.02953(T - 273.15) - 9.1827\times10^{-5}(T - 273.15)^2 + 1.4454\times10^{-7}(T - 273.15)^3 \tag{2.19}$$

In the membrane, the resulting expression for the ohmic heat source is:

$$Q_{ohmic,ML} = \frac{j^2}{(0.5139\lambda - 0.326\exp\left(1298\left(\frac{1}{303} - \frac{1}{T}\right)\right)} \tag{2.20}$$

3.2.2.4 Pinhole heat source

Stanic and Hoberecht [66], demonstrated in a scanning electron microscope micrograph that the pinhole is a 20 μm wide hole in the membrane surrounded by burnt catalyst. Based on a pinhole size and MEA ignition heat, they estimated that a hydrogen flow rate of 6.2 x 10^{-6} cm^3/s is required to create a pinhole considering an exothermic heat of reaction of 285 kJ/mol. For a hydrogen and air inlet flow rates set at $0.2ms^{-1}$ and $0.5ms^{-1}$, respectively, Lu *et al.*[52], found that the average hydrogen diffusion flux through a pinhole from the anode to cathode is 45 mol $m^{-2}s^{-1}$ while the oxygen diffusion flux is 0.56 mol $m^{-2}s^{-1}$. With these parameters, they obtained a temperature at the hotspot that was 4-5 K higher than under normal conditions. Due to the hydrogen diffusion flux through the pinhole being much greater than that of oxygen, the formation of the hotspot took place at the cathode side of the pinhole in their simulation[52].In the current model, the thermal conductivity of air inside the pinhole is considered the same as humidified air. The pinhole model has been based on the above mentioned work. As a result, for an oxygen diffusion flux of 0.56 mol $m^{-2}s^{-}1$, the heat source due to the hotspot formation has been calculated as: $Q_{Hotspot} = 160{,}160\,\mathrm{W/m^2}$.

3.2.2.5 Heat of Vaporisation (Heat Sink)

In a single-phase model, water is assumed to be formed in the vapor phase. As a result, the heat of vaporisation of liquid water is considered in the cathode catalyst layer for the Oxygen Reduction Reaction (ORR).

This heat sink term is given by:

$$Q_{Vap,CCL} = \frac{-j}{2F}\hat{h}_{fg,water} \tag{2.21}$$

The molar latent heat of vaporisation of water, $\hat{h}_{fg,water}$, can be determined from the following formula[67]:

$$\hat{h}_{fg,water} = 2500.304 - 2.252(T - 273.15) - -0.0215(T - 273.15)^{1.5} - 3.175x10^{-4}(T - 273.15)^{2.5} - 2.861x10^{-5}(T - 273.15)^{3} \tag{2.22}$$

For a two-phase model, the vaporisation of all the liquid water into the vapor phase should not be considered.

3.2.2.6 Heat of sorption/ desorption

Heat can be released (heat source) or absorbed (heat sink) due to respectively the sorption or desorption of water vapor in the catalyst layers. Bhaiya *et al.*[34], showed that the heat of sorption/desorption can contribute up to 10% of the total heat sources at normal operating conditions. For current densities below 1000 mA/cm^2, the sorption/desorption heat actually exceeds the protonic ohmic heat source in the membrane. The source term for sorption/ desorption in the catalyst layers is given by[53]:

$$Q_{Sorption} = \frac{k_t \rho_{dry}}{EW}\left(\lambda_{eq} - \lambda\right)\Delta H_{sorption} \tag{2.23}$$

Where,

k_t: Time constant[s^{-1}]

λ_{eq}: Equilibrium membrane water content[-]

EW: Equivalent weight of Nafion[g/eq]

ρ_{dry}: Density of dry Nafion[kg/m^3]

$\Delta H_{sorption}$: Molar enthalpy change due to the sorption/desorption of water vapor into the electrolyte [kJ/mol]

The time constant, k_t [s^{-1}], represents the time scale for a membrane to reach its equilibrium sorption state when placed in humid air. This time constant is significant for ensuring the coupling between the membrane and the catalyst and it represents the transfer of water from the vapor or liquid phase in the catalyst layer to the membrane[53][68]. This time constant is different depending on studies. 10 s^{-1}(liquid-membrane) or 10^{-5} s^{-1}(vapor-membrane) has been used in Songprakorp[65] while Bhaiya *et al.*[53] use a value of 10^4 s^{-1}. Its order of magnitude varies between 100s^{-1} to 1000s^{-1}[68]. In Secanell[68] and Bhaiya[53] works, this constant was set to 10000 s^{-1} for a guaranteed coupling between the membrane and catalyst.

The equilibrium membrane water content,λ_{eq}, is given by the following expression:

$$\lambda_{eq} = \left[1 + 0.2352a^2 \frac{(T - 303.15)}{30}\right]\left(14.22a^2 - 18.92a^2 + 13.41a\right) \quad (2.24)$$

A maximum value of $\lambda = 14$ is considered for a fully humidified condition [1]. The density of Nafion, ρ_{dry}, is taken as 1580 kg/m^3[69]. In this work, the thickness of the membrane layer is 30μm. This corresponds to a thickness of around 0.001inch, for Nafion 111, in which, the last digit represent the thickness. The equivalent weight of the ionomer material, EW, which is the dry membrane weight per sulphonate group, is thus equal to 1100 g/mol [70]. Ramousse *et al.*[60], demonstrated that the value of

the molar enthalpy change due to the sorption/desorption of water vapor into the electrolyte, $\Delta H_{sorption}$, is similar to the enthalpy of vaporisation of water. At a temperature of 80°C, a constant value of 45 kJ/mol has been considered. In Pharoah *et al.*[40], when water vapor absorbs into the Nafion membrane, a heat source is applied as 44.7 kJ/mol, and when water desorbs to the vapor phase, a heat sink is applied as−44.7 kJ/mol.

3.2.2.7 Summary of heat sources/sinks

The heat source in the membrane consists only of the ohmic losses in this work. In the PTL, MPL and the gas channels, no heat sources are considered. In the bipolar plates, there is a heat sink due to convection by the coolant gases.

Table 10: Summary of heat sources/sinks

Layer	Q, Volumetric heat source/sink (W m^{-3})
Porous transport layer(PTL)	-
Microporous transport layer(MPL)	-
Anode Catalyst layer(ACL) $Q_{rev,ACL}$ (See Section 2.4) $Q_{irrev,ACL}$ (See Section 2.7) $Q_{Sorption}$ (See Section 2.23)	$Q_{rev,ACL} + Q_{irrev,ACL} + Q_{Sorption} =$ $\frac{T\Delta S_{ACL}}{\delta_{ACL}}\frac{j}{nF} + \frac{\eta_{ACL}}{\delta_{ACL}} j + \frac{k_t \rho_{dry}}{EW}\left(\lambda_{eq} - \lambda\right)\Delta H_{sorption} =$

	$\frac{T\Delta S_{ACL}}{\delta_{ACL}}\frac{j}{nF} + \frac{\frac{j}{j_o}\frac{RT}{nF}}{\delta_{ACL}} j + \frac{k_t \rho_{dry}}{EW}\left(\lambda_{eq} - \lambda\right)\Delta H_{sorption}$
Membrane $Q_{ohmic,ML}$ (See Section 2.20)	$Q_{ohmic,ML} = \frac{j^2}{(0.5139\lambda - 0.326\exp\left(1298\left(\frac{1}{303} - \frac{1}{T}\right)\right)}$
Cathode Catalyst layer(CCL) $Q_{rev,CCL}$ (See Section 2.5) $Q_{irrev,CCL}$ (See Section 2.8) $Q_{Vap,CCL}$ (See Section 2.21) $Q_{Sorption}$ (See Section 2.23)	$Q_{rev,CCL} + Q_{irrev,CCL} + Q_{Vap,CCL} + Q_{Sorption} =$ $\frac{T\Delta S_{CCL}}{\delta_{CCL}}\frac{j}{nF} + \frac{\left(\frac{RT}{\alpha F}\right) ln\frac{j}{j_o}}{\delta_{CCL}} j + \frac{-j}{2F}\hat{h}_{fg,water} +$ $\frac{k_t \rho_{dry}}{EW}\left(\lambda_{eq} - \lambda\right)\Delta H_{sorption}$

3.2.3 Convection heat flux in the channels

In the bipolar plates, there is a heat sink due to convection by the gases. For laminar flow in channels with a square cross-section or a rectangle with an aspect ratio of 1.0, the Nusselt number ($Nu=hL/k$) is 2.98[55][49]. The temperature of the gas in the channel is 70°C, that is, the gas enters the domain at 70°C and leaves the domain at 70°C.

In COMSOL, the Heat transfer in fluids physics has been applied to the hydrogen and air gas channels. The following Convective heat flux boundary condition is applied on the wall of the channels:

$$-n\Delta\left(-k_i\nabla T\right)=h\left(T_{ext}-T\right) \tag{2.25}$$

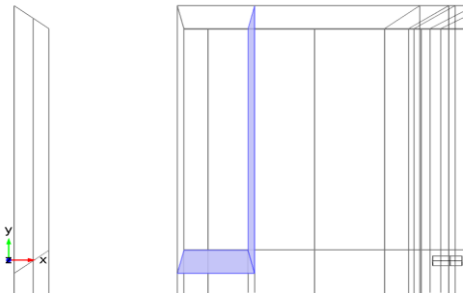

Figure 8: Convection boundaries on the anode side

The convection takes place on the boundaries shaded in blue in the Figure 8.

The temperature of fluid (T_{ext}) =70°C.

The convective heat transfer coefficient, h, is given by:

$$h=\frac{\text{Thermal conductivity of fluid* Nusselt number}}{\text{length of channel}} \tag{2.26}$$

3.2.4 Boundary conditions

A Dirichlet constant temperature of 70°C is applied to the right and left side of the domain (both on channel and plates). The top and bottom sides are symmetric boundaries (zero flux). This is comparable to a perfect thermal insulation condition meaning that there is no heat flux across the boundary.

$$-n\Delta\left(-k_i\nabla T\right)=0 \tag{2.27}$$

A Thermal contact resistance condition is applied at the interface between the PTL and the bipolar plate. This thermal contact resistance, $R_S = \frac{d_s}{k_s}$ is considered as 0.9 x 10^{-4} K m^2/W based on the previously reviewed literature values [27] [29].

In COMSOL, the heat flux across this Thin Thermally Resistive Layer is defined by[71]:

$$-n_d \bullet \left(-k_d \nabla T_d\right) = -R_S \left(T_u - T_d\right) \tag{2.28}$$

$$-n_u \bullet \left(-k_u \nabla T_u\right) = -R_S \left(T_d - T_u\right) \tag{2.29}$$

Where the *u* and *d* subscripts refer to the upside and downside of the layer, respectively.

3.3 Thermal and heat sources distribution

The temperature distribution, in the **Error! Reference source not found.** 9 below, represents the temperature data from the anode to the cathode side along the width of the different layers of the PEFC which is obtained from a cut line which goes through the centre of the hotspot/pinhole and the middle of the depth (z-axis) of the domain.

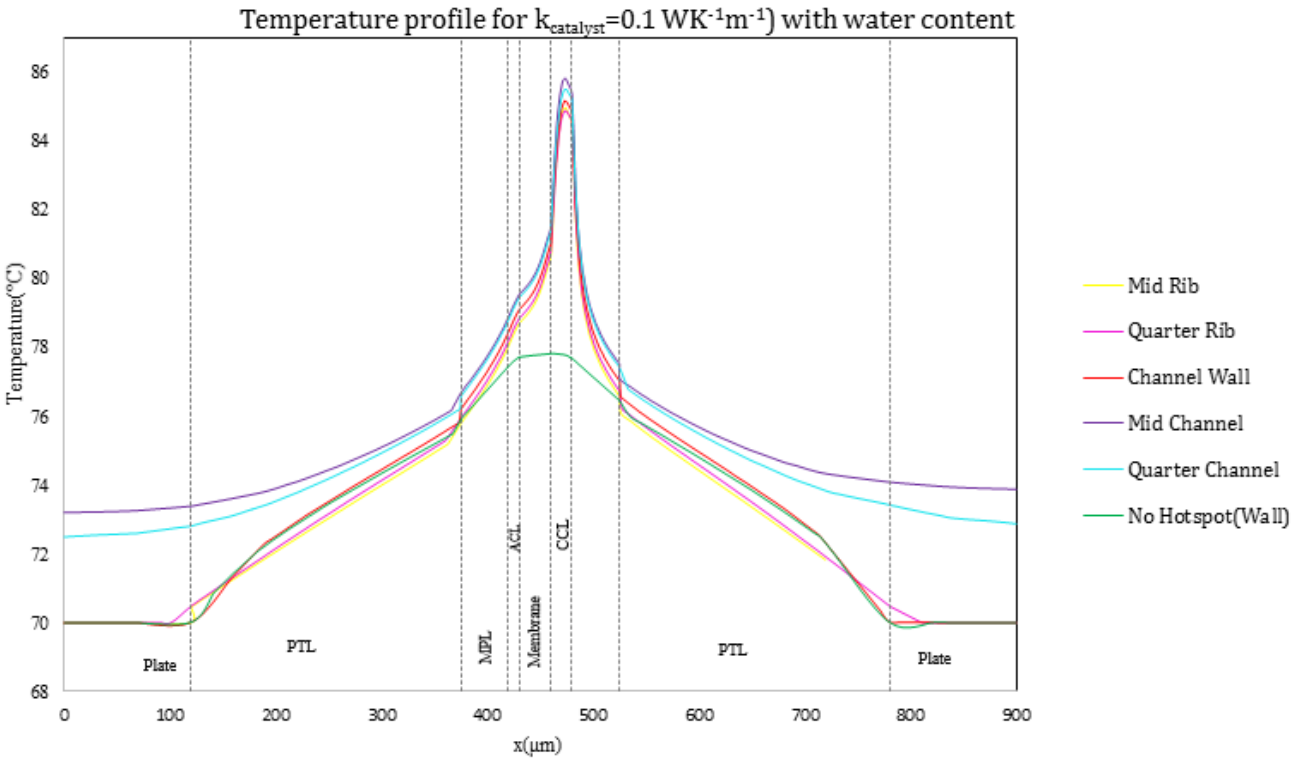

Figure 9: Temperature profiles from cut lines across the different PEFC layers

From the base case scenario with no water percolation and a thermal conductivity of 0.1 W/m K for the catalyst layers, it can be seen that the bell-curve temperature distribution becomes more uneven in the presence of a hotspot/pinhole with a maximum jump of nearly 9 °C in the CCL. The maximum temperature reached in the domain, which is the parameter of interest in this work, is located in the CCL. This can be explained by the presence of a more significant heat source at the CCL due to the crossover reaction between the hydrogen from the anode and the oxygen from the cathode taking place at this location. Indeed Nishimura *et al.*[72], found that the temperature of the reaction surface is 3-9 °C higher than the initial operation temperature while the relative humidity of the supply gas does not affect the temperature of the reaction surface significantly. At an operating current density of 1 A cm^{-2}, Pharoah *et al.*[40], demonstrated in a 2D model that the maximum temperature of the MEA is elevated by 4.5-15◦C compared to the polarisation plate temperature and that the maximum temperature, which occurs under the land in

the anode catalyst layer, is 3.5 ˚C above that of the bi-polar plate. Nandjou *et al.*[73], validates their 3D pseudo model by comparing their simulated results to a printed board circuit sensor plate inserted in the middle of the stack of 30 cells. They found a 3-6˚C temperature difference between the CCL and bipolar plate and hot zones on the cell surface were associated with a low cooling water velocity.

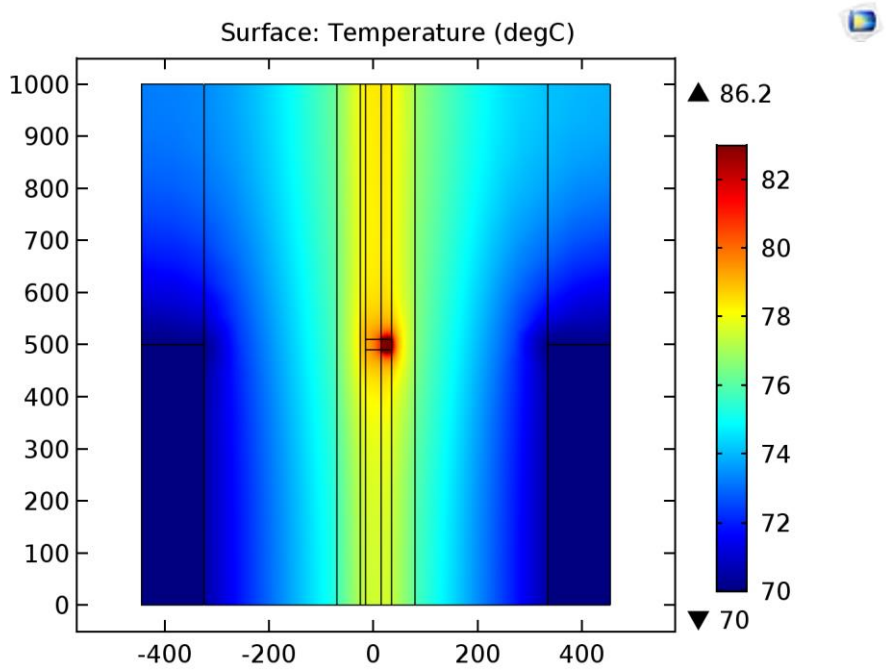

Figure 10:2D Plane view of Channel Wall Hotspot-Base case Scenario

A cross-sectional 2D XY plane view for the Channel Wall hotspot, that is located at the wall of the channel/land, is shown in the Figure 10. The Gas diffusion layer or Porous transport layer with its low thermal conductivity acts as an insulation layer around the conductive catalyst layer. Hence, this limits the heat which can be dissipated by direct conduction through the highly conductive ribs. It can be observed that the temperature under the land is cooler than that under the channel. This is expected due to the direct conduction to the flow field plates which have a high thermal conductivity. Hence, the heat generated due to the hotspot is mostly removed through the ribs to the channels of the flowplate. The temperature distribution obtained in the base scenario, in Figure 10, shows that a more important amount

of heat is dissipated through the anode flow channel than through the cathode. This can be due to hydrogen having a thermal conductivity which can be up to 10 times the value of humidified air. As a result of the lower temperature under the land, there may be condensation of water happening under the rib. According to Weber *et al.*[74], this is removed from under the land through evaporation or in-plane flow toward the gas channel. Further significant heat removal from catalyst layer can occur due to the phenomenon of Phase Change induced flow as described by Weber *et al.*[74]. This can eventually lead less steep temperature gradients within the PEFC.

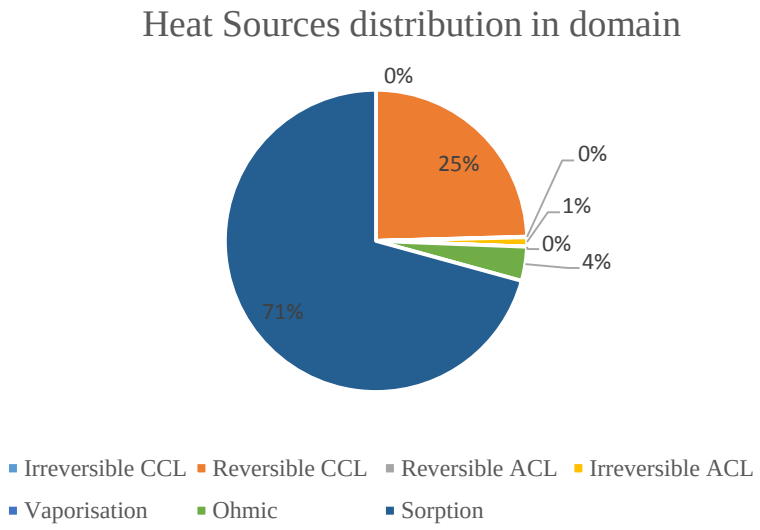

Figure 11: Heat sources/sinks distribution

A comparison of the heat sources and heat sinks distribution in the domain for the Channel Wall hotspot, at the rib wall, is shown in Figure 11. The heat of sorption, reversible heating at the cathode, and ohmic heating in the membrane account for 71 %, 25% and 4 % respectively. The other heat sources are quite negligible. The heat sources distribution was determined by considering the integral (summation) of the sources at all points in the domain. Despite that the heat of sorption is the most important contribution,

the rate of sorption/desorption, that is the time constant, is not clearly defined and different values are used by different research authors.

3.4 Preliminary Sensitivity study

A parametric study was done to assess the effect of partially flooded electrodes by arbitrarily implementing liquid water fraction in the different layers of the PEFC.

3.4.1 Effect of thermal conductivity in the presence of water content in porous layers

In the preliminary simplified model, a water fraction of 0.30, 0.50 and 0.80 has been assumed in the PTL, MPL and CL on the cathode side respectively while an isotropic thermal conductivity of the CL has been varied from 0.1 W/m K to 1.0 W/m K. The anisotropic factor of the MPL and PTL have been kept at its base case value of 10. The water fraction is accounted for by volume averaging the thermal conductivity of the concerned porous layer with the thermal conductivity of water. The obtained effective thermal conductivity is an input to equation (2.2).

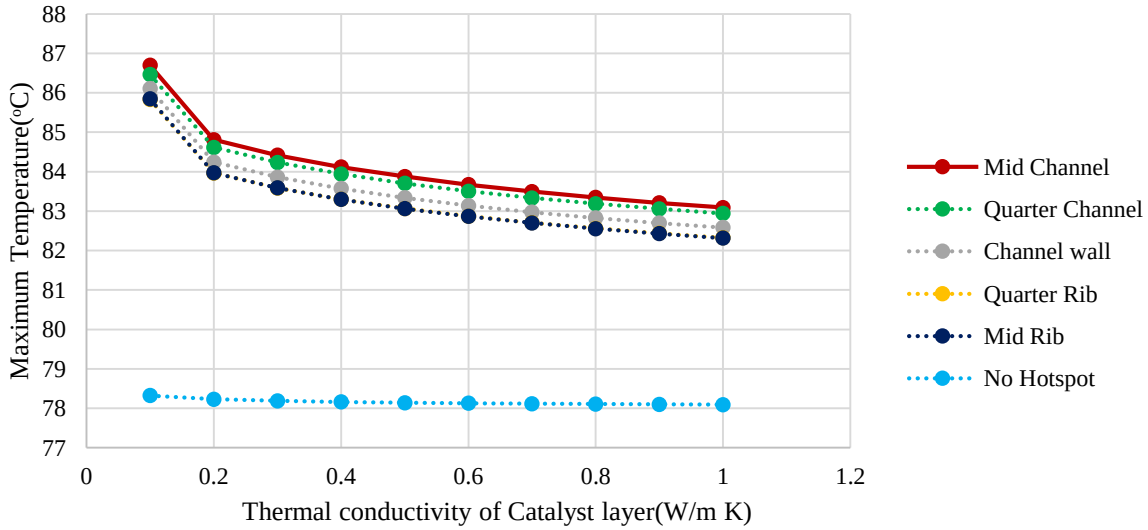

Figure 12: Effect of Thermal Conductivity of the Catalyst layer (W/m K) on the Maximum temperature (°C) in Stagnant Condition

There is a steep decrease in the maximum temperature for all hotspots locations as thermal conductivity is increased from 0.1 W/m K to 0.4 W/m K. As the thermal conductivity values is increased beyond 0.5 W/ m K, the decrease in the maximum temperature become negligible. The literature values for the thermal conductivity values of the CL varies between 0.04[18] and 0.39 W/m K[19]. The steepest decrease in the maximum temperature occurs within this range. When the thermal conductivity is increased from 0.1 W/ m K to 0.5 W/m K, in stagnant condition, the maximum decrease is 3.25% at the Mid Channel (at the centerline of the channel) while the minimum is 3.19% at the Quarter Channel (midway between the midplane of the channel and the rib wall).

3.4.2 Effect of thermal conductivity of MPL

Similarly as for the parametric study on the thermal conductivity of the CL, a constant water fraction of 0.30, 0.50 and 0.80 has been set in the PTL, MPL and CL on the cathode side respectively. Based on the literature [27], the value of the through-plane thermal conductivity of the MPL has been varied from 0.05 to 0.15 W/ m K. The in-plane value of the PTL is still set at 10 times of that of the through-plane. The thermal conductivity of the PTL and CL are kept constant at the base case scenario values. For the base case scenario, a value of 0.084 W/m K was used for the MPL thermal conductivity. According to Burheim *et al.* [27], this could correspond to an MPL with 25% PTFE and compressed at 9.2 bar or an MPL with 15% PTFE and compressed under 4.6 bar.

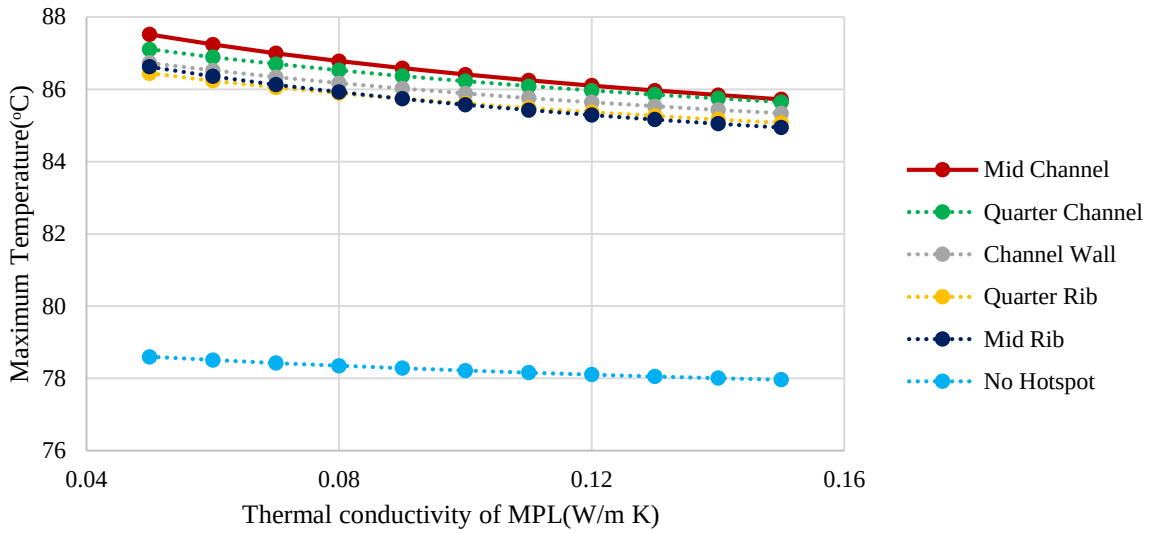

Figure 13: Effect of Thermal Conductivity of MPL (W/m K) on the Maximum temperature (˚C) in Stagnant Condition

In the Figure 13, an increase in the thermal conductivity of the MPL only has less impact on the maximum temperature of the domain compared to an increase in the thermal conductivity of the CL. This confirms that the thermal conductivity of the catalyst layer is a more important parameter in heat management.

3.4.3 Effect of anisotropic thermal conductivity in the presence of water content

Beyond an increase in the anisotropy factor to a value of 5, there is not a significant decrease in the maximum temperature in the domain as shown in Figure 14. Hence, it can be concluded that an in-plane

thermal conductivity which is 4-5 times the magnitude of a through-plane value is sufficient to cause a drop in the maximum temperature in the domain.

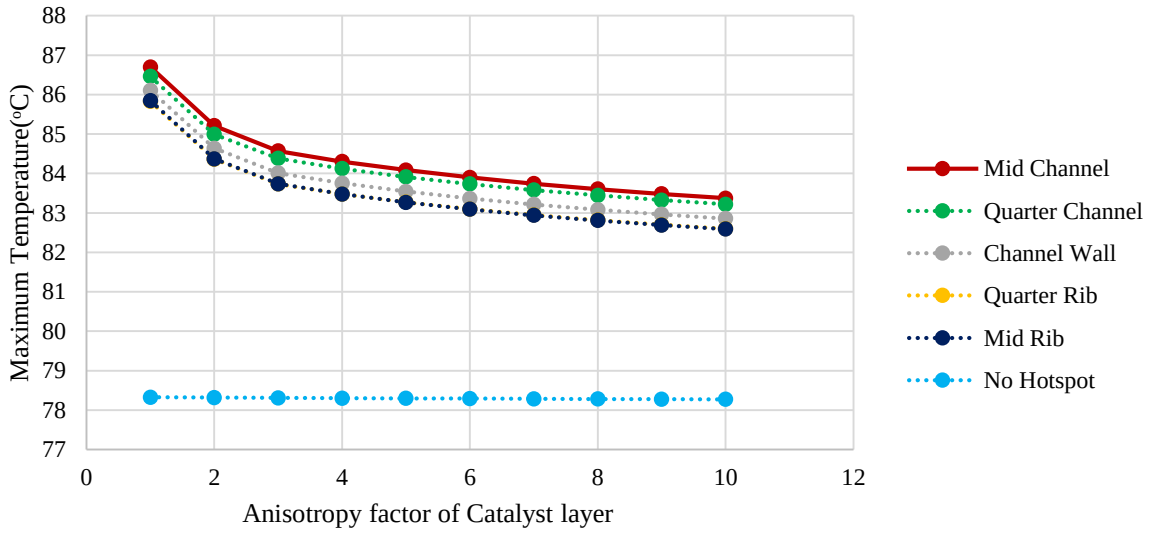

Figure 14: Effect of the Anisotropy factor of the CL on the Maximum temperature (˚C) in Stagnant Condition for a constant through-plane thermal conductivity

For the stagnant condition, when the anisotropy factor is increased by 50%, a maximum decrease of 3.01% occurs at the Mid Channel (at the channel centerline) while the minimum is 2.95% at the Quarter Channel (between the midplane of channel and the rib wall).

Anisotropy is a parameter which could be engineered through alternative fabrication techniques. For instance, the microstructure of the catalyst layer manufactured by the doctor-blade, meyer rod, piezoelectric printing, airbrush spray deposition and screen printing will most likely differ from each

other. In the case of the PTL, Todd and Mérida[75], have developed a method to produce controlled in-plane anisotropy for the PTL through fibre-alignment by electrospinning technology. They demonstrated that better performance was achieved with electro-spun PTLs with greater anisotropy magnitude. Hence, the anisotropy of the PTL is a parameter that can indeed be engineered to control not only the electrical performance but also thermal management in the PEFC.

3.4.4 Impact of varying water content in the porous layers

In this case study, the thermal conductivity of the different layers have been kept constant as per the base case scenario. The CL is considered as isotropic while an anisotropy factor of 10 is set for the MPL and PTL. The maximum saturation of the CCL is set at 80% while the water content of the PTL and MPL on the cathode side are varied as per Table 11. On the anode side, the voids spaces in the porous layers are filled with hydrogen only.

The fraction of liquid water in the porous layers refers to the percentage of the void spaces filled with liquid water. For an ideal gas mixture, the mole fraction (x_j) and volume fraction (y_j) for an ideal gas mixture are equivalent. A volumetric/ molar fraction has been set and has been converted to mass fraction using the following relationship:

$$\text{Molar fraction: } x_i = \frac{n_i}{\sum n_i} = \frac{y_i / M_i}{\sum y_i / M_i} \tag{2.30}$$

$$\text{Mass fraction: } w_i = \frac{m_i}{\sum m_i} = \frac{x_i M_i}{\sum x_i M_i} \tag{2.31}$$

Hence, the mass fraction is obtained from mass of species (mole fraction*Molar mass) divided by the total mass of all species (summation of all species' mole fraction*Molar mass).

The following physical properties of interest will be mass averaged: specific heat capacity, ratio of specific heats, thermal conductivity. The density of the mixture has been calculated from the ideal gas law. Instead of the mass fraction, volumetric fraction averaging could also be used for the density. Other methods of mixture averaging of the properties will be considered in the next chapter.

Table 11: Variation of water content in MPL and PTL on the cathode side

Combination	Volume fraction of water in MPL	Volume fraction of water in PTL
#1	0.4	0.3
#2	0.5	0.4
#3	0.6	0.5
#4	0.7	0.6
#5	0.8	0.7

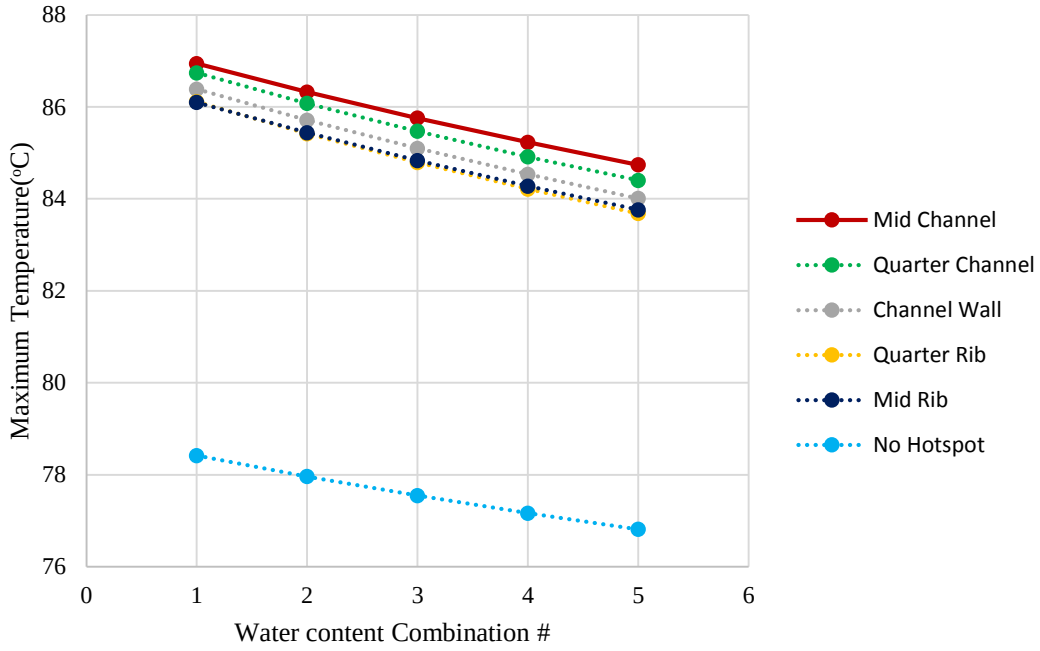

Figure 15: Effect of increasing water content on the Maximum temperature (˚C) in Stagnant Condition

As expected, a gradual increase in the water content of the porous layers on the cathode side contributes to a linear decrease in the maximum temperature reached in the domain. The average decrease for all hotspots location in the stagnant condition is 2.73 % when the water content of the MPL is increased from 40% to 80% and the water content of the PTL is increased from 30% to 70% while the maximum water content of the CL is 80%. For the stagnant condition, the maximum decrease of 2.83% occurs at the Channel Wall (also at Rib wall) while the minimum decrease of 2.53 % is at the Mid Channel (at the midplane of the channel).

Reverse water distribution from more saturated in PTL to less saturated in CL

Usually in gas diffusion layers without microporous layer, it is observed that liquid water moves from high water saturation regions to lower saturation regions through capillary-induced liquid water transport. However, in the work by Deevanhxay *et al.*[76], there is a reverse distribution of the liquid water accumulation when a microporous layer is included with the porous transport layer. Near the catalyst layer, the amount of liquid water in the microporous layer was low but increased toward the porous transport layer side under the rib. This accumulation under the rib can be explained by an increase in the amount of liquid at high current density. Indeed, the water vapor pressure can exceed the saturated vapor pressure in the catalyst layer as the current density increases. In turn, this cause liquid water to be transported in the cracks of the MPL which are connected to the pores in the PTL. The enhanced accumulation of liquid water toward the rib can also result from the inhomogeneous pathway in the MPL and the distribution of the porosity in a gas diffusion layer with an MPL. In that study[76], the porosities of the MPL and PTL were set to 0.35 and 0.84 respectively while the average liquid water saturation in the MPL and PTL were 0.08 and 0.27 respectively.

Hence, the water distribution in the previous parametric study will be reversed with a fixed saturation level of 80% in the PTL while the CL and the MPL water fractions, on the cathode side, are as follows:

Table 12: Variation of volume fraction of water in CL and MPL on the cathode side

Combination	Volume fraction of water in CCL	Volume fraction of water in MPL
#1	0.3	0.4
#2	0.4	0.5
#3	0.5	0.6
#4	0.6	0.7
#5	0.7	0.8

It can be seen in the below figures that a gradual reverse water content increase from the CL to the PTL on the cathode side while keeping the saturation of the PTL at 80%, leads to a slightly more significant increase in the maximum temperature in the domain than compared to the situation where the water content is more important at the CL and decreases towards the PTL.

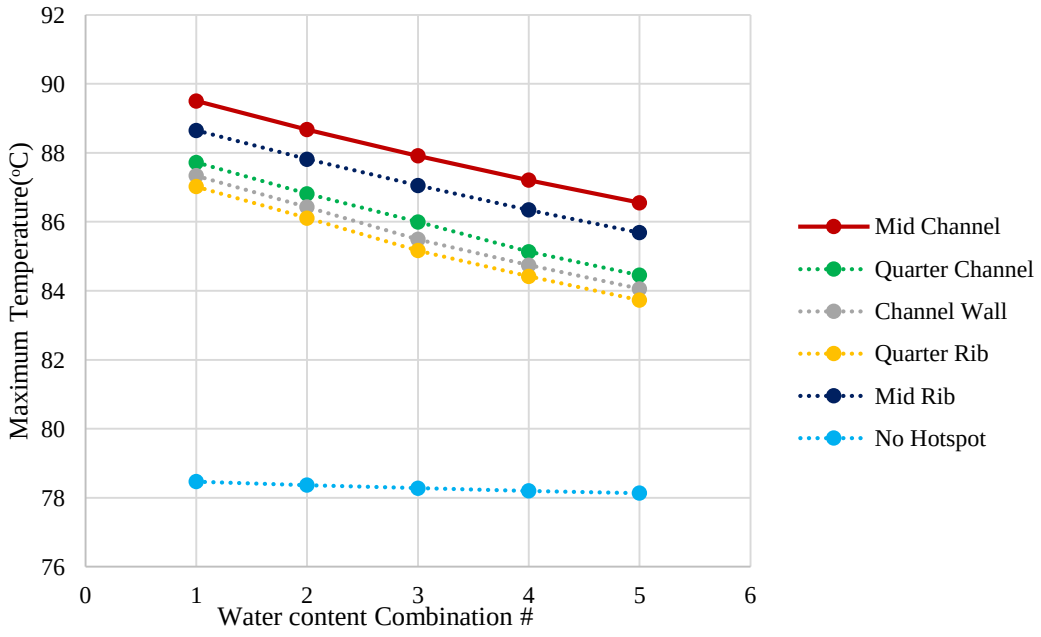

Figure 16: Effect of reverse water content on the Maximum temperature (˚C) in Stagnant Condition

3.4.5 Effect of Porosity of PTL

Porosity is an important input parameter since the effective transport coefficients such as the effective thermal conductivity is determined using this variable. Porosity of the PTL varies due to stress and compression. For example, under the land/rib, the porous layers are subject to a greater compressive force than under the channel, hence the porosity under the rib/land is lower than that under the channel. Actually , the porosity of an uncompressed PTL can be over :80% [15], as in the base case scenario of the current model, but it can be decreased down to 55-65%. Most original modelling work use a porosity of 40% which is an unrealistic value according to Pharoah *et al.*[15].

For the parameter analysis, we can decrease the PTL porosity from 80% to 40%, the MPL porosity will be changed from 50% to a constant 40% and the CL can be kept constant at 20%. Hence, the parametric study will be on a volume fraction of 20%-60% for the PTL, constant volume fraction of 60% for MPL and CL volume fraction of 80%.

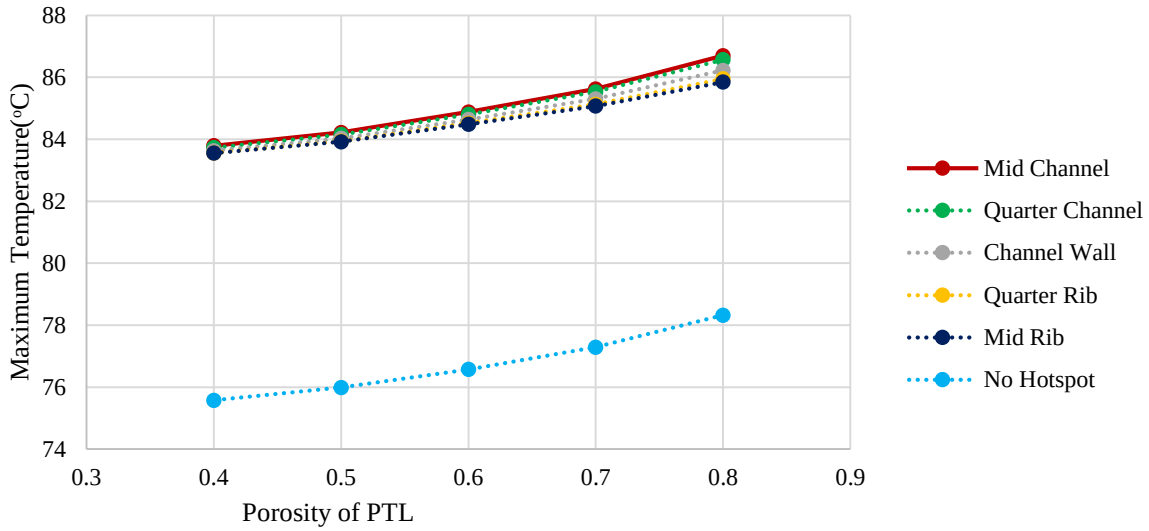

Figure 17: Effect of Porosity of PTL on the Maximum temperature (˚C) in Stagnant Condition

It can be seen in the above figures that as the volume fraction of the PTL increases (porosity of PTL decreases), the maximum temperature in the domain also decreases meaning that heat is better dissipated. This could be explained by an overall increase in the effective thermal conductivity due to a decrease in porosity. The volume occupied by the PTL fibres, which are highly conductive, increases and hence conducts heat more efficiently away from the heat sources in the CL. Hence, this reduces the maximum temperature in the domain. This trend is less significant for the Mid Rib and Mid Channel hotspot.

3.4.6 Effect of thickness of the layers in the presence of water

Parametric studies have been performed to investigate the impact of the thickness of the layers of the PEFC on the maximum temperature in the domain. Three case studies have been considered:

1) Vary the thickness of the ML, CL, MPL and PTL all at the same time
2) Keep the MPL and PTL thickness constant and vary the ML and CL thickness only

3) Keep the ML,MPL and PTL thickness constant and vary the CL thickness only

A constant water fraction of 0.30, 0.50 and 0.80 has been set in the PTL, MPL and CL on the cathode side for all the case studies. The pinholes size (length) have also been adjusted as the layers of the membrane and catalyst layers are varied.

Table 13: Case Study 1: Variation of all PEFC layers

Combination	Thickness(μm)					
	ML		CCL	ACL	MPL	PTL
# 1	25.4	Nafion 111	10	10	30	127.5
# 2	50.8	Nafion 112	20	20	60	255
# 3	127	Nafion 115	30	30	90	382.5

As it can be shown in the Figure 18, Figure 19 and Figure 20 below, the thickness value of the different layers of the PEFC has by far the largest effect on the maximum temperature in the domain. The maximum temperature reached is up to around 100 $^{\circ}$C for all the locations when the thickness of all the layers are increased. As the thickness of the ML and CL is increasing in the parametric studies, the surface area of the crossover reaction in the pinhole is also increased leading to a more significant heat source in this region. In addition to the insulating capacity of the increasing thickness of the PTL in the first case study, this amplified pinhole heat source can explain the tremendous increase in the maximum temperature in the domain.

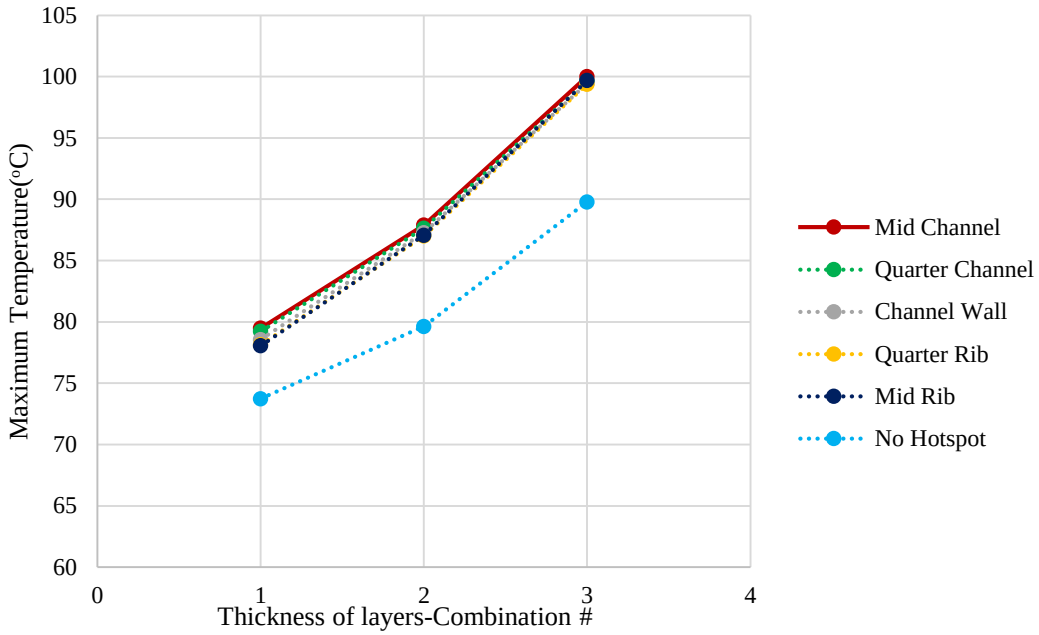

Figure 18: Effect of increasing thickness of layers on the Maximum temperature (˚C) in Stagnant Condition

In the second case study, the thickness of the MPL and PTL have been kept constant at 30 µm and 127.5 µm respectively while the thickness of the catalyst layers and the membrane layer have been increased as per the combination in the Table 14, where the combination 1, 2 and 3 refers to Nafion 111,112 and 113.

Table 14: Case study 2: Variation of thickness of ML-CL layers

Combination	Thickness(µm)		
	ML	ACL	CCL
#1	25.4	10	10
#2	50.8	20	20
#3	127	30	30

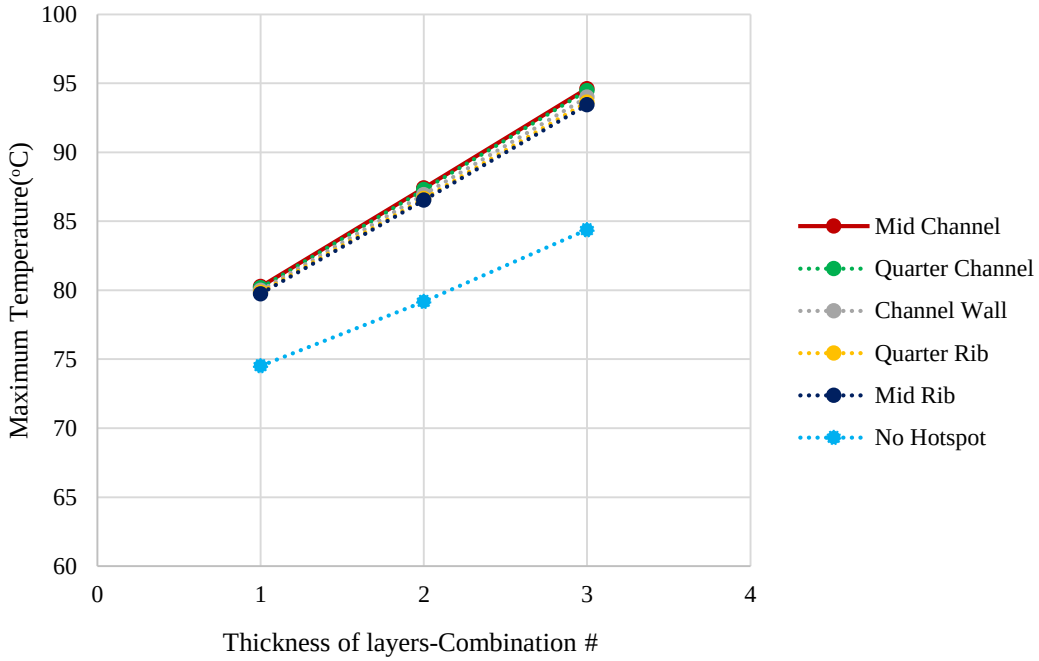

Figure 19: Effect of increasing thickness of ML-CL layers on the Maximum temperature (˚C) in Stagnant Condition

In the third case study, the thickness of the ML, MPL and PTL have been kept constant at 25.4 µm, 30 µm and 127.5 µm respectively while only the thickness of the catalyst layers have been varied from 10 µm to 30 µm.

Table 15: Case study 3: Variation of CL thickness

Combination	Thickness(µm)	
	ACL	CCL
#1	10	10
#2	20	20
#3	30	30

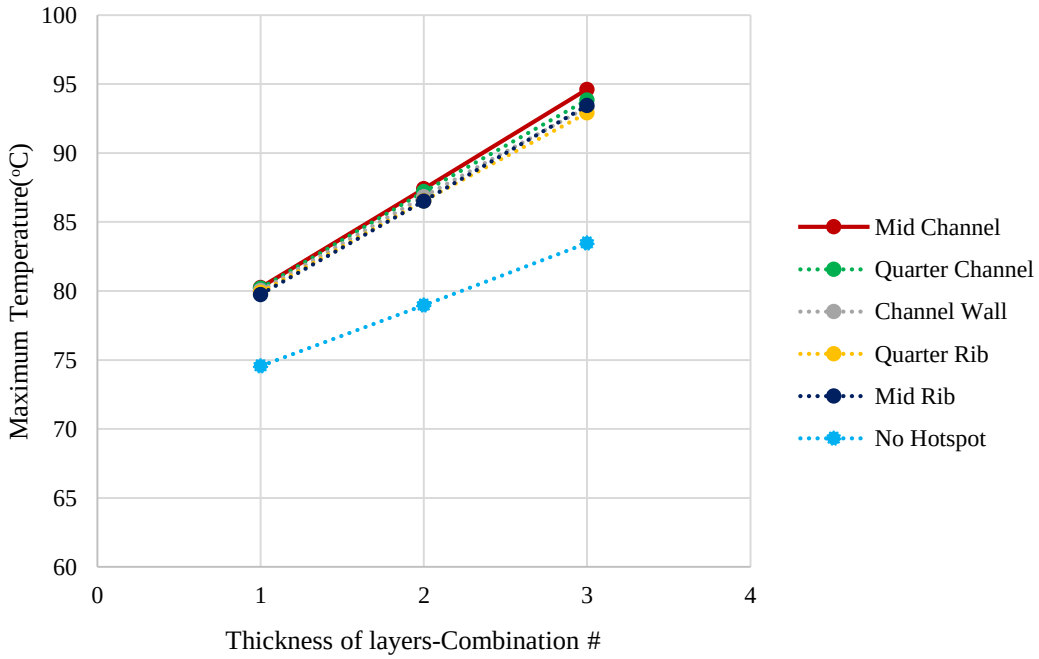

Figure 20: Effect of the thickness of CL layers on the Maximum temperature (˚C) in Stagnant Condition

In all the presented case studies, as the thickness of the layers increases, there is an increase in the maximum temperature. The effect in the case study 2 is nearly the same for the case study 3 in which the Nafion is kept constant at 25.4 um (Nafion 111) and only the thickness of the catalyst layer is varied. The thickness of the catalyst layer does not seem to play a role in heat dissipation. The maximum temperature reached is at least 5°C higher for all hotspots locations in the first case study where the PTL thickness is increased. This can be explained by the MPL and PTL acting an as insulation layer around the membrane electrode assembly.

Apart from the thermal effect resulting from the dimensions of the layers, there are other implications regarding the geometry of the PEFC layers. For instance, the thickness of the membrane layer in the base case scenario corresponds to Nafion 111, which is quite thin and more susceptible to membrane defect. The optimum thickness of the MPL has been demonstrated experimentally to be around 50 µm [77]. The dimension of the MPL is indeed important for water management in the PEFC by ensuring that the size and saturation level of interfacial water droplets on the CL surface is reduced enough to allow enhanced gas diffusion into the CL for the electrochemical reactions[77]. The MPL also help to reduce the liquid water saturation in the PTL and improve gas diffusion by decreasing the number of liquid water breakthroughs into the PTL. Nam *et al.* [77], demonstrated that a thin MPL is not able to perform its mentioned role in term of water removal. Instead, the location of the large interfacial droplets is shifted from surface of CL to the surface of the MPL.

The flow field design has been shown to influence the temperature distribution, with the maximum temperature under the channel being higher by 1°C for the parallel flow field compared to the serpentine flowfield [40]. Pharoah *et al.* [40] demonstrated that increasing the land and channel dimensions lead to

an rise in the maximum temperature though a wider channel is desirable to reduce the presence of water droplets which might block the channel.

3.5 Conclusions and further works

To summarize the various parametric studies, a bar chart has been plotted to illustrate the relative change in the maximum temperature in the domain. This study is based on the range of literature values where available or possible assumptions in the case of the CL anisotropy and saturation level.

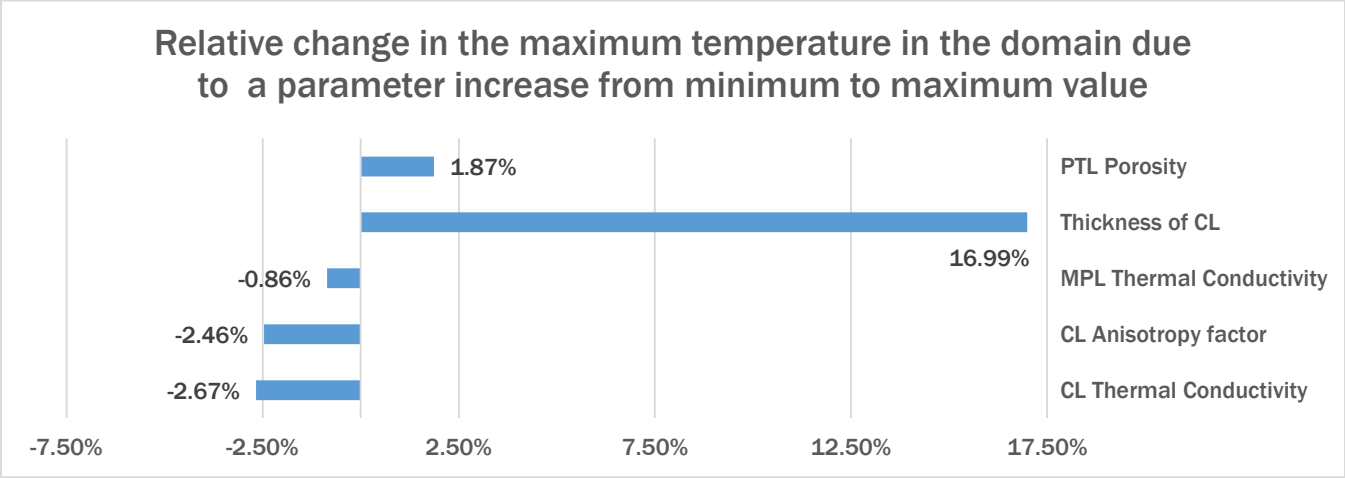

Figure 21: Relative change in the maximum temperature in the domain due to a parameter increase from minimum to maximum value

Table 16: Range of values considered for relative change in maximum temperature

Parameter	Minimum Value	Minimum Value
PTL Porosity	80%	40%
Thickness of CL	30 um	10 um
MPL Thermal Conductivity	0.05 W/m K	0.15 W/m K
CL Anisotropy factor	1	5
CL Thermal Conductivity	0.1	0.5

Minimizing the thickness of the different layers of the PEFC is desirable based on the sensitivity study but this is limited by other factors such as the robustness of the membrane and water morphology control of the MPL. Apart from reducing the temperature gradients within the cell, a thin CL can also help to keep the cost down. Pharoah *et al.* [40], also showed that the parameters with the greatest influence on the temperature distribution were the gas channel geometry (width and channel type), the thermal conductivity of the PTL and the state of water in the cell.

In this preliminary study, arbitrary saturation level and superficial velocity values have been assumed in each porous layers. Two-phase effects resulting from the interaction of the thermal and saturation profile have also been ignored. For instance, an increased water vapor saturation pressure and a rise in the water fraction in the vapor phase are expected as the temperature increases. In the next chapter, the model has been refined to account for these two-phase effects. The current physics have been coupled with the two phase D'Arcy flow in which the capillary pressure is a function of the saturation. Other physical properties which plays a role in two-phase flow, such as the viscosity, density and surface tension, are also a function of the temperature in the domain. The parametric studies have then been updated accordingly.

Chapter 4 Two-phase thermal model with water percolation

4.1 Two-phase effects

For the PEFC, the flow will remain gas-phase as long as the water vapor pressure does not exceed the saturation pressure. On the other hand, the thermal distribution is interlinked with both the electrochemical performance and the water management aspect of the PEFC. Indeed, an increase in temperature results in a change in the activation potential as well as in the local saturation pressure conditions. In turn, this could lead to a modification in the liquid water content in the system. A model based on single-phase flow will thus not be able to account for the liquid water. It is known that cell flooding at the interface between the gas diffusion layer and catalyst layer can also result in performance loss and mass transport resistance[12]. However, the effect of the high thermal conductivity of liquid water on the temperature distribution has not yet been investigated. Hence, the model has been modified to take into consideration the thermal effect resulting from a moisture content in the porous layers of the PEFC. Liquid water presence has been considered only on the cathode side. Indeed, water is produced in the liquid form at the cathode catalyst layer. However, water can also build up on the anode depending on operating conditions.

Ge *et al.* [78], determined through synchroton x-ray imaging that the temperature gradient should be considered in two-phase flow modelling since it impacts the liquid water distribution due to the capillary pressure effect. Actually, an elevated temperature reduces liquid water content due to more vapor phase transport but it also increases liquid water content due to a lower capillary pressure. For instance, at the

CCL-MPL interface, the liquid saturation increases from 0.29 to 0.40 as the temperature increases from 40 to 60°C. Hence, this author proposes that the temperature gradient can indeed be optimized to control liquid water accumulation[78].

A water vapor-pressure gradient results from the thermal distribution in the fuel cell. This phenomenon which causes water to be transported along that gradient is termed Phase Change Induced flow (PCI) [74]. When the water vapor reach the cooler land region, it condenses and this phase change releases heat. However, PCI flow leads to more water flowing through the pores toward the channel. This results in increased mass transfer resistance for the air which has to diffuse against the water flux towards the cathode. The pressure of liquid water can also lead to a decrease in the local fuel and oxidant mass diffusivities[65]. Weber *et al.* [74], points out that at higher current densities, the rate of heat generation overtakes the rate at which water is produced.

Two-phase flow is highly complex. The wetting and de-wetting behaviour depends on the capillary pressure level which is in turn related to the degree of the hydrophilicity and hydrophobicity of the diffusion layer. The saturation of the gas diffusion layers is linked to membrane hydration. The regime of the flow itself take the form of diverse configurations as described by Buongiorno [79] and Mench[1] : bubble, disperse bubbly, plug/ slug, churn or froth, annular, mist and stratified. Bazylak[80] provides a significant review of visualization techniques for liquid water transport. Indeed, there are various mechanism for liquid water accumulation and transport proposed by different authors such as branching geometry, tree-like water percolation, channelling and fingering accompanied by dynamic eruptive which has been observed in some in-situ visualization. However, all these mechanisms can be happening at the same time within the complex porous transport layers. Through ex-situ fluorescence microscopy

visualization, Lister *et al.*[81], demonstrated that the water is transported by fingering and channeling rather than by converging capillary.

4.1.1 Darcy's Law

To account for the two-phase effects, the model has been refined further by coupling the heat transport physics in the base case scenario with the two phase Darcy flow, which enables modelling of the convective multiphase liquid water transport in the porous electrodes. The two-phase Darcy law is basically a momentum equation in which the velocity field is described by the permeability, the fluid viscosity and the pressure gradient across the media[82]:

$$u = \frac{\kappa}{\mu} \nabla p \tag{3.1}$$

u: Darcy velocity vector [m/s]

κ: Permeability of the porous medium [m^2]

μ: Dynamic viscosity of fluid [Pa·s]

p: Pressure of fluid [Pa]

The velocity field obtained from solving the two-phase Darcy's Law is coupled with the velocity field in the heat transport equation. Similarly, the temperature is a property which is an input to the water

saturation pressure, viscosity of the fluid, density, capillary pressure, heat of evaporation/condensation, etc.

Darcy's flow has been considered due to low permeability and slow flow through the porous media.
The following assumptions have been considered for the two-phase Darcy flow:

- Immiscible flow. This means that the liquid and gas phase do not mix. However, it is quite likely that some gas phase will dissolve into the liquid phase.
- A uniform contact angle is assumed for each layer since the wetting property of the anisotropic layers can be really complex for numerical modelling.
- Gravitational forces is negligible compared to the surface tension forces. However, this might not hold true in the in-plane direction.
- The gas phase pressure is assumed to be constant. Since the capillary pressure is the difference between liquid phase and gas phase, this means that the capillary pressure is approximately equal to the liquid phase pressure.
- The temperature of the solid wall is assumed to be the same as the pore volume, hence all phases are at the same temperature and phase equilibrium holds.
- Diffusion is considered in the through plane direction only since the flow velocity down the channel is much lower.
- Air enters and water leaves the porous region in the down channel direction only on the cathode side while the fluid in the porous layers of the anode are considered stagnant.

The Darcy flow equation is quite limited in the sense that it was empirically derived from experiments studying the flow of water through sand beds [1].

4.1.1.1 Permeability

Since two phase is considered where both liquid and gas will be occupying pore space, it can be expected that the flow of a phase will be constrained due to the presence of the other phase. This resistance to flow in a two-phase transport is characterised by a physical property known as the effective permeability.

As a result, the two phase effective permeability κ will be obtained by correcting the intrinsic/absolute permeability k_{abs} of the porous media by the relative permeability κ_{rl} for a phase:

$$\kappa = \kappa_{abs} \bullet \kappa_{rl} \tag{3.2}$$

The relative permeability k_{rl} is a function of the saturation of the wetting phase[65]:

$$\kappa_{rl}(s) = \begin{cases} s^{v} & for\ wetting\ phase \\ (1-s)^{v} & for\ non-wetting\ phase \end{cases} \tag{3.3}$$

In the modelling work by Songprakorp[65], based on the standard Wyllie relative permeability correlation, a value of v=3 is used in the catalyst layer, and v=4.5 is used in the gas diffusion layer.

Kumbur *et al.*[83], proposed a relative permeability correlation based on an empirical curve fit obtained from experimental capillary pressure data from tested fuel cell media:

$$\kappa_{rl}(s) = s^{2.16} \tag{3.4}$$

This correlation is used in this work instead of the Wyllie correlation which was adapted for fuel cells from non-consolidated sand studies. However, different diffusion media were tested under no compression

to obtain the correlation by Kumbur *et al.*[83]. Bhaiya[53] similarly used a value of v=2.16 for all layers in their modelling work.

Liquid water is stagnant in the pores until a minimum saturation s_{min} is reached, which is known as the irreducible saturation s_{irr}[53]:

$$s_{min} = \frac{s - s_{irr}}{1 - s_{irr}} \tag{3.5}$$

The liquid water saturation s is defined as the fraction of pore volume available to liquid water [53]:

$$s = \frac{V_l}{V_{pore}} \tag{3.6}$$

Since the irreducible saturation can be considered as zero as in previous work[53], the same can be assumed here for all layers.

For the absolute permeability of the gas diffusion layer, a value of 10^{-12} m^2 has usually been used as in the works of Songprakorp[65] ,Wang *et al.*[84] and Mench[1]. Bhaiya [53] used a value of 1.8×10^{-11} m^2 for the PTL and a value of 1.5×10^{-13} m^2 for both the MPL and CL. Actually, the same value was assumed for the CL due its comparable microstructure to the MPL and the unavailability of literature data[53]. The same approach has been applied in this current work.

The value of absolute permeability used in most models, that is 10^{-12} m^2 (1 darcy), is actually adapted from petroleum science. Instead, a more appropriate estimation can be obtained using the Carman-Kozeny equation, for which the mean radius of the pore size, the porosity and tortuosity must be known[1]:

$$\kappa_{abs} = \frac{r^2 \varnothing^3}{18\tau\left(1-\varnothing\right)^2} \tag{3.7}$$

4.1.1.2 Viscosity

The temperature impact the viscosity of the fluid which in turn influence the two phase flow.

The Sutherland's equation has been applied to describe the viscosity of air as a function of the temperature[85]:

$$b = 1.458\times10^{-6}\ \frac{kg}{m\,s\,K^{\frac{1}{2}}}$$

$$\mu\left[\text{kg.m}^{-1}.\text{s}^{-1}\right] = \frac{bT^{3/2}}{T+S} \tag{3.8}$$

In the case of air,

$$S = 110.4\text{K}$$

The viscosity of liquid water is greatly influenced by temperature as per the following relationship[86]:

$$\mu\left[\text{g.cm}^{-1}.\text{s}^{-1}\right] = \left(2.414\times10^{-4}\right)\times10^{\frac{247.8}{T-140}} \tag{3.9}$$

4.1.1.3 Capillary pressure

The driving force in the Darcy flow regime is the pressure gradient resulting from the capillary force:

$$P_C = P_{nw} - P_w = \frac{2\gamma\cos\theta}{r} \tag{3.10}$$

Where,

$$\gamma: \text{Surface tension} \left[\frac{\text{N}}{\text{m}}\right]$$

$$\theta: \text{Contact Angle}[\text{deg}]$$

$$r: \text{Mean radius of pore size}$$

It can be seen from the above equation that the capillary pressure is a result of a difference in pressure between the wetting and non-wetting phase. Important factors which control this force is the pore size of the porous media and the surface tension[1]. Hence, there will be higher capillary pressure in region of small pore size and lower capillary pressure as the pore size increase. This difference in capillary pressure leads to a flow from the region with small pore size to region with larger pore size, for instance, from the MPL to the PTL.

For PEFC modelling, the capillary pressure is often a function of the level of saturations through the Leverett relationship J(s)[1]:

$$P_c = \gamma \cos\theta \left(\frac{\varnothing}{k}\right)^{1/2} J\left(s_l\right) \tag{3.11}$$

$$J\left(s_l\right) = \begin{cases} 1.417\left(1-s_l\right) - 2.120\left(1-s_l\right)^2 + 1.263\left(1-s_l\right)^3 & \text{if } \theta < 90°, \text{ Hydrophilic} \\ 1.417 s_l - 2.120 s_l^{\,2} + 1.263 s_l^{\,3} & \text{if } \theta > 90°, \text{ Hydrophobic} \end{cases} \tag{3.12}$$

The surface tension drops as the temperature is increased since it is a function of the temperature[1]:

$$\gamma[\text{N/m}] = -1.78\times10^{-4}\left(T\right) + 0.1247 \tag{3.13}$$

If all the other conditions are held constant, the capillary pressure decreases as the surface tension is lowered.

The above presented generic Leverett function has been developed from soil science. Its applicability for the thin anisotropic layers of the PEFC is questionable. Indeed, to account for this different application, a modified Leverett function has been presented by Kumbur *et al.*[83], which takes into account the liquid saturation and the hydrophobic content:

$$P_C = \gamma \left(\frac{\varnothing}{k} \right)^{\frac{1}{2}} M\left(s_{nw}\right) \tag{3.14}$$

Where for, $0 < s_{nw} < 0.50$,

$$M\left(s_{nw}\right) = \%wt(0.0469 - 0.00152 \times \%wt - 0.0406 s_{nw}^2 + 0.143 s_{nw}^3 + 0.0561 ln s_{nw} \tag{3.15}$$

Due to the varying properties such as hydrophilicity, saturation and pore size, different capillary pressure relationship have been used in the different CL,MPL and PTL layers in the work by Bhaiya[53] .

The temperature and compression can also have an effect on the capillary pressure saturation relationship which is not captured by the above equations. Indeed, as the pore size becomes very small, there can be an increase in the gas phase pressure according to the Kelvin equation[1]:

$$R_a T ln\left(\frac{P_v}{P_o}\right) = \frac{2\gamma \hat{V} \cos\theta}{r} \tag{3.16}$$

As a result of this higher vapor pressure in the small pore as the total pressure increases, this can lead to an increase in the relative humidity and a decrease in the vapor mole fraction as per the below equation:

$$RH = \frac{y_{H_2O} P_{Total}}{P_{g,sat(T)}} = \frac{P_{vapor}}{P_{g,sat(T)}} \tag{3.17}$$

Consequently, this can cause condensation above the normal bulk condensation temperature. This is termed as capillary condensation[1]. Except for the membrane which may have holes at the nanometer scale, the other layers of the PEFC have pore sizes which are large enough to avoid this issue[1].

4.1.1.4 Liquid water source/sink terms

Inside the porous layers, water undergoes phase change that is it is either evaporated or condensed based on the water vapor pressure and the saturation pressure. Hence, the complete vaporization of water produced during the oxygen reduction reaction cannot be considered in the two-phase model and this assumption is dropped in this chapter where the two-phase effects are accounted for.

The following empirical equation can be used to account for the source term S_l, that is the interfacial mass transfer between liquid and water vapor due to both evaporation and condensation.[53] [87]:

$$S_l = K_{e/c} a_{lv} M_{H_2O} \left(p_v - p_{sat}(T) \right) \tag{3.18}$$

Where,

a_{lv} : Liquid water-vapour interfacial surface area per unit volume $\left[\text{cm}^2\text{cm}^{-3} \right]$

S_l : Source term for evaporated or condensed water $\left[\text{ g cm}^{-3}\ \text{s}^{-1} \right]$

p_v : water vapour pressure or partial pressure of water[Pa]

$p_{sat}(T)$: Saturation pressure of water[Pa]

M_{H_2O} : Molar mass of water $[\text{g/mol}]$

In the above equation, the source term becomes positive (Condensation), if the water vapor pressure exceeds the saturation pressure. Else, if the water vapor pressure is lower than the saturation pressure, the source term becomes negative (Evaporation).

The liquid water-vapor interfacial surface area per unit volume, a_{lv}, is a function of the saturation of the porous layer.

For the PTL(50% hydrophobic and 50% hydrophilic pores)[53]):

$$a_{lv} = 140 s^{1.15} \left(1-s\right)^{1.75} \tag{3.19}$$

For MPL(100% Hydrophobic pores) [53]:

$$a_{lv} = 9\times10^{4} s^{5} \left(1-s\right)^{1.25} \tag{3.20}$$

For CL(50% hydrophobic and 50% hydrophilic pores) [53]:

$$a_{lv} = 4.4\times10^{4} s^{1.25} \left(1-s\right)^{2.5} \tag{3.21}$$

The water saturation pressure is dependent on the temperature as per the below relationship [65][64]:

$P_{sat}\left(T\right)$: *Water saturation pressure*

$$Log\left(P_{sat}\left(T\right)\right) = -2.1794 + 0.02953\left(T-273.15\right) - 9.1827\times10^{-5}\left(T-273.15\right)^{2} + 1.4454\times10^{-7}\left(T-273.15\right)^{3}$$

.

The water vapor partial pressure P_{H_2O} is obtained as the product of the mole fraction of water vapor and (pressure). To make the computation less expensive, a hypothetical water vapor partial pressure P_{H_2O} is computed from the mass balance of the gaseous species, in the work by Nandjou et al[73], and the hypothetical saturation is obtained as follows:

If $P_{H_2O} \leq P_{sat}(T)$, then $s = 0$ (3.22)

If $P_{H_2O} > P_{sat}(T)$, then $s = \dfrac{P_{H_2O} - P_{sat}(T)}{\dfrac{\rho_L RT}{M_{H_2O}} - P_{sat}(T)}$ (3.23)

The above method can however lead to an underestimation of the real saturation.

Condensation rate constant: 1×10^{-4} mol/(Pa-cm^2-s) ([53], assumed), 1.0 Pa^{-1} s^{-1}([65])

Evaporation rate constant: 1×10^{-10} mol/(Pa-cm^2-s) ([53], assumed), 5×10^{-5} Pa^{-1} s^{-1}([65])

The condensation/evaporation constant is an unknown parameter in Bhaiya [53].

Instead of using condensation and evaporation rate constant, there are also models which considers the surface energy in the conservation and evaporation rates. In Songprakorp[65], kinetic theory is used to estimate mass transfer rate. Nusselt number and Schmidt number can also be used to determine a mass diffusion rate. Hu *et al.*[36], considered the condensation and evaporation rate coefficients to be infinite, under which definition, liquid water can only coexists with vapor which is saturated. The same value of 1×10^4 s^{-1} was used for the both the condensation and evaporation rate coefficients.

The heat source/sink term due to the phase change is given by the product of the water source term and the heat of Condensation/Evaporation:

$$S_{Heat} = K_{e/c} a_{lv} \left(p_v - p_{sat}(T) \right) \times \Delta H_{lv} \tag{3.24}$$

Evaporation: If $P_{H_2O} \le P_{sat}(T)$, $\Delta H_v = 242$ KJ/mol (3.25)

Condensation: If $P_{H_2O} > P_{sat}(T)$, $\Delta H_l = 285.8$ KJ/mol (3.26)

4.2 Sensitivity study with two-phase interactions

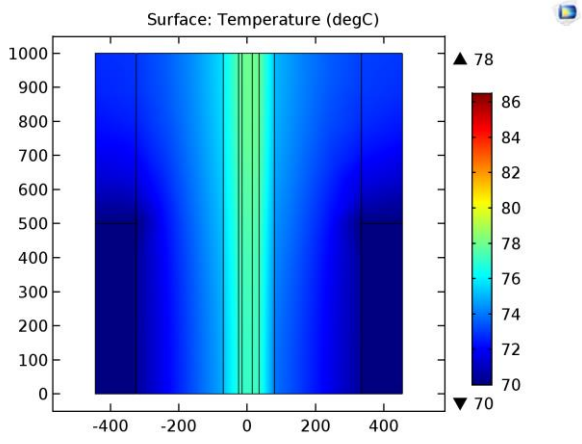

Figure 22: 2D XY Cut plane view- No Hotspot

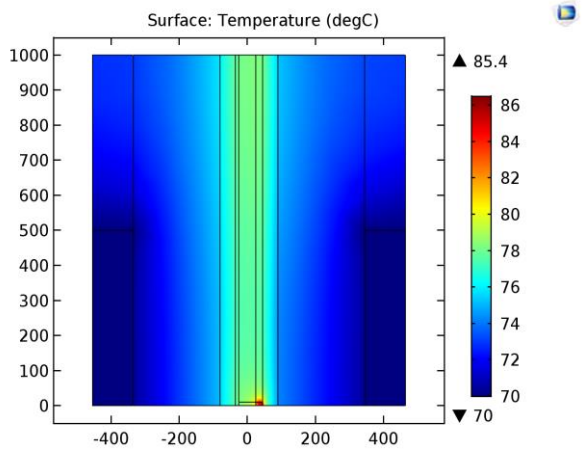

Figure 23:2D XY Cut plane view-Mib Rib

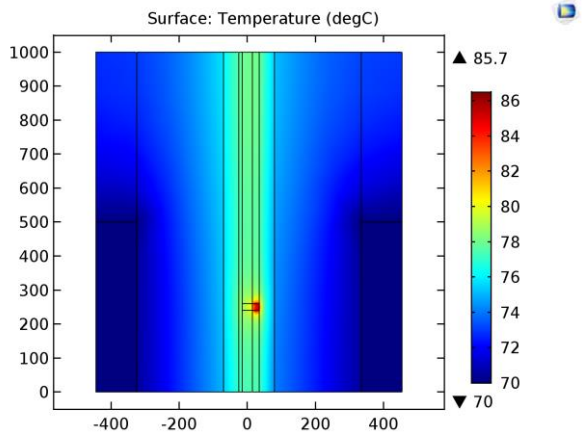

Figure 24:2D XY Cut plane view-Quarter Rib

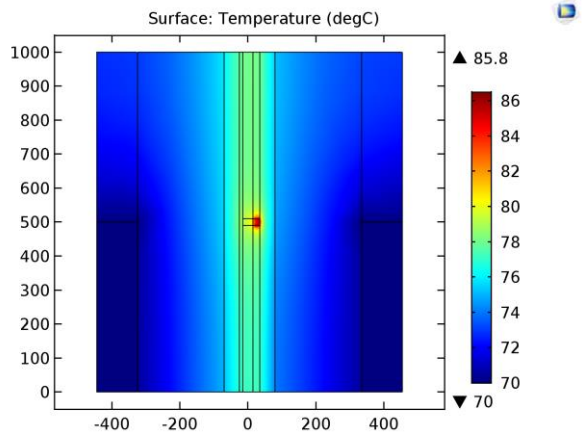

Figure 25:2D XY Cut plane view-Channel Wall

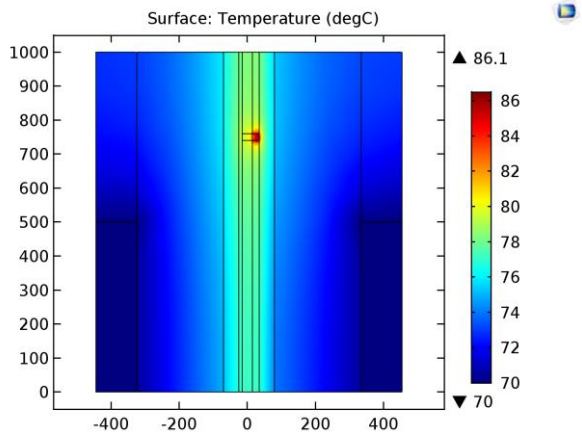

Figure 26:2D XY Cut plane view-Quarter Channel

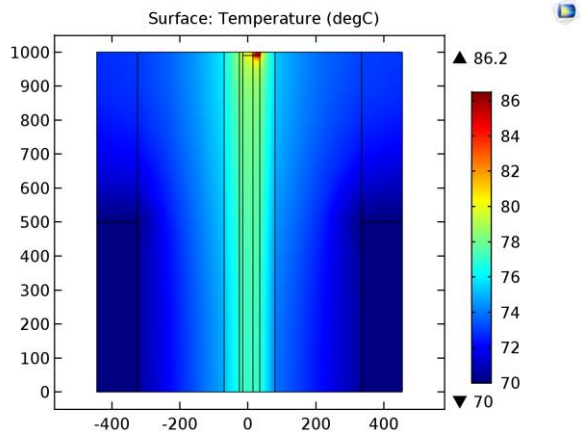

Figure 27:2D XY Cut plane view-Mid Channel

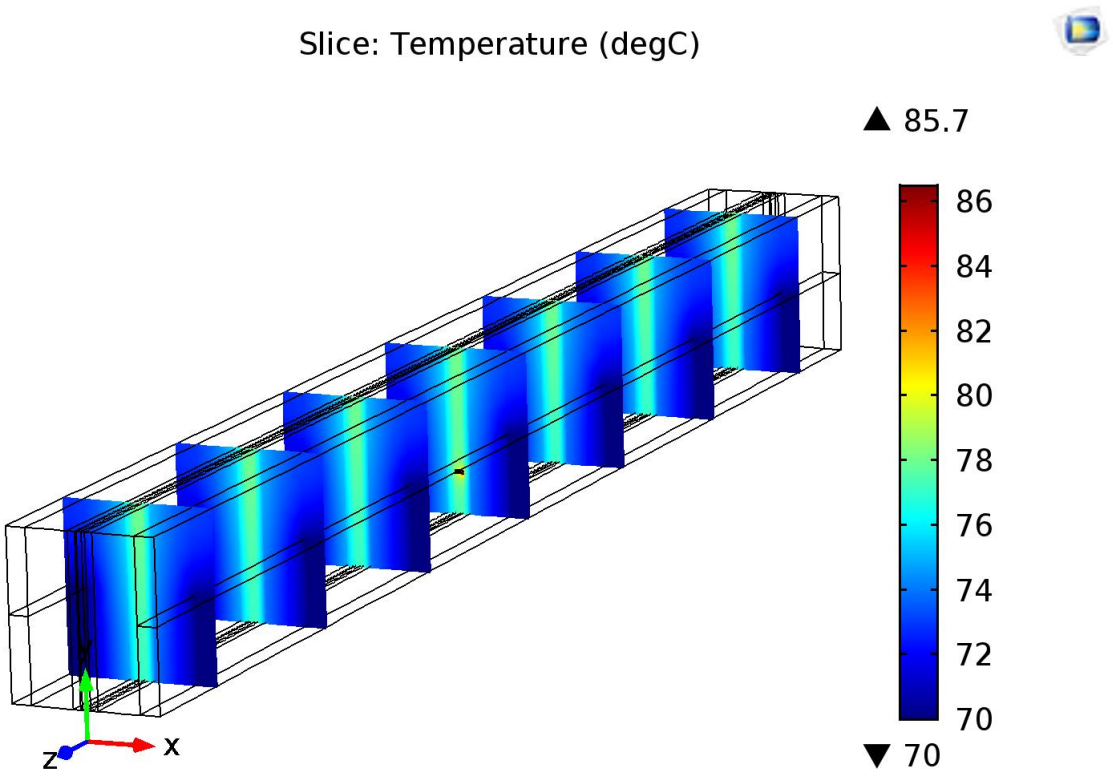

Figure 28: 3D XY Slice View- Quarter Rib

In this chapter, the temperature and saturation profiles have been coupled to include the influence of temperature on various physical properties of the fluid phases in the porous layers. In the Figures 23- 28, the temperature profile of the cut XY plane view of the domain can be observed for the coupled Two-phase Darcy flow thermal model for the case with no hotspot and for hotspots located at the centerline of the channel (Mid Channel), midway between the centerline of the channel and the rib wall (Quarter Channel), at the rib or channel wall, midway between the rib wall and the centerline of the rib (Quarter Rib) and at the centerline of the rib. In the presence of the hotspots, there is a maximum temperature of nearly 8°C compared with a model with no hotspot, while considering the base case value parameters.

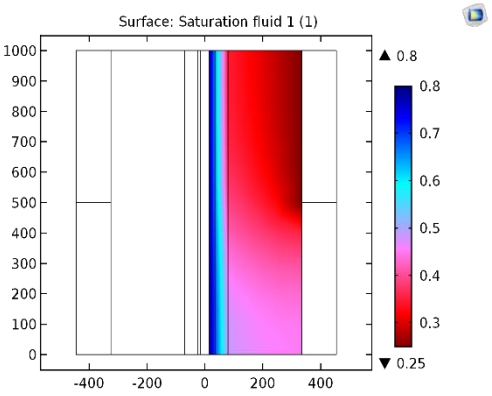

Figure 29: 2D XY Cut Plane View- Saturation profile for base case scenario

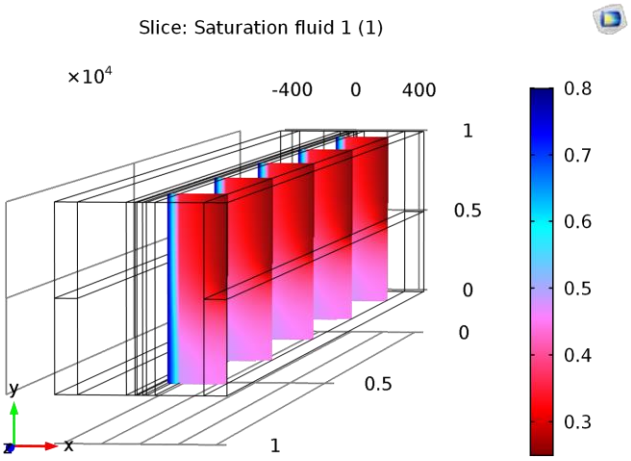

Figure 30: 3D XY Slice view- Saturation profile for base case scenario

As shown in Figure 2930 and Figure 30 31, the capillary flow is from high to low saturation regions with saturation being the highest in the catalyst layer and gradually decreasing toward the channel. The region under the rib wall is more saturated than under the channel due to condensation underneath the cooler rib surface.

4.2.1 Effect of thermal conductivity of CL

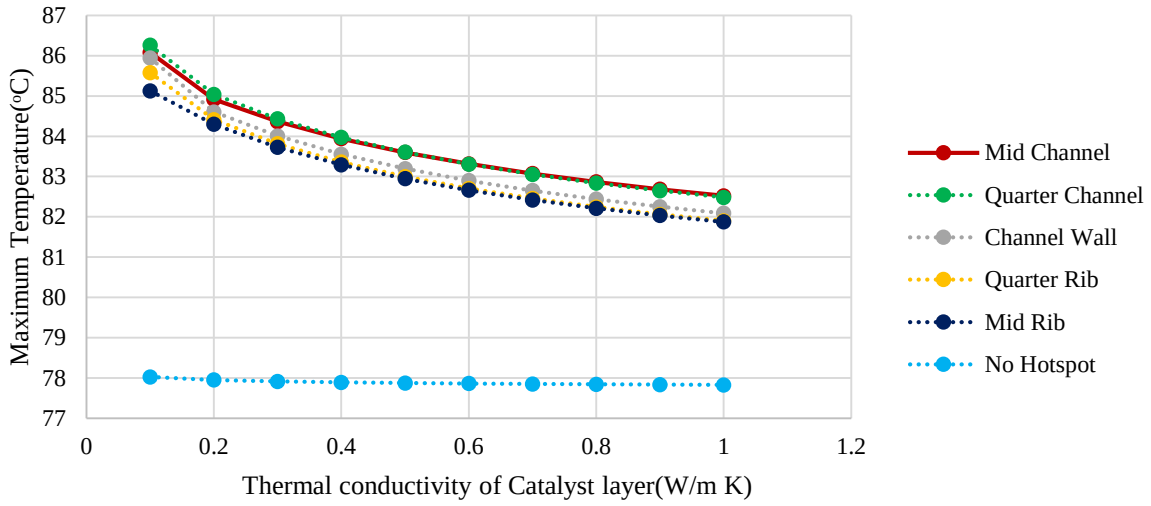

Figure 31: Effect of Thermal Conductivity of the CL (W/m K) on the Maximum temperature (˚C) in the presence of two-phase effects

The maximum temperature decreases more steadily as the thermal conductivity of the catalyst layers increases, in the case where the two-phase effects are considered, as shown in Figure 31. Compared to Figure 12, there is no steep decrease beyond a thermal conductivity value of 0.2 W/ m K. Similarly, the thermal conductivity has nearly no effect in the absence of a hotspot and only plays a role in the occurrence of pinholes. When the two-phase effects are considered, there is a drop of nearly 1˚C in the maximum temperature for all the positions at the base case value of 0.1 W/ m K. The presence of liquid water tends to mitigate the rise in temperature due to the hotspot. Based on the literature range of the CL thermal conductivity, an increase from the minimum value of 0.1 W/m K to the maximum value of 0.4 W/m K yields an average decrease of 2.53% of the maximum temperature in the domain.

4.2.2 Effect of thermal conductivity of MPL

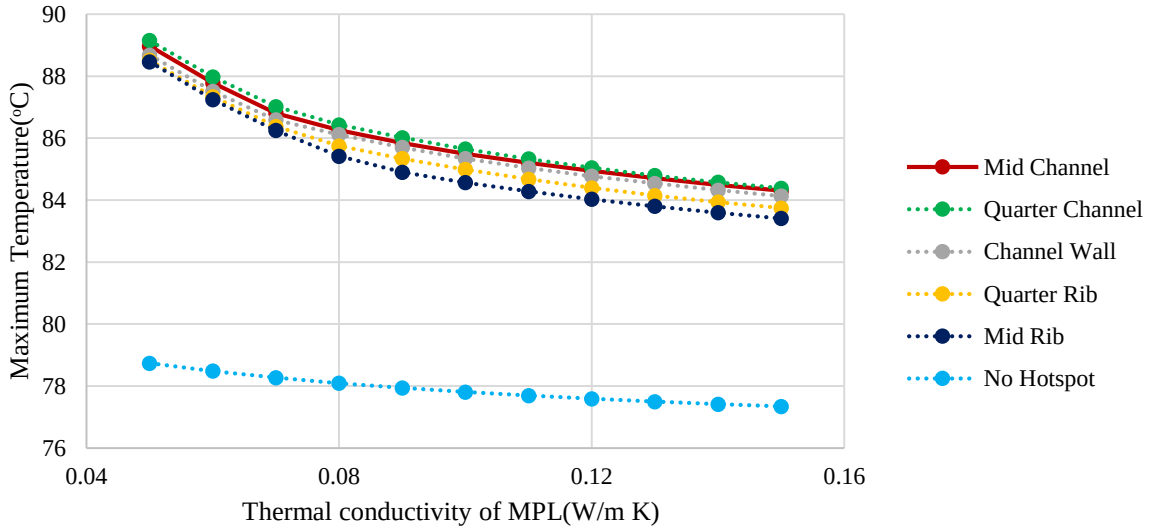

Figure 32: Effect of the Thermal Conductivity of the MPL (W/m K) on the Maximum temperature (˚C) in the presence of two-phase effects

Over the range of the thermal conductivity of the MPL considered, there is a larger decrease in the maximum temperature. For instance, for the Quarter Rib, the maximum temperature drops from 89°C to 84°C, when the thermal conductivity is varied from from 0.05 to 0.15 W/ m K as per Figure 33. In the case where the two-phase effect is neglected as per Figure 13, over the same range of thermal conductivity for the same location, the maximum temperature changes from 86.5 °C to 85.5 °C. Accounting for the two phase effects in the MPL shows that the its thermal conductivity plays a more important role in dissipating heat than suggested by the previous study ignoring the two-phase effect.

4.2.3 Effect of anisotropic thermal conductivity in the presence of water content

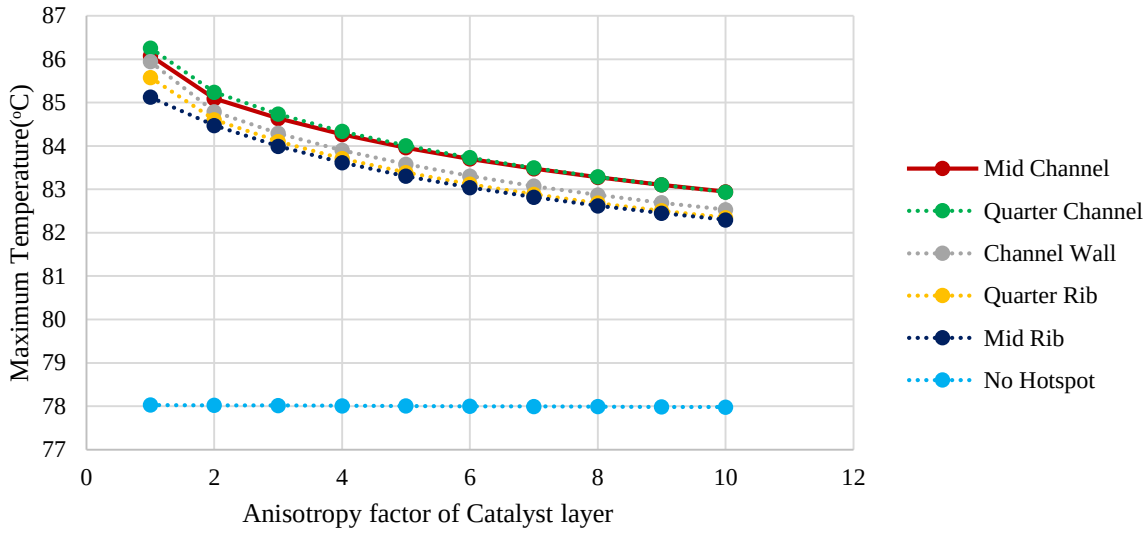

Figure 33: Effect of the Anisotropy factor of the CL on the Maximum temperature (˚C) in the presence of two-phase effects for a constant through-plane thermal conductivity

Compared to the Figure 14, the maximum temperature keeps on decreasing beyond the anisotropy value of 4-5. The rapid drop from the anisotropy factor of 2 to a value of 4 is not observed when coupling with the two-phase Darcy flow. The two-phase effect seems to overtake the impact of the anisotropy factor of the CL thermal conductivity and it also reduces the value of the maximum temperature for all positions over the range of the MPL thermal conductivity by about 1˚C. Cao *et al.*[88], explored the coupled effect of water and thermal transport for an anisotropic PEFC. A lower temperature difference of 3˚C is observed between the cathode channel/PTL interface and the CL/PTL interface when anisotropy is taken in consideration. In the isotropic condition, this difference is 4˚C. Similarly, in this work, anisotropy results in lowered thermal gradient.

4.2.4 Impact of varying water content in the porous layers

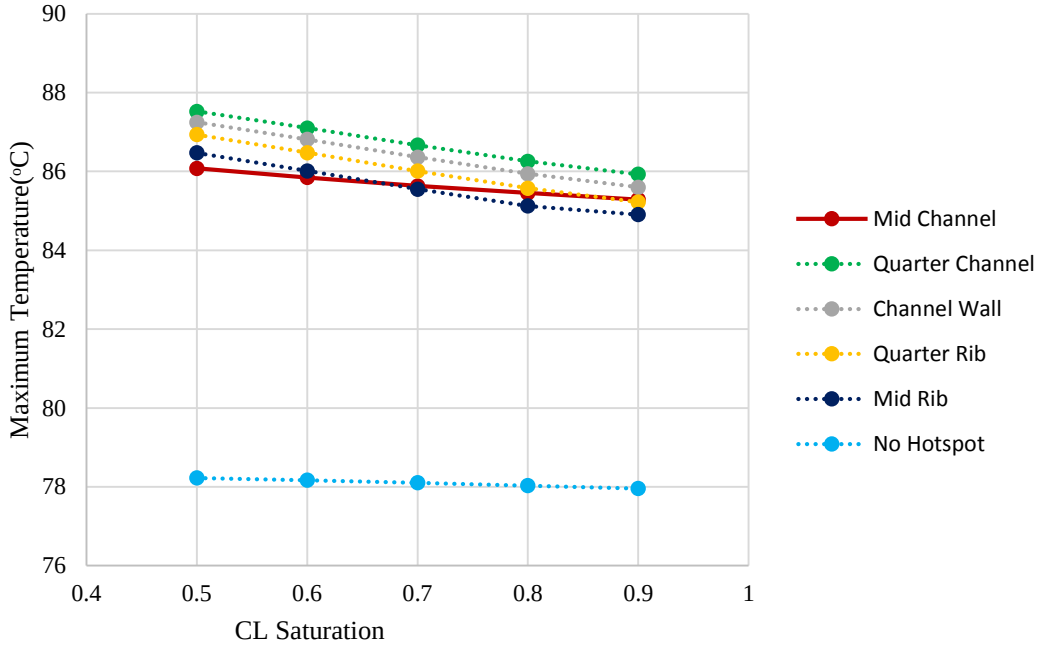

Figure 34: Effect of increasing CL saturation on the Maximum temperature (˚C) in the presence of two-phase effects

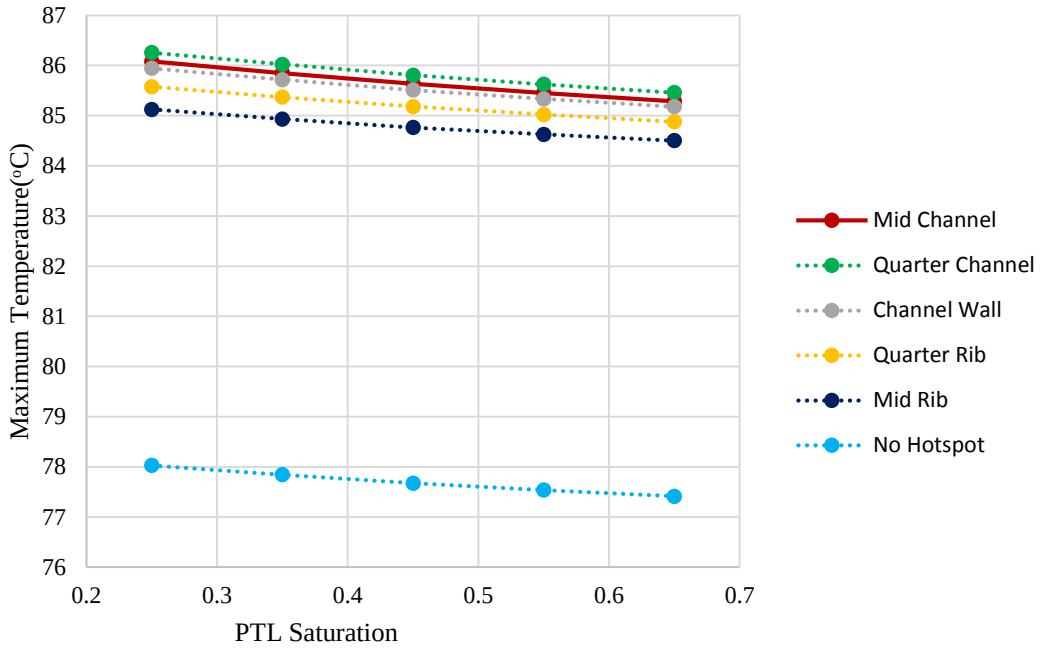

Figure 35: Effect of increasing PTL saturation on the Maximum temperature (˚C) in the presence of two-phase effects

In the Figure 35, only the saturation value at the CCL is varied from 0.5 to 0.9. This refers to the boundary condition at the interfacial wall between the CCL and the ML. As expected, an increase in the liquid water content at the CL leads to a reduction in the maximum temperature in the domain. Accounting for the two-phase effect instead of assigning arbitrary saturation value in each layers, results in a different maximum drop for all positions. At the Quarter Channel, with CL saturation of 0.8 as assumed in the chapter 3, the maximum temperature is 86.3˚C. This roughly corresponds to the water content combination #2 in chapter 3, with a ML saturation of 0.5 and a PTL saturation of 0.4. As the saturation at the PTL is increased, in Figure 36, from 0.25 to 0.65, there is a decrease in the maximum temperature in the domain. Similarly as for the CL saturation increase, there is a minimal drop in temperature. For instance, for the Quarter

Channel position, over the range of the water content considered for the PTL, the temperature changes only from 86.3˚C to 85.5˚C.

4.2.5 Effect of Porosity of PTL

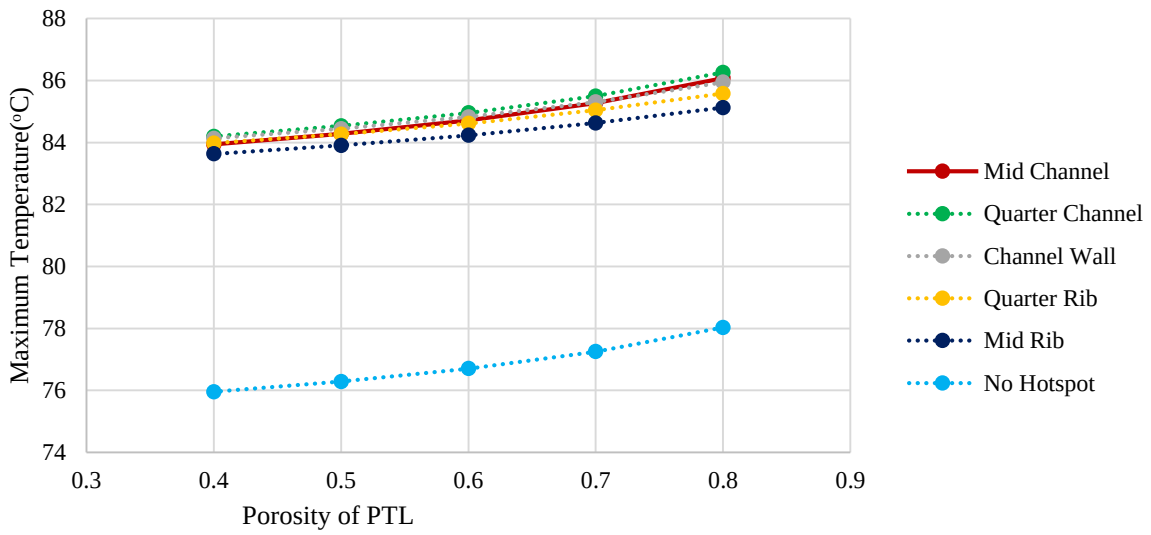

Figure 36: Effect of the Porosity of PTL on the Maximum temperature (˚C) in the presence of two-phase effects

Taking into account the two-phase effect, an increase in the porosity of the PTL, in Figure 37, leads to a rise in the maximum temperature of the domain. For the Quarter Rib, as the PTL porosity in increased from 0.4 to 0.8, the maximum temperature increases from 84.0 ˚C to 85.6˚C. Over the same range and for this location, in chapter 3, the change in the parameter of interest is from 83.6˚C to 85.9˚C. The same

slight change can be observed for all locations. The increase in the volume fraction of the PTL fibres is mostly responsible for the increased heat dissipation, as described previously.

4.2.6 Effect of thickness of the layers in the presence of water

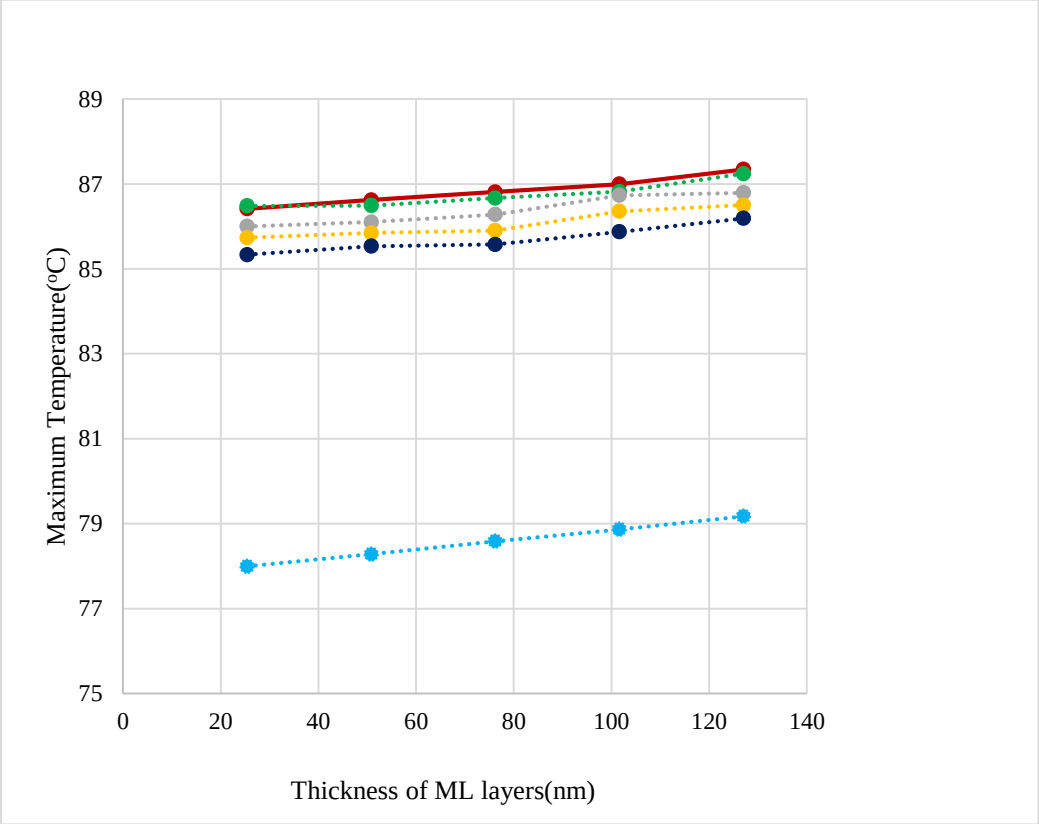

Figure 37: Effect of the increasing ML thickness on the Maximum temperature (˚C) in the presence of two-phase effects

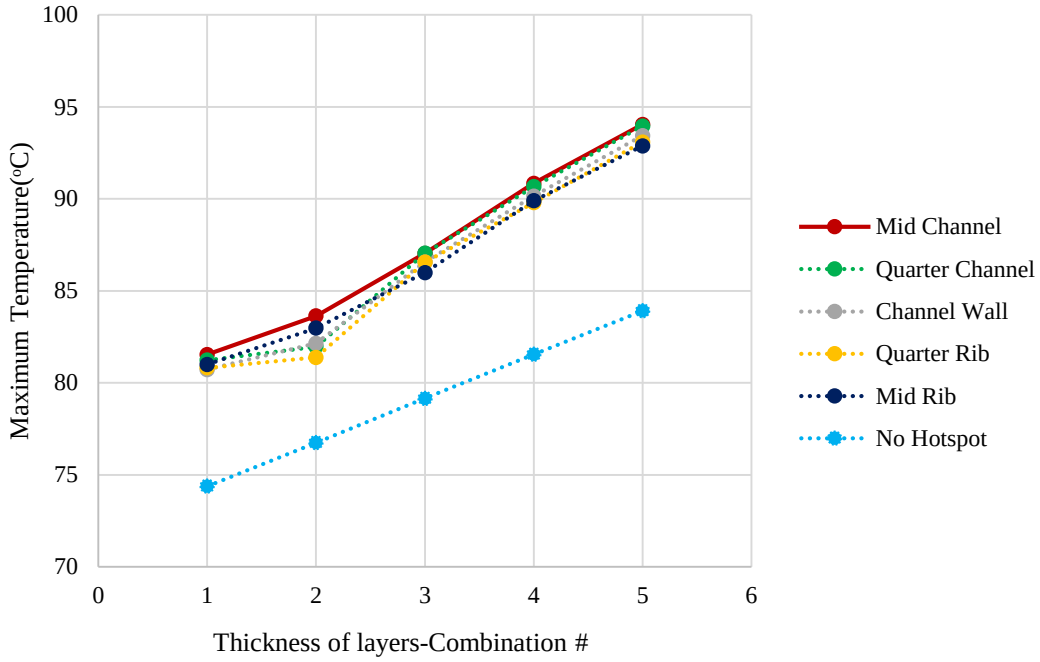

Figure 38: Effect of the increasing thickness of ML-CL layers on the Maximum temperature (˚C) in the presence of two-phase effects

Table 17: Variation of thickness of ML-CL layers

Combination	Thickness(μm)		
	ML	ACL	CCL
#1	25.4	10	10
#2	50.8	15	15
#3	76.2	20	20
#4	101.6	25	25
#5	127	30	30

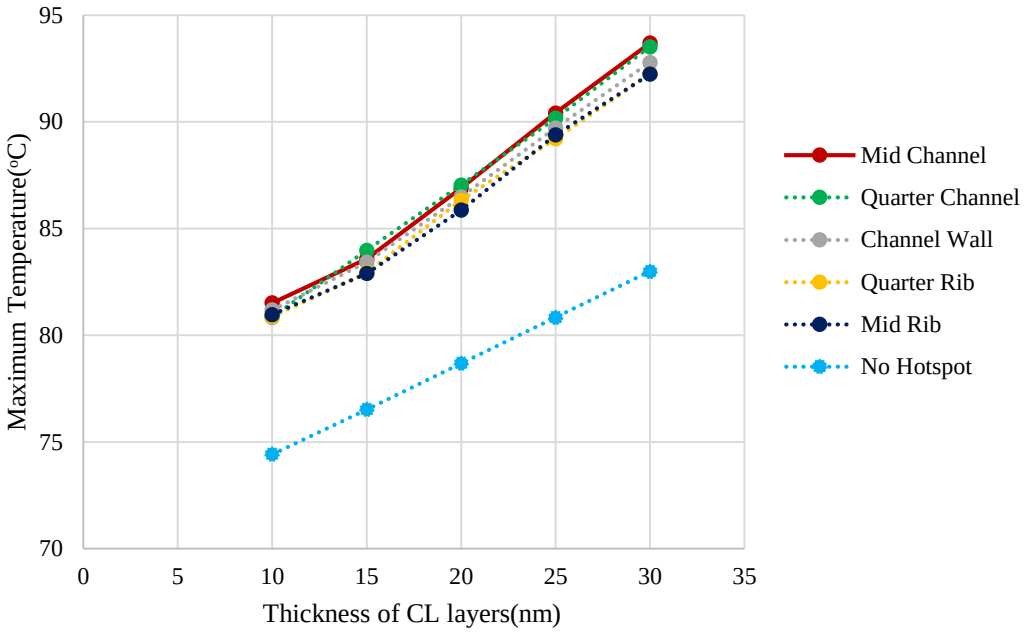

Figure 39: Effect of the increasing CL thickness on the Maximum temperature (˚C) in the presence of two-phase effects

In Figure 38, only the thickness of the Nafion membrane has been varied while the thickness of the other layers have been kept at their base case value. Nafion 111, up to Nafion 115 have been considered. The maximum temperature in the domain is seen to increase as the thickness of the Nafion increases. However, the increase is quite insignificant with an average 0.85 % change in the parameter of interest for all layers. As the thickness of both the membrane and the catalyst layer are increased simultaneously as per the combination values in Table 17, a definitive impact on the maximum temperature can be observed in Figure 39. This can be attributed to the fact that the increase in the thickness of the catalyst layer has a more significant effect, as seen in Figure 40. Indeed, an average rise of 15.33% in the maximum

temperature for all locations was observed when both the thickness of CL and ML are increased while an average increase of 14.58% is observed when only the CL thickness is varied. This increase in the maximum temperature can be explained by an increase in the surface area for the exothermic reaction which takes in the pinhole. As the CL thickness is increased, the pinhole through the CL is also lengthened in this simulation, providing a larger area for the reaction to occur.

4.2.7 Effective thermal conductivity of Porous matrix

For the base case scenario and parametric studies throughout chapter 3 and chapter 4, a classic volume averaged approach has been considered to determine the effective thermal conductivity of each layer in order by accounting for both the fluid properties and the solid matrix. The volume average method can also be referred to as the parallel resistance, in which, the effective thermal conductivity is calculated as the weighted arithmetic mean of the fluid and solid porous matrix respective thermal conductivities. Hence, it is a volume averaging of the parallel network in which the solid matrix is considered distinct from the fluid matrix. Heat can only be transferred at any given time through either the solid or the fluid matrix and not along a path in which the solid and fluid are both coexisting, as it is in reality[15].

$$k_{eff,Volume\ Average} = \varepsilon_f k_f + \left(1-\varepsilon_f\right) k_s \tag{3.27}$$

The equation can be further modified to consider a series resistance network as well as a combination of series and parallel network. The series network is a reciprocal average where the effective conductivity of the solid fluid system is determined as the weighted arithmetic mean of the solid and fluid matrix thermal conductivities.

$$\frac{1}{k_{eff\,,\,Reciprocal\ Average}} = \frac{\varepsilon_f}{k_f} + \frac{\left(1-\varepsilon_f\right)}{k_s} \tag{3.28}$$

The weighted geometric mean of the solid and fluid matrix thermal conductivities is considered for the power law method:

$$k_{eff\,,\,Power\ law} = k_f{}^{\varepsilon_f} \times k_s{}^{\left(1-\varepsilon_f\right)} \tag{3.29}$$

Awad *et al.*[89] provide furthers correlations for estimating the effective thermal conductivity. To see how the results are affected by the method used to compute the effective thermal conductivity, the first parametric study (Effect of the thermal conductivity of the catalyst layer) has been simulated by considering the volume-average, reciprocal average and power law methods for the Channel Wall hotspot, located at the wall of the rib/channel.

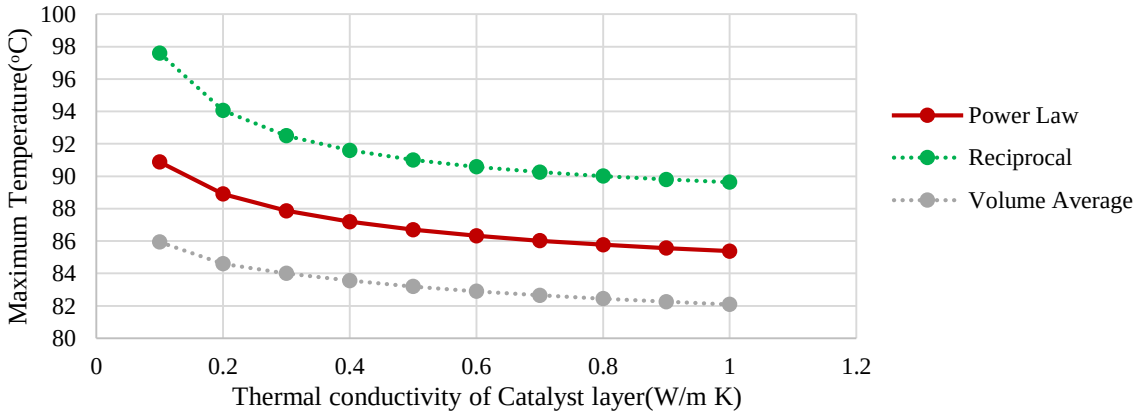

Figure 40: Effect of the effective thermal conductivity determination technique on the Maximum temperature (˚C) for the Channel Wall hotspot

In the Figure 41, the maximum temperature is highest when for the effective thermal conductivity calculated by the reciprocal average method (series network) while the lowest maximum temperature was obtained by the volume average approximation (parallel network). The results for the power law approach lies in between that of the reciprocal average and volume average. Indeed, for a CL thermal conductivity value of 0.1 W/m K, the difference in the maximum temperature between the reciprocal average method and the volume average method is 12°C. The effective thermal conductivity through volume averaging bear a higher value than that by reciprocal average. Hence, the volume average method (parallel network) provides an overestimation of the effective thermal conductivity and therefore, an underestimation of the maximum temperature reached in the domain.

4.2.8 Effect of hydrophobicity of porous layers

The hydrophobicity, characterised by the contact angle, is known to be a function of the liquid water temperature for different metal substrates as well as glass[90]. Indeed, as the temperature rises, there is a reduction in the surface tension force. The contact angle also decreases as the droplet volume increases[90]. Lim and Yang[91], demonstrated the dependence of the contact angle on the temperature in the gas diffusion layers. For a 40 wt. % FEP (fluorinated ethylene propylene) treated PTL, at a water temperature of 80°C, the contact angle was found to be 80^{o} while at a temperature of 20°C, the contact angle was nearly 110^{o}. As the temperature increases, the contact angle and hence the degree of hydrophobicity decreases. The static and dynamic contact angle (advancing and receding) were measured

as a function of temperature for different PTL materials[92]. Except for the Sigracet® PTL sample, it was found that the receding contact angle decreases as the temperature is increased.

The following correlation between the contact angle and temperature was proposed, for a PTL (E-TEK1 ELAT HT 1400-W)[93]:

$$\theta = -0.9444\left(\frac{T}{T_O}\right) + 3.422 \tag{3.30}$$

Where, T_0 =298 K and the contact angle is expressed in radians.

Another study has shown that the hydrophobicity of the PTL can indeed be engineered to increase from 134.7 to 150.9^o by depositing a super hydrophobic layer (Polydimethylsiloxane) on the substrate[10]. Despite the fact that the dependence of the contact angle on the temperature has been demonstrated experimentally, no previous modelling work as reviewed in the literature for this study has considered this relationship in their constituent equations for the two-phase flow physics. This could be due to a lack of general equation which can describe this relationship for the porous layers. For this reason, this effect has also not been studied in this work.

4.3 Key Figure: Relative changes due to variation in the parameters

To summarize the various parametric studies, a bar chart has been plotted to illustrate the relative average change in the maximum temperature in the domain based on the range of literature or commercial values available. The relative percentage change in the parameter of interest, i.e. the maximum temperature in

the domain, due to an increase in the magnitude of the variable under study from its minimum to maximum value has been considered so that the average contribution of each variable under study can be compared. Only the parameters which can be engineered have been included in the comparative bar chart.

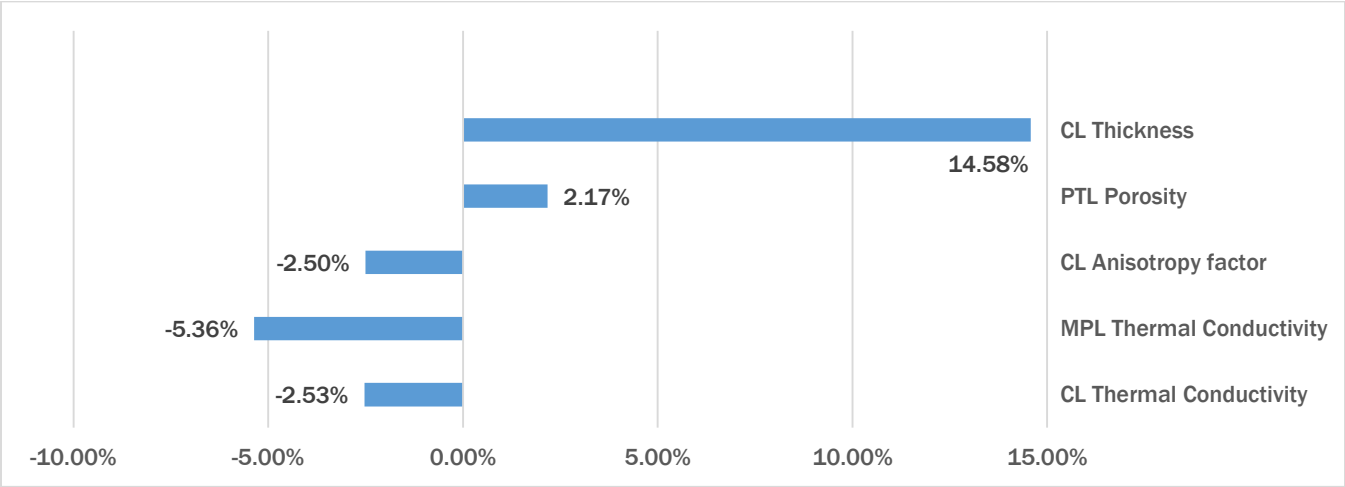

Figure 41: Relative change in the maximum temperature in the domain due to a parameter increase from minimum to maximum value

Table 18: Range of values considered for relative change in maximum temperature

Parameter	Minimum Value	Minimum Value
PTL Porosity	80%	40%
Thickness of CL	30 um	10 um
MPL Thermal Conductivity	0.05 W/m K	0.15 W/m K
CL Anisotropy factor	1	5
CL Thermal Conductivity	0.1	0.5

The relative percentage change in the temperature is computed as: (Maximum temperature at final parameter value-Maximum temperature at initial parameter value)/ Maximum temperature at initial parameter value *100.An average over all pinholes/hotspots locations is then done. The relative change does not include data for the case study with no hotspot/no pinhole. From the Figure 4142, it can be noted that the relative impact of the parameters is quite insignificant except for the thickness of the CL layers. As mentioned previously, rather than the CL thickness itself, the increase in the surface reaction area due an increasing thickness might be the main contributor to the highly elevated temperature in the domain. The thickness of the CL and ML and the PTL porosity must be minimized while the CL anisotropy factor and MPL and CL thermal conductivity must be maximised to optimize heat dissipation.

4.4 Conclusion

Coupling Darcy's law with the heat transport model has enabled the study of the two-phase effects on the thermal gradients resulting from hotspots in the membrane-electrode assembly. The relationship between the main parameter in this study, that is the temperature, and the physical properties such as the viscosity, density and surface tension have been accounted for in this chapter. Hence, differences in the results can be observed compared to the previous chapter in which an appropriate model for the two-phase effects is not considered. An increase in both the CL thermal conductivity and the CL Anisotropy factor leads to a steadier drop in the maximum temperature. At a base case value of 0.1 W/ m K, the maximum temperature decreases uniformly by nearly 1°C for all locations. In the presence of a two- phase Darcy flow, the MPL thermal conductivity has a greater influence on the parameter of interest. The same trends as in chapter 3 could be observed for the PTL porosity and CL thickness but in the refined model, the impact of the PTL

porosity was slightly increased while that of the CL thickness was somewhat reduced. The method used to determine the effective thermal conductivity that is volume average, power law and reciprocal had a significant impact on the determination on the maximum temperature in the domain. The volume average technique provided an underestimation of the maximum temperature while the reciprocal technique overestimated the parameter of interest.

Chapter 5 Conclusion

5.1 Summary of all findings

A two-phase thermal model was developed for a section of a PEFC membrane electrode assembly with half a channel and half a rib. The main contribution of this work is to study the influence of thermal properties on heat dissipation of hotspots in the catalyst layer of the PEFC. In chapter 3, a preliminary thermal model was developed by considering the conservation of energy equation with heat sources and heat sinks. The thermal profile across the MEA layers from the anode to the cathode was mapped for five potential hotspot locations and compared to the same MEA section with no hotspot. The hotspot locations under study are: at the midplane of the channel, midway between the channel midplane and the channel wall, at the channel or rib wall, midway between the rib midplane and the channel wall, at the midplane of the rib. The maximum temperature, which occurs in the CCL, is the parameter of interest in this study. In chapter 4, the thermal model was coupled with Darcy's Law to account for the two-phase flow effects. To accomplish the objectives described in this thesis, parametric studies were done on various parameters, namely, the CL thermal conductivity, the MPL thermal conductivity, the anisotropy factor of the CL thermal conductivity, the PTL porosity, the liquid water distribution and the thickness of the membrane and porous layers.

The thermal properties of the catalyst layer were shown to have a limited effect on the maximum temperature in the catalyst layer at the beginning of life, when no hotspot is present. As the cell ages, a high thermal conductivity and anisotropy may be able to alleviate the impact of localized hot spots that can develop due to membrane thinning and start-stop stresses on the MEA. These observations are in agreement with those of Lu et al. [58] who have observed that the presence of pinholes in the initial stages

of operation of the fuel cell does not immediately affect its performance, resulting in this issue being overlooked until the damage become irreversible. Membrane defects such as pinholes and micro-cracks can be mitigated in the presence of liquid water which seals the defects and eliminates the crossover issue[94].This could be the reason behind a good electrochemical performance despite the presence of small membrane defects. However, this sealing capacity depends on the size of the pinhole and the pressure differential between the anode and the cathode[94]. Accounting for the two-phase flow effects with Darcy's law resulted in an improved heat dissipation, with a reduction of the maximum temperature in the domain for all locations.

We can see in this study that thermal properties are not critical in fuel cells at the beginning of life but plays a more important role as the fuel cell ages and helps to mitigate the thermal runaway once degradation has started to take place. For new catalyst layers incorporating novel materials, it should be ensured that the thermal properties of the CL lie within a certain range that throughout the lifetime of the fuel cell, it would then be possible to dissipate the heat generated by hotspots.

5.2 Recommendations for future work

This section outlines the future studies that can be undertaken to improve our understanding of the importance of heat dissipation on the reliability and durability of the PEFC. Several avenues to improve the results of the current research work and to achieve a more comprehensive model are presented.

5.2.1 Experimental studies

To relate the effect of the thermal distribution on the degradation rate, an experimental study should be pursued. Pinholes could be introduced artificially by perforating the membrane through electron beam lithography, focused ion beam or glassy micro-needles[94] . The standard for durability testing is the accelerated stress test which is used in most works to assess the degradation rate[95]. The thermal profile of a cell could be analyzed using an infrared camera. A printed circuit board sensor plate could also be inserted in the middle of a stack[73] .An empirical equation describing the relationship between the temperature and the degradation rate can then be implemented in the model so that the indirect effect of the thermal properties on the durability of the PEFC can be studied. Additionally, to address the lack of in-plane thermal conductivity values for the catalyst layer in the current model, experimental tests could be performed using appropriate techniques such as the transient plane source, modified transient plane source, thermos-reflectance and infrared laser flash. An anisotropy factor for the thermal conductivity of the catalyst layer can then be determined from the ratio between the through-plane and in-plane values. Factors which can potentially have an influence on the thermal conductivity values could also be assessed. Further studies can be done to unravel potential relationship between the thermal conductivity and other physical properties. For electron conductors such as metals, the thermal conductivity is directly proportional to the electrical conductivity and the temperature through a proportionality constant (Lorentz number) [1]. There could be a potential similar relationship for the CL.

5.2.2 Pore network modelling

The current volume averaged approach used in this model presents some limitations even though complex transport phenomena can be simulated by considering effective properties for the two-phase and thermal transport. Indeed, the liquid water produced at the CL tends to follow a certain preferential geometric

pathway with a tree-like or fingering flow pattern towards the PTL. In the volume averaged method, water is assumed to be distributed uniformly throughout all the porous layers. Hence, the continuum model with a volume averaged approach fails to capture the capillary driven phenomena as well as the spatial heterogeneities in the CL, MPL and PTL morphologies. On the other hand, in a pore network model, the porous layer is represented as a set of interconnected pores and throats, which is comparable to a resistor network[96]. The inhomogeneous nature of the material is mapped through a distribution of the material properties[97].

However, complex coupling of the electrochemical phenomena, thermal and water transport for a complete MEA of a PEFC cell, is computationally expensive in pore network modelling due to the use of partial differential equations as a result of the discretization of the governing equations. Indeed, by modifying the PTL thermal conductivity, Qin *et al.*[98], found through pore network-modelling that they can control the water vapor condensation across the interface between the flow-field ribs and the PTL. However, instead of considering heat transfer physics and phase change for the pore network, a linear thermal gradient has been assumed in the through-plane direction of the PTL to reduce computational requirement. As a result, compared to the continuum volume averaged model, multi-physics phenomena are not yet well represented in pore network modelling works.

To take advantage of the benefits of both approaches and address their limitations, a coupled continuum and pore network model can be implemented such as in the work by Medici *et al.*[97], where an iterative continuum-pore network model is developed. In the work by Aghighi *et al.*[96], pore-scale physics is applied for the PTL while the CL is treated as a porous continuum. Compared to a volume averaged approach, this enabled the authors to show the effect of water percolation on the electrochemical

performance, notably that liquid water block reactive sites on the CL and hence lead to an increase in ohmic losses and hence decrease in performance. However, thermal transport was also not considered in that work.

5.2.3 Hygro-thermal stresses

The effect of the thickness of the MEA layers on the thermal distribution was investigated in this work. However, in the presence of liquid water, the temperature can also influence the mechanical behavior of the constitutive PEFC layers. Hygro-thermal stresses due to heat and moisture leading to expansion and contraction of the layers have not been accounted for in this work. Al-Baghdadi *et al.*[99], takes this effect into consideration by applying Hooke's law and Von Misses stresses. The presence of a physical pinhole across the membrane aggravates mechanical stresses and thus can increase the degradation rate. Hence, hygro-thermal stresses should be taken into consideration in a future model in which durability is studied as a function of the temperature in an operating hydrated PEFC.

5.2.4 Optimization

An optimization model with the parameters considered in the sensitivity study could be developed. An ideal set of physical properties to ensure favorable heat dissipation could then be recommended. For instance, to characterise water management, Wang *et al.*[100], proposed a dimensionless parameter $Da_{o,}$ which is the ratio of the rate of water addition to rate of water removal via diffusion and evaporation, to study two-phase transport in the cathode PTL. Thermal parameters are also lumped into this dimensional number, among which are the operating temperature and the PTL thermal conductivity. By controlling

those thermal parameters to modify the dimensionless parameter, a liquid free region can be created in the PTL which counteracts degradation due to either flooding or dryness[100].

5.2.5 Other considerations

At moderate current density, the maximum current density underneath the gas channel is twice the minimum current density below the lands and this increase to tenfold as air is replaced by oxygen[101]. The thermal profile is impacted by this non-uniformity in the current distribution because the overpotentials and ohmic heat source are dependent on the current density. The clamping pressure is also a critical parameter to consider since it influences the PTL thickness and its thermal conductivity[2]. The difference in pressure from under the land to under the channel have an effect on the PTL thermal conductivity. The non-uniform current distribution and non-uniform thermal conductivity under the land and channel could be accounted for by applying a sinusoid function.

The state of water on the anode side and the dependence of the thermal conductivity of liquid water on the temperature should be considered in a future model. An average porosity is assumed in each porous layer in the current work. However there are transition regions with a jump in porosity between the CL and MPL as well as between the MPL and PTL[102]. These interfacial regions may affect the liquid water saturation profile. For the base case scenario, an averaging approach is used for the physical properties of the two-phase mixture. Instead, various empirical correlation for the determination of properties such as the specific heat capacity, ratio of specific heats, density and thermal conductivity could be explored

References

[1] Mench MM. Fuel Cell Engines. New Jersey: 2008.

[2] Spiegel C. Mathematical modeling of polymer exchange membrane fuel cells by. 2008.

[3] Schmittinger W, Vahidi A. A review of the main parameters influencing long-term performance and durability of PEM fuel cells. J Power Sources 2008;180:1–14. doi:10.1016/j.jpowsour.2008.01.070.

[4] Bauer F, Denneler S, Willert-Porada M. Influence of temperature and humidity on the mechanical properties of Nafion?? 117 polymer electrolyte membrane. J Polym Sci Part B Polym Phys 2005;43:786–95. doi:10.1002/polb.20367.

[5] Ryan O'Hayre, Suk-Won Cha, Whitney Colella FBP. Fuel Cell Fundamentals. 2nd ed. New Jersey: John Wiley & Sons Inc; 2008.

[6] Mathias M, Gasteiger H, Makharia R, Kocha S, Fuller T, Xie T, et al. Can available membranes and catalysts meet automotive polymer electrolyte fuel cell requirements? ACS Div Fuel Chem Prepr 2004;49:471–4.

[7] Alaefour I. Current and Temperature Distributions in Proton Exchange Membrane Fuel Cell by 2012.

[8] Raileanu Ilie VA, Martemianov S, Thomas A. Investigation of the local temperature and overheat inside the membrane electrode assembly of PEM fuel cell. Int J Hydrogen Energy 2016:4–13. doi:10.1016/j.ijhydene.2016.04.103.

[9] US Department of Energy. Fuel Cell Technical Team Roadmap, June 2013. 2013.

[10] Wang C, Wang S, Peng L, Zhang J, Shao Z, Huang J, et al. Recent Progress on the Key Materials and Components for Proton Exchange Membrane Fuel Cells in Vehicle Applications. Energies 2016;9:603. doi:10.3390/en9080603.

[11] US Drive. Fuel Cell Technical Team Roadmap. 2013.

[12] Banerjee R, Kandlikar SG. Two-phase flow and thermal transients in proton exchange membrane fuel cells – A critical review. Int J Hydrogen Energy 2015;40:3990–4010. doi:10.1016/j.ijhydene.2015.01.126.

[13] Jeon SW, Cha D, Kim HS, Kim Y. Analysis of the electrical efficiency of a proton exchange membrane fuel cell at elevated temperature and relative humidity conditions. Appl Energy 2016;166:165–73. doi:10.1016/j.apenergy.2015.12.123.

[14] Kandlikar SG, Lu Z. Thermal management issues in a PEMFC stack - A brief review of current status. Appl Therm Eng 2009;29:1276–80. doi:10.1016/j.applthermaleng.2008.05.009.

[15] Pharoah JG, Karan K, Sun W. On effective transport coefficients in PEM fuel cell electrodes: Anisotropy of the porous transport layers. J Power Sources 2006;161:214–24. doi:10.1016/j.jpowsour.2006.03.093.

[16] Tritt TM. Thermal Conductivity: Theory, Properties and Applications. New York, New York: Kluwer Academic/Plenum; 2004. doi:10.1007/978-1-4899-3751-3.

[17] Dames C. Chapter 2 Measuring the Thermal Conductivity of Thin Films : 3 Omega and Related Electrothermal Methods. Annu Rev Heat Transf 2013:7–49. doi:10.1615/AnnualRevHeatTransfer.v16.20.

[18] Burheim OS, Su H, Hauge HH, Pasupathi S, Pollet BG. Study of thermal conductivity of PEM fuel cell catalyst layers. Int J Hydrogen Energy 2014;39:9397–408. doi:10.1016/j.ijhydene.2014.03.206.

[19] Alhazmi N, Ismail MS, Ingham DB, Hughes KJ, Ma L, Pourkashanian M. The in-plane thermal conductivity and the contact resistance of the components of the membrane electrode assembly in proton exchange membrane fuel cells. J Power Sources 2013;241:136–45. doi:10.1016/j.jpowsour.2013.04.100.

[20] Khandelwal M, Mench MM. Direct measurement of through-plane thermal conductivity and contact resistance in fuel cell materials. J Power Sources 2006;161:1106–15. doi:10.1016/j.jpowsour.2006.06.092.

[21] Vie PJS, Kjelstrup S. Thermal conductivities from temperature profiles in the polymer electrolyte fuel cell. Electrochim Acta 2004;49:1069–77. doi:10.1016/j.electacta.2003.10.018.

[22] D.J. Burford MMM. Proceedings of the IMECE'04 ASME International Mechanical Engineering Congress and Exposition, 2004.

[23] Ramousse J, Didierjean S, Lottin O, Maillet D. Estimation of the effective thermal conductivity of carbon felts used as PEMFC Gas Diffusion Layers. Int J Therm Sci 2008;47:1–6. doi:10.1016/j.ijthermalsci.2007.01.018.

[24] Zamel N, Litovsky E, Li X, Kleiman J. Measurement of the through-plane thermal conductivity of carbon paper diffusion media for the temperature range from -50 to +120 ??c. Int J Hydrogen Energy 2011;36:12618–25. doi:10.1016/j.ijhydene.2011.06.097.

[25] Andisheh-Tadbir M, Kjeang E, Bahrami M. Thermal conductivity of microporous layers: Analytical modeling and experimental validation. J Power Sources 2015;296:344–51. doi:10.1016/j.jpowsour.2015.07.054.

[26] Burheim OS, Vie PJS, Pharoah JG, Kjelstrup S. Ex situ measurements of through-plane thermal conductivities in a polymer electrolyte fuel cell. J Power Sources 2010;195:249–56. doi:10.1016/j.jpowsour.2009.06.077.

[27] Burheim OS, Su H, Pasupathi S, Pharoah JG, Pollet BG. Thermal conductivity and temperature

profiles of the micro porous layers used for the polymer electrolyte membrane fuel cell. Int J Hydrogen Energy 2013;38:8437–47. doi:10.1016/j.ijhydene.2013.04.140.

[28] Burheim OS, Kjelstrup S, Pharoah JG, Vie PJS, Møller-Holst S. Calculation of reversible electrode heats in the proton exchange membrane fuel cell from calorimetric measurements. Electrochim Acta 2011;56:3248–57. doi:10.1016/j.electacta.2011.01.034.

[29] Karimi G, Li X, Teertstra P. Measurement of through-plane effective thermal conductivity and contact resistance in PEM fuel cell diffusion media. Electrochim Acta 2010;55:1619–25. doi:10.1016/j.electacta.2009.10.035.

[30] Sadeghi E, Djilali N, Bahrami M. Effective thermal conductivity and thermal contact resistance of gas diffusion layers in proton exchange membrane fuel cells. Part 1: Effect of compressive load. J Power Sources 2011;196:246–54. doi:10.1016/j.jpowsour.2010.06.039.

[31] Sadeghi E, Djilali N, Bahrami M. Effective thermal conductivity and thermal contact resistance of gas diffusion layers in proton exchange membrane fuel cells. Part 2: Hysteresis effect under cyclic compressive load. J Power Sources 2010;195:8104–9. doi:10.1016/j.jpowsour.2010.07.051.

[32] Nitta I, Himanen O, Mikkola M. Thermal conductivity and contact resistance of compressed gas diffusion layer of PEM fuel cell. Fuel Cells 2008;8:111–9. doi:10.1002/fuce.200700054.

[33] A. Radhakrishnan, Z. Lu and SGK. Effective Thermal Conductivity of Gas Diffusion Layers Used in PEMFC: Measured with Guarded-Hot-Plate Method and Predicted by a Fractal method. ECS Trans 2010;23:168–83. doi:10.1111/j.1467-9329.2010.00459.x.

[34] Bhaiya M, Putz A, Secanell Gallart M. Electrochimica Acta Analysis of non-isothermal effects on polymer electrolyte fuel cell electrode assemblies. Electrochim Acta 2014;147:294–309. doi:10.1016/j.electacta.2014.09.051.

[35] Motoaki Kawase, Sze Ting Chin, Miho Kaeyama KM. Effective Thermal Conductivity of Catalyst layer of PEFC. 220th ECS Meet., 2011.

[36] Hu J, Li J, Xu L, Huang F, Ouyang M. Analytical calculation and evaluation of water transport through a proton exchange membrane fuel cell based on a one-dimensional model. Energy 2016;111:869–83. doi:10.1016/j.energy.2016.06.020.

[37] Sadeghi E, Djilali N, Bahrami M. A novel approach to determine the in-plane thermal conductivity of gas diffusion layers in proton exchange membrane fuel cells. J Power Sources 2011;196:3565–71. doi:10.1016/j.jpowsour.2010.11.151.

[38] Zamel N, Litovsky E, Shakhshir S, Li X, Kleiman J. Measurement of in-plane thermal conductivity of carbon paper diffusion media in the temperature range of -20??C to +120??C. Appl Energy 2011;88:3042–50. doi:10.1016/j.apenergy.2011.02.037.

[39] Teertstra P, Karimi G, Li X. Measurement of in-plane effective thermal conductivity in PEM fuel cell diffusion media. Electrochim Acta 2011;56:1670–5. doi:10.1016/j.electacta.2010.06.043.

[40] Pharoah JG, Burheim OS. On the temperature distribution in polymer electrolyte fuel cells. J Power Sources 2010;195:5235–45. doi:10.1016/j.jpowsour.2010.03.024.

[41] Burheim OS, Crymble G a., Bock R, Hussain N, Pasupathi S, du Plessis A, et al. Thermal conductivity in the three layered regions of micro porous layer coated porous transport layers for the PEM fuel cell. Int J Hydrogen Energy 2015:1–11. doi:10.1016/j.ijhydene.2015.07.169.

[42] Maggio G, Recupero V, Mantegazza C. Modelling of temperature distribution in a solid polymer electrolyte fuel cell stack 1996;62:167–74.

[43] Shan Y, Choe SY, Choi SH. Unsteady 2D PEM fuel cell modeling for a stack emphasizing thermal effects. J Power Sources 2007;165:196–209. doi:10.1016/j.jpowsour.2006.12.022.

[44] Park SK, Choe SY. Dynamic modeling and analysis of a 20-cell PEM fuel cell stack considering temperature and two-phase effects. J Power Sources 2008;179:660–72. doi:10.1016/j.jpowsour.2008.01.029.

[45] Ju H, Meng H, Wang CY. A single-phase, non-isothermal model for PEM fuel cells. Int J Heat Mass Transf 2005;48:1303–15. doi:10.1016/j.ijheatmasstransfer.2004.10.004.

[46] Berning T, Lu DM, Djilali N. Three-dimensional computational analysis of transport phenomena in a PEM fuel cell. J Power Sources 2002;106:284–94. doi:10.1016/S0378-7753(01)01057-6.

[47] Hwang JJ. Thermal-Electrochemical Modeling of a Proton Exchange Membrane Fuel Cell. J Electrochem Soc 2006;153:A216. doi:10.1149/1.2137652.

[48] Rowe A, Li X. Mathematical modeling of proton exchange membrane fuel cells. J Power Sources 2001;102:82–96. doi:10.1016/S0378-7753(01)00798-4.

[49] Bapat CJ. Anisotropic Heat Conduction Effects in Proton Exchange Membrane Fuel Cells. 2008.

[50] Burheim OS. Thermal Signature and Thermal Conductivities of PEM Fuel Cells. 2009.

[51] Reucroft PJ, Rivin D, Schneider NS. Thermodynamics of Nafion???-vapor interactions. I. Water vapor. Polymer (Guildf) 2002;43:5157–61. doi:10.1016/S0032-3861(02)00342-7.

[52] Lu W, Liu Z, Wang C, Mao Z, Zhang M. The effects of pinholes on proton exchange membrane fuel cell performance 2011:24–30. doi:10.1002/er.

[53] Bhaiya M. An open-source two-phase non-isothermal mathematical model of a polymer electrolyte membrane fuel cell by Madhur Bhaiya A thesis submitted to the Faculty of Graduate Studies and Research in partial fulfillment of the requirements for the degree of Master. 2014.

[54] Weber AZ, Newman J. Modeling Transport in Polymer-Electrolyte Fuel Cells: Chemical Reviews. vol. 104. 2004. doi:10.1021/cr020729l.

[55] Perry RH, Green DW, Maloney JO. Perry's Chemical Engineers' Handbook Seventh. vol. 27. 1997. doi:10.1021/ed027p533.1.

[56] Tsilingiris PT. Thermophysical and transport properties of humid air at temperature range between 0 and 100 C. Energy Convers Manag 2008;49:1098–110. doi:10.1016/j.enconman.2007.09.015.

[57] Sengers, J.V., Watson, J.T.R., Basu, R.S., Kamgar-Parsi, B., Hendricks RC. Representative equations for thermal conductivity of water substances. J Phys ChemRefData 1984.

[58] Yao KZ, Karan K, McAuley KB, Oosthuizen P, Peppley B, Xie T. A Review of Mathematical Models for Hydrogen and Direct Methanol Polymer Electrolyte Membrane Fuel Cells. Fuel Cells 2004;4:3–29. doi:10.1002/fuce.200300004.

[59] Olaf Schenk, Klaus Gärtner PC. PARDISO 5.0.0 Solver Project 2007.

[60] Ramousse J, Lottin O, Didierjean S, Maillet D. Heat sources in proton exchange membrane (PEM) fuel cells. J Power Sources 2009;192:435–41. doi:10.1016/j.jpowsour.2009.03.038.

[61] Burheim OS, Vie PJS, Møller-Holst S, Pharoah JG, Kjelstrup S. A calorimetric analysis of a polymer electrolyte fuel cell and the production of H2O2 at the cathode. Electrochim Acta 2010;55:935–42. doi:10.1016/j.electacta.2009.09.053.

[62] Springer TE, Zawodzinski T a., Gottesfeld S. Polymer electrolyte fuel cell model. J Electrochem Soc 1991;138:2334–42. doi:10.1149/1.2085971.

[63] Aqualab. WATER ACTIVITY DEFINITION (AN-13418-00) 1981.

[64] Motupally S, Becker AJ, Weidner JW. Diffusion of Water in Nafion 115 Membranes. J Electrochem Soc 2000;147:3171. doi:10.1149/1.1393879.

[65] Songprakorp R. Investigation of Transient Phenomena of Proton Exchange Membrane Fuel Cells Investigation of Transient Phenomena of Proton Exchange Membrane Fuel Cells 2008:183.

[66] Stanic V, Hoberecht M. Mechanism of pin-hole formation in membrane electrode assemblies for PEM fuel cells. 2006.

[67] Popiel CO, Wojtkowiak J. Simple Formulas for Thermophysical Properties of Liquid Water for Heat Transfer Calculations (from 0°C to 150°C). Heat Transf Eng 1998;19:87–101. doi:10.1080/01457639808939929.

[68] Secanell Gallart M. Computational Modeling and Optimization of Proton Exchange Membrane Fuel Cells. PhD Dissertation. University of Victoria, 2007.

[69] Oberbroeckling K, Dunwoody DC, Leddy J. Density of Cation Exchanged Nafion 1978:95.

[70] Ramousse J, Deseure J, Lottin O, Didierjean S, Maillet D. Modelling of heat, mass and charge transfer in a PEMFC single cell. J Power Sources 2005;145:416–27. doi:10.1016/j.jpowsour.2005.01.067.

[71] Comsol. Heat Transfer Module: User's Guide 2011:268.

[72] Nishimura A, Fukuoka T, Baba M, Hirota M, Hu E. Clarification on Temperature Distribution in Single Cell of Polymer Electrolyte Fuel Cell under Different Operation Conditions by Means of 1D Multi-Plate Heat-Transfer Model. J Chem Eng Japan 2015;48:862–71. doi:10.1252/jcej.14we200.

[73] Nandjou F, Poirot-crouvezier J, Chandesris M, Bultel Y. ScienceDirect A pseudo-3D model to investigate heat and water transport in large area PEM fuel cells e Part 1 : Model development and validation. Int J Hydrogen Energy 2016;33:1–17. doi:10.1016/j.ijhydene.2016.06.007.

[74] Weber a. Z, Borup RL, Darling RM, Das PK, Dursch TJ, Gu W, et al. A Critical Review of Modeling Transport Phenomena in Polymer-Electrolyte Fuel Cells. J Electrochem Soc 2014;161:F1254–99. doi:10.1149/2.0751412jes.

[75] Todd D, Walter M. Synthesis of transport layers with controlled anisotropy and application thereof to study proton exchange membrane fuel cell performance 2016;311:182–7. doi:10.1016/j.jpowsour.2016.02.031.

[76] Deevanhxay P, Sasabe T, Tsushima S, Hirai S. Observation of dynamic liquid water transport in the microporous layer and gas diffusion layer of an operating PEM fuel cell by high-resolution soft X-ray radiography. J Power Sources 2013;230:38–43. doi:10.1016/j.jpowsour.2012.11.140.

[77] Nam JH, Lee K-J, Hwang G-S, Kim C-J, Kaviany M. Microporous layer for water morphology control in PEMFC. Int J Heat Mass Transf 2009;52:2779–91. doi:10.1016/j.ijheatmasstransfer.2009.01.002.

[78] Ge N, Chevalier S, Lee J, Antonacci P, George M, Liu H, et al. Non-isothermal two-phase transport in the polymer electrolyte membrane fuel cell microporous layer. Int J Heat Mass Transf 2016.

[79] Buongiorno J. Notes On Two-Phase Flow, Boiling Heat Transfer, And Boiling Crisis In PWRs And BWRs 2010:1–34.

[80] Bazylak. Liquid water visualization in PEM fuel cells: A review. Int J Hydrogen Energy 2009;34:3845–57. doi:10.1016/j.ijhydene.2009.02.084.

[81] Litster S, Sinton D, Djilali N. Ex situ visualization of liquid water transport in PEM fuel cell gas diffusion layers. J Power Sources 2006;154:95–105. doi:10.1016/j.jpowsour.2005.03.199.

[82] Comsol. CFD Module User ' s Guide 2015.

[83] Kumbur EC, Sharp K V., Mench MM. On the effectiveness of Leverett approach for describing the water transport in fuel cell diffusion media. J Power Sources 2007;168:356–68. doi:10.1016/j.jpowsour.2007.02.054.

[84] Wang Y, Wang CY. Simulation of flow and transport phenomena in a polymer electrolyte fuel cell under low-humidity operation. J Power Sources 2005;147:148–61. doi:10.1016/j.jpowsour.2005.01.047.

[85] Formulas for Viscosity. Univ Sydney,Aerospace, Mech Mechatron Engg 2005. http://www-mdp.eng.cam.ac.uk/web/library/enginfo/aerothermal_dvd_only/aero/fprops/propsoffluids/node5.html.

[86] Fox, R. W; McDonald AT. Introduction to Fluid Mechanics. Fifth edit. New York: John Wiley &

Sons Inc; 1998.

[87] Villanueva PAM. A mixed wettability pore size distribution model for the analysis of water transport in PEMFC materials. 2013.

[88] Cao TF, Lin H, Chen L, He YL, Tao WQ. Numerical investigation of the coupled water and thermal management in PEM fuel cell. Appl Energy 2013;112:1115–25. doi:10.1016/j.apenergy.2013.02.031.

[89] Awad MM, Muzychka YS. Effective property models for homogeneous two-phase flows. Exp Therm Fluid Sci 2008;33:106–13. doi:10.1016/j.expthermflusci.2008.07.006.

[90] Majeed MH. Static Contact Angle and Large Water Droplet Thickness Measurements with the Change of Water Temperature 2014;17:114–28.

[91] Lim C, Wang CY. Effects of hydrophobic polymer content in GDL on power performance of a PEM fuel cell. Electrochim Acta 2004;49:4149–56. doi:10.1016/j.electacta.2004.04.009.

[92] A VK. Static and Dynamic Contact Angle Measurement on Rough Surfaces Using Sessile Drop Profile Analysis with Application to Water Management in Low Temperature Fuel Cells 2010.

[93] Coppo M, Siegel NP, Spakovsky MR von. On the influence of temperature on PEM fuel cell operation. J Power Sources 2006;159:560–9. doi:10.1016/j.jpowsour.2005.09.069.

[94] Kreitmeier S, Michiardi M, Wokaun A, Büchi FN. Factors determining the gas crossover through pinholes in polymer electrolyte fuel cell membranes. Electrochim Acta 2012;80:240–7. doi:10.1016/j.electacta.2012.07.013.

[95] Wu J, Yuan XZ, Martin JJ, Wang H, Zhang J, Shen J, et al. A review of PEM fuel cell durability: Degradation mechanisms and mitigation strategies. J Power Sources 2008;184:104–19. doi:10.1016/j.jpowsour.2008.06.006.

[96] Aghighi M, Hoeh MA, Lehnert W, Merle G, Gostick J. Simulation of a Full Fuel Cell Membrane

Electrode Assembly Using Pore Network Modeling. J Electrochem Soc 2016;163:F384–92. doi:10.1149/2.0701605jes.

[97] Medici EF, Zenyuk I V., Parkinson DY, Weber AZ, Allen JS. Understanding Water Transport in Polymer Electrolyte Fuel Cells Using Coupled Continuum and Pore-Network Models. Fuel Cells 2016:1–9. doi:10.1002/fuce.201500213.

[98] Qin C-Z, Hassanizadeh S, Van Oosterhout L. Pore-Network Modeling of Water and Vapor Transport in the Micro Porous Layer and Gas Diffusion Layer of a Polymer Electrolyte Fuel Cell. Computation 2016;4:21. doi:10.3390/computation4020021.

[99] Al-Baghdadi MARS. A CFD model for analysis of performance, water and thermal distribution, and mechanical related failure in PEM fuel cells. J Mechatronics, Electr Power, Veh Technol 2016;7:7. doi:10.14203/j.mev.2016.v7.7-20.

[100] Wang Y, Chen KS. Advanced control of liquid water region in diffusion media of polymer electrolyte fuel cells through a dimensionless number. J Power Sources 2016;315:224–35. doi:10.1016/j.jpowsour.2016.03.045.

[101] Reum M, Wokaun A, Büchi FN. Measuring the Current Distribution with Submillimeter Resolution in PEFCs. J Electrochem Soc 2009;156:B1225. doi:10.1149/1.3187913.

[102] Chevalier S, Lee J, Ge N, Yip R, Antonacci P, Tabuchi Y, et al. In operando measurements of liquid water saturation distributions and effective diffusivities of polymer electrolyte membrane fuel cell gas diffusion layers. Electrochim Acta 2016;210:792–803. doi:10.1016/j.electacta.2016.05.180.

[103] Comsol M. Maxwell Stefan Diffusion in a Fuel cell Unit cell.

{Bibliography

Appendix

The below sections provide an example of the expressions and definitions in COMSOL 5.2 for the heat transfer and two-phase Darcy law physics for the catalyst layer on the cathode side in the domain for the Mid Channel pinhole. The general mass transport physics applied for the porous layers and the channel are described in the last section, Appendix A.4. These data have been directly extracted from the COMSOL files. The other porous layers have been simulated similarly but with the appropriate expressions, equations and variables pertaining to each layer.

A.1 Heat Transfer in Porous Media CCL

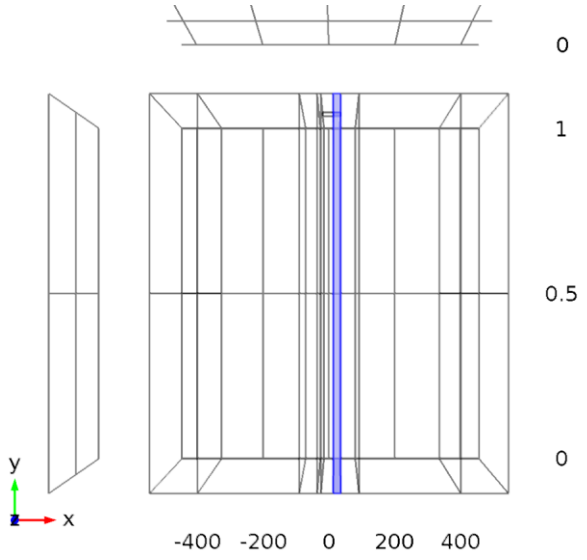

Figure 42: Heat Transfer in Porous Media CCL

A.1.1 Selection

Geometric entity level	Domain
Selection	Domain 8

A.1.2 Equations

$$\rho C_p \mathbf{u} \cdot \nabla T + \nabla \cdot \mathbf{q} = Q + Q_{vd}$$

$$\mathbf{q} = -k_{eff} \nabla T$$

$$k_{eff} = \theta_p k_p + (1 - \theta_p) k + k_{disp}$$

A.1.3 Settings

Description	Value
Fluid type	Gas/Liquid
	Air (mat7)
Thermal conductivity	User defined
Thermal conductivity	{{tpdl.s1*k_h2o + (1 - tpdl.s1)*k_air, 0, 0}, {0, tpdl.s1*k_h2o + (1 - tpdl.s1)*k_air, 0}, {0, 0, tpdl.s1*k_h2o + (1 - tpdl.s1)*k_air}}
Density	User defined
Density	tpdl.s1*comp1.mat9.def.Mn + (1 - tpdl.s1)*comp1.mat7.def.Mn
Heat capacity at constant pressure	User defined
Heat capacity at constant pressure	tpdl.s1*comp1.mat9.def.Cp + (1 - tpdl.s1)*comp1.mat7.def.Cp
Ratio of specific heats	User defined
Ratio of specific heats	tpdl.s1*comp1.mat9.def.gamma + (1 - tpdl.s1)*comp1.mat7.def.gamma
Volume fraction	phi_ccl
Effective conductivity	Volume average
Thermal conductivity	From material

Description	Value
Density	User defined
Specific heat capacity	User defined
Solid material	Cathode (mat3)

A.1.4 Properties from material

Property	Material	Property group
Thermal conductivity	Cathode	Basic

A.1.5 Variables

Name	Expression	Unit	Description	Selection
domflux.Tx	(-ht3.k_effxx*Tx-ht3.k_effxy*Ty-ht3.k_effxz*Tz)*ht3.d	W/m^2	Domain flux, x component	Domain 8
domflux.Ty	(-ht3.k_effyx*Tx-ht3.k_effyy*Ty-ht3.k_effyz*Tz)*ht3.d	W/m^2	Domain flux, y component	Domain 8
domflux.Tz	(-ht3.k_effzx*Tx-ht3.k_effzy*Ty-ht3.k_effzz*Tz)*ht3.d	W/m^2	Domain flux, z component	Domain 8

Name	Expression	Unit	Description	Selection
ht3.WnsInt	ht3.porous5.intDom(ht3.pA*(d(ht3.ux,x)+d(ht3.uy,y)+d(ht3.uz,z))*ht3.porous5.varIntSpa)	W	Total work source	Global
ht3.kxx	tpdl.s1*k_h2o+(1-tpdl.s1)*k_air	W/(m*K)	Thermal conductivity, xx component	Domain 8
ht3.kyx	0	W/(m*K)	Thermal conductivity, yx component	Domain 8
ht3.kzx	0	W/(m*K)	Thermal conductivity, zx component	Domain 8
ht3.kxy	0	W/(m*K)	Thermal conductivity, xy component	Domain 8
ht3.kyy	tpdl.s1*k_h2o+(1-tpdl.s1)*k_air	W/(m*K)	Thermal conductivity, yy component	Domain 8
ht3.kzy	0	W/(m*K)	Thermal conductivity, zy component	Domain 8

Name	Expression	Unit	Description	Selection
ht3.kxz	0	W/(m*K)	Thermal conductivity, xz component	Domain 8
ht3.kyz	0	W/(m*K)	Thermal conductivity, yz component	Domain 8
ht3.kzz	tpdl.s1*k_h2o+(1-tpdl.s1)*k_air	W/(m*K)	Thermal conductivity, zz component	Domain 8
ht3.rho	material.rho	kg/m^3	Density	Domain 8
ht3.Cp	tpdl.s1*mat9.def.Cp+(1-tpdl.s1)*mat7.def.Cp	J/(kg*K)	Heat capacity at constant pressure	Domain 8
ht3.gamma	tpdl.s1*mat9.def.gamma+(1-tpdl.s1)*mat7.def.gamma	1	Ratio of specific heats	Domain 8
ht3.k_pxx	material.k_p11	W/(m*K)	Thermal conductivity, xx component	Domain 8
ht3.k_pyx	material.k_p21	W/(m*K)	Thermal conductivity, yx component	Domain 8

Name	Expression	Unit	Description	Selection
ht3.k_pzx	material.k_p31	W/(m*K)	Thermal conductivity, zx component	Domain 8
ht3.k_pxy	material.k_p12	W/(m*K)	Thermal conductivity, xy component	Domain 8
ht3.k_pyy	material.k_p22	W/(m*K)	Thermal conductivity, yy component	Domain 8
ht3.k_pzy	material.k_p32	W/(m*K)	Thermal conductivity, zy component	Domain 8
ht3.k_pxz	material.k_p13	W/(m*K)	Thermal conductivity, xz component	Domain 8
ht3.k_pyz	material.k_p23	W/(m*K)	Thermal conductivity, yz component	Domain 8
ht3.k_pzz	material.k_p33	W/(m*K)	Thermal conductivity, zz component	Domain 8
ht3.rho_p	0	kg/m^3	Density	Domain 8

Name	Expression	Unit	Description	Selection
ht3.Cp_p	0	J/(kg*K)	Specific heat capacity	Domain 8
ht3.theta_p	phi_ccl	1	Volume fraction	Domain 8
ht3.T	model.input.minput_temperature	K	Temperature	Domain 8
ht3.alphap	-d(ht3.rho,T)/(ht3.rho+eps)	1/K	Isobaric compressibility coefficient	Domain 8
ht3.pA	model.input.minput_pressure	Pa	Absolute pressure	Domain 8
ht3.gradTmag	sqrt(ht3.gradTx^2+ht3.gradTy^2+ht3.gradTz^2)	K/m	Temperature gradient magnitude	Domain 8
ht3.kmean	(ht3.k_effxx+ht3.k_effyy+ht3.k_effzz)/3	W/(m*K)	Mean effective thermal conductivity	Domain 8
ht3.Q	0	W/m^3	Heat source	Domain 8
ht3.qs	0	W/(m^3*K)	Production/absorption coefficient	Domain 8
ht3.Qmet	0	W/m^3	Metabolic heat source	Domain 8
ht3.Qtot	0	W/m^3	Total heat source	Domain 8

Name	Expression	Unit	Description	Selection
ht3.rhoInt	subst(ht3.rho,root.comp1.ht3.porous5.minput_pressure,ht3.pA)	kg/m^3	Density for integration	Domain 8
ht3.CpInt	subst(ht3.Cp,root.comp1.ht3.porous5.minput_pressure,ht3.pA)	J/(kg*K)	Specific heat capacity for integration	Domain 8
ht3.gammaInt	subst(ht3.gamma,root.comp1.ht3.porous5.minput_pressure,ht3.pA)	1	Ratio of specific heats for integration	Domain 8
ht3.TRef	298.15[K]	K	Reference temperature	Domain 8
ht3.pRef	ht3.porous5.pRef	Pa	Reference pressure level	Domain 8
ht3.HRef	0	J/kg	Reference enthalpy	Domain 8
ht3.DeltaH	integrate((1+T*d(ht3.rhoInt,T)/ht3.rhoInt)/ht3.rhoInt,ht3.pA,ht3.pRef,ht3.pA)+integrate(subst(ht3.CpInt,ht3.pA,ht3.pRef),T,ht3.TRef,T)	J/kg	Sensible enthalpy	Domain 8
ht3.H	ht3.HRef+ht3.DeltaH	J/kg	Enthalpy	Domain 8

Name	Expression	Unit	Description	Selection
ht3.H0	ht3.H+0.5*(ht3.ux^2+ht3.uy^2+ht3.uz^2)	J/kg	Total enthalpy	Domain 8
ht3.Ei	ht3.H-ht3.pA/ht3.rho	J/kg	Internal energy	Domain 8
ht3.Ei0	ht3.Ei+0.5*(ht3.ux^2+ht3.uy^2+ht3.uz^2)	J/kg	Total internal energy	Domain 8
ht3.Qbtot	0	W/m^2	Total boundary heat source	Boundaries 36–39, 41–43, 45–46
ht3.k_effxx	ht3.k_eqxx	W/(m*K)	Effective thermal conductivity, xx component	Domain 8
ht3.k_effyx	ht3.k_eqyx	W/(m*K)	Effective thermal conductivity, yx component	Domain 8
ht3.k_effzx	ht3.k_eqzx	W/(m*K)	Effective thermal conductivity, zx component	Domain 8
ht3.k_effxy	ht3.k_eqxy	W/(m*K)	Effective thermal conductivity, xy component	Domain 8

Name	Expression	Unit	Description	Selection
ht3.k_effyy	ht3.k_eqyy	W/(m*K)	Effective thermal conductivity, yy component	Domain 8
ht3.k_effzy	ht3.k_eqzy	W/(m*K)	Effective thermal conductivity, zy component	Domain 8
ht3.k_effxz	ht3.k_eqxz	W/(m*K)	Effective thermal conductivity, xz component	Domain 8
ht3.k_effyz	ht3.k_eqyz	W/(m*K)	Effective thermal conductivity, yz component	Domain 8
ht3.k_effzz	ht3.k_eqzz	W/(m*K)	Effective thermal conductivity, zz component	Domain 8
ht3.C_eff	ht3.C_eq	J/(m^3*K)	Effective volumetric heat capacity	Domain 8
ht3.ux	ht3.u_inputx	m/s	Velocity field, x component	Domain 8
ht3.uy	ht3.u_inputy	m/s	Velocity field, y component	Domain 8

Name	Expression	Unit	Description	Selection
ht3.uz	ht3.u_inputz	m/s	Velocity field, z component	Domain 8
ht3.gradTx	Tx	K/m	Temperature gradient, x component	Domain 8
ht3.gradTy	Ty	K/m	Temperature gradient, y component	Domain 8
ht3.gradTz	Tz	K/m	Temperature gradient, z component	Domain 8
ht3.Qltot	0	W/m	Total line heat source	Edges 56–65, 67–72, 74, 76–78, 81
ht3.Qptot	0	W	Total point heat source	Points 28–41
ht3.alphaTdxx	ht3.k_effxx/ht3.C_eff	m^2/s	Thermal diffusivity, xx component	Domain 8
ht3.alphaTdyx	ht3.k_effyx/ht3.C_eff	m^2/s	Thermal diffusivity, yx component	Domain 8

Name	Expression	Unit	Description	Selection
ht3.alphaTdzx	ht3.k_effzx/ht3.C_eff	m^2/s	Thermal diffusivity, zx component	Domain 8
ht3.alphaTdxy	ht3.k_effxy/ht3.C_eff	m^2/s	Thermal diffusivity, xy component	Domain 8
ht3.alphaTdyy	ht3.k_effyy/ht3.C_eff	m^2/s	Thermal diffusivity, yy component	Domain 8
ht3.alphaTdzy	ht3.k_effzy/ht3.C_eff	m^2/s	Thermal diffusivity, zy component	Domain 8
ht3.alphaTdxz	ht3.k_effxz/ht3.C_eff	m^2/s	Thermal diffusivity, xz component	Domain 8
ht3.alphaTdyz	ht3.k_effyz/ht3.C_eff	m^2/s	Thermal diffusivity, yz component	Domain 8
ht3.alphaTdzz	ht3.k_effzz/ht3.C_eff	m^2/s	Thermal diffusivity, zz component	Domain 8
ht3.alphaTdMean	ht3.kmean/ht3.C_eff	m^2/s	Mean thermal diffusivity	Domain 8
ht3.dfluxx	-ht3.k_effxx*Tx-ht3.k_effxy*Ty-ht3.k_effxz*Tz	W/m^2	Conductive heat flux, x component	Domain 8

Name	Expression	Unit	Description	Selection
ht3.dfluxy	-ht3.k_effyx*Tx-ht3.k_effyy*Ty-ht3.k_effyz*Tz	W/m^2	Conductive heat flux, y component	Domain 8
ht3.dfluxz	-ht3.k_effzx*Tx-ht3.k_effzy*Ty-ht3.k_effzz*Tz	W/m^2	Conductive heat flux, z component	Domain 8
ht3.dfluxMag	sqrt(ht3.dfluxx^2+ht3.dfluxy^2+ht3.dfluxz^2)	W/m^2	Conductive heat flux magnitude	Domain 8
ht3.trlfluxx	0	W/m^2	Translational heat flux, x component	Domain 8
ht3.trlfluxy	0	W/m^2	Translational heat flux, y component	Domain 8
ht3.trlfluxz	0	W/m^2	Translational heat flux, z component	Domain 8
ht3.trlfluxMag	sqrt(ht3.trlfluxx^2+ht3.trlfluxy^2+ht3.trlfluxz^2)	W/m^2	Translational heat flux magnitude	Domain 8
ht3.cfluxx	ht3.rho*ht3.ux*ht3.Ei	W/m^2	Convective heat flux, x component	Domain 8
ht3.cfluxy	ht3.rho*ht3.uy*ht3.Ei	W/m^2	Convective heat flux, y component	Domain 8

Name	Expression	Unit	Description	Selection
ht3.cfluxz	ht3.rho*ht3.uz*ht3.Ei	W/m^2	Convective heat flux, z component	Domain 8
ht3.cfluxMag	sqrt(ht3.cfluxx^2+ht3.cfluxy^2+ht3.cfluxz^2)	W/m^2	Convective heat flux magnitude	Domain 8
ht3.tfluxx	ht3.dfluxx+ht3.trlfluxx+ht3.cfluxx	W/m^2	Total heat flux, x component	Domain 8
ht3.tfluxy	ht3.dfluxy+ht3.trlfluxy+ht3.cfluxy	W/m^2	Total heat flux, y component	Domain 8
ht3.tfluxz	ht3.dfluxz+ht3.trlfluxz+ht3.cfluxz	W/m^2	Total heat flux, z component	Domain 8
ht3.tfluxMag	sqrt(ht3.tfluxx^2+ht3.tfluxy^2+ht3.tfluxz^2)	W/m^2	Total heat flux magnitude	Domain 8
ht3.tefluxx	ht3.dfluxx+ht3.rho*ht3.ux*ht3.H0	W/m^2	Total energy flux, x component	Domain 8
ht3.tefluxy	ht3.dfluxy+ht3.rho*ht3.uy*ht3.H0	W/m^2	Total energy flux, y component	Domain 8
ht3.tefluxz	ht3.dfluxz+ht3.rho*ht3.uz*ht3.H0	W/m^2	Total energy flux, z component	Domain 8
ht3.tefluxMag	sqrt(ht3.tefluxx^2+ht3.tefluxy^2+ht3.tefluxz^2)	W/m^2	Total energy flux magnitude	Domain 8

Name	Expression	Unit	Description	Selection
ht3.rflux	0	W/m^2	Radiative heat flux	Boundaries 36–39, 41–43, 45–46
ht3.chflux	0	W/m^2	Boundary convective heat flux	Boundaries 36–39, 41–43, 45–46
ht3.ntrlflux	mean(ht3.trlfluxx)*ht3.nx+mean(ht3.trlfluxy)*ht3.ny+mean(ht3.trlfluxz)*ht3.nz	W/m^2	Normal translational heat flux	Boundaries 36–39, 41–43, 45–46
ht3.ntrlflux_u	up(ht3.trlfluxx)*ht3.unx+up(ht3.trlfluxy)*ht3.uny+up(ht3.trlfluxz)*ht3.unz	W/m^2	Internal normal translational heat flux, upside	Boundaries 36, 41–42, 46
ht3.ntrlflux_d	down(ht3.trlfluxx)*ht3.dnx+down(ht3.trlfluxy)*ht3.dny+down(ht3.trlfluxz)*ht3.dnz	W/m^2	Internal normal translational heat flux, downside	Boundaries 36, 41–42, 46
ht3.ncflux	mean(ht3.cfluxx)*ht3.nx+mean(ht3.cfluxy)*ht3.ny+mean(ht3.cfluxz)*ht3.nz	W/m^2	Normal convective heat flux	Boundaries 36–39, 41–43, 45–46

Name	Expression	Unit	Description	Selection
ht3.ncflux_u	up(ht3.cfluxx)*ht3.unx+up(ht3.cfluxy)*ht3.uny+up(ht3.cfluxz)*ht3.unz	W/m^2	Internal normal convective heat flux, upside	Boundaries 36, 41–42, 46
ht3.ncflux_d	down(ht3.cfluxx)*ht3.dnx+down(ht3.cfluxy)*ht3.dny+down(ht3.cfluxz)*ht3.dnz	W/m^2	Internal normal convective heat flux, downside	Boundaries 36, 41–42, 46
ht3.ndflux	-dflux_spatial(T)/ht3.d	W/m^2	Normal conductive heat flux	Boundaries 37–39, 43, 45
ht3.ndflux	0.5*(uflux_spatial(T)-dflux_spatial(T))/ht3.d	W/m^2	Normal conductive heat flux	Boundaries 36, 41–42, 46
ht3.ndflux_u	-uflux_spatial(T)/ht3.d	W/m^2	Internal normal conductive heat flux, upside	Boundaries 36, 41–42, 46
ht3.ndflux_d	-dflux_spatial(T)/ht3.d	W/m^2	Internal normal conductive heat flux, downside	Boundaries 36, 41–42, 46
ht3.ntflux	ht3.ndflux+ht3.ntrlflux+ht3.ncflux	W/m^2	Normal total heat flux	Boundaries 36–39, 41–43, 45–46
ht3.ntflux_u	ht3.ndflux_u+ht3.ntrlflux_u+ht3.ncflux_u	W/m^2	Internal normal total flux, upside	Boundaries 36, 41–42, 46

Name	Expression	Unit	Description	Selection
ht3.ntflux_d	ht3.ndflux_d+ht3.ntrlflux_d+ht3.ncflux_d	W/m^2	Internal normal total flux, downside	Boundaries 36, 41–42, 46
ht3.nteflux	mean(ht3.tefluxx)*ht3.nx+mean(ht3.tefluxy)*ht3.ny+mean(ht3.tefluxz)*ht3.nz-mean(ht3.dfluxx)*ht3.nx-mean(ht3.dfluxy)*ht3.ny-mean(ht3.dfluxz)*ht3.nz+ht3.ndflux	W/m^2	Normal total energy flux	Boundaries 36–39, 41–43, 45–46
ht3.nteflux_u	up(ht3.tefluxx)*ht3.unx+up(ht3.tefluxy)*ht3.uny+up(ht3.tefluxz)*ht3.unz-up(ht3.dfluxx)*ht3.unx-up(ht3.dfluxy)*ht3.uny-up(ht3.dfluxz)*ht3.unz+ht3.ndflux_u	W/m^2	Internal normal total energy flux, upside	Boundaries 36, 41–42, 46
ht3.nteflux_d	down(ht3.tefluxx)*ht3.dnx+down(ht3.tefluxy)*ht3.dny+down(ht3.teflux	W/m^2	Internal normal total energy flux, downside	Boundaries 36, 41–42, 46

Name	Expression	Unit	Description	Selection
	z)*ht3.dnz-down(ht3.dfluxx)*ht3.dnx-down(ht3.dfluxy)*ht3.dny-down(ht3.dfluxz)*ht3.dnz+ht3.ndflux_d			
ht3.c_s	sqrt(ht3.gamma/max(subst(d(ht3.rhoInt,ht3.pA),ht3.pA,model.input.minput_pressure),eps))	m/s	Speed of sound	Domain 8
ht3.Ma	sqrt(model.input.minput_velocity1^2+model.input.minput_velocity2^2+model.input.minput_velocity3^2)/ht3.c_s	1	Mach number	Domain 8
ht3.cellPe	0.5*ht3.rho*ht3.Cp*h*sqrt(ht3.ux^2+ht3.uy^2+ht3.uz^2)/ht3.kmean	1	Cell Péclet number	Domain 8
ht3.k_eqxx	ht3.theta_p*ht3.k_pxx+(1-	W/(m*K)	Equivalent thermal conductivity, xx component	Domain 8

Name	Expression	Unit	Description	Selection
	ht3.theta_p)*ht3.kxx+ht3.k_dispxx			
ht3.k_eqyx	ht3.theta_p*ht3.k_pyx+(1-ht3.theta_p)*ht3.kyx+ht3.k_dispyx	W/(m*K)	Equivalent thermal conductivity, yx component	Domain 8
ht3.k_eqzx	ht3.theta_p*ht3.k_pzx+(1-ht3.theta_p)*ht3.kzx+ht3.k_dispzx	W/(m*K)	Equivalent thermal conductivity, zx component	Domain 8
ht3.k_eqxy	ht3.theta_p*ht3.k_pxy+(1-ht3.theta_p)*ht3.kxy+ht3.k_dispxy	W/(m*K)	Equivalent thermal conductivity, xy component	Domain 8
ht3.k_eqyy	ht3.theta_p*ht3.k_pyy+(1-ht3.theta_p)*ht3.kyy+ht3.k_dispyy	W/(m*K)	Equivalent thermal conductivity, yy component	Domain 8
ht3.k_eqzy	ht3.theta_p*ht3.k_pzy+(1-ht3.theta_p)*ht3.kzy+ht3.k_dispzy	W/(m*K)	Equivalent thermal conductivity, zy component	Domain 8

Name	Expression	Unit	Description	Selection
ht3.k_eqxz	ht3.theta_p*ht3.k_pxz+(1-ht3.theta_p)*ht3.kxz+ht3.k_dispxz	W/(m*K)	Equivalent thermal conductivity, xz component	Domain 8
ht3.k_eqyz	ht3.theta_p*ht3.k_pyz+(1-ht3.theta_p)*ht3.kyz+ht3.k_dispyz	W/(m*K)	Equivalent thermal conductivity, yz component	Domain 8
ht3.k_eqzz	ht3.theta_p*ht3.k_pzz+(1-ht3.theta_p)*ht3.kzz+ht3.k_dispzz	W/(m*K)	Equivalent thermal conductivity, zz component	Domain 8
ht3.C_eq	ht3.theta_p*ht3.rho_p*ht3.Cp_p+(1-ht3.theta_p)*ht3.rho*ht3.Cp	J/(m^3*K)	Equivalent volumetric heat capacity	Domain 8
ht3.k_dispxx	0	W/(m*K)	Thermal dispersion coefficient, xx component	Domain 8
ht3.k_dispyx	0	W/(m*K)	Thermal dispersion coefficient, yx component	Domain 8

Name	Expression	Unit	Description	Selection
ht3.k_dispzx	0	W/(m*K)	Thermal dispersion coefficient, zx component	Domain 8
ht3.k_dispxy	0	W/(m*K)	Thermal dispersion coefficient, xy component	Domain 8
ht3.k_dispyy	0	W/(m*K)	Thermal dispersion coefficient, yy component	Domain 8
ht3.k_dispzy	0	W/(m*K)	Thermal dispersion coefficient, zy component	Domain 8
ht3.k_dispxz	0	W/(m*K)	Thermal dispersion coefficient, xz component	Domain 8
ht3.k_dispyz	0	W/(m*K)	Thermal dispersion coefficient, yz component	Domain 8
ht3.k_dispzz	0	W/(m*K)	Thermal dispersion coefficient, zz component	Domain 8
ht3.helem	h	m	Element size	Domain 8

Name	Expression	Unit	Description	Selection
ht3.res_T	-ht3.k_effxx*Txx-ht3.k_effxy*Txy-ht3.k_effxz*Txz-ht3.k_effyx*Tyx-ht3.k_effyy*Tyy-ht3.k_effyz*Tyz-ht3.k_effzx*Tzx-ht3.k_effzy*Tzy-ht3.k_effzz*Tzz-(ht3.qs+ht3.qs_oop)*T+ht3.rho*ht3.Cp*(ht3.ux*Tx+ht3.uy*Ty+ht3.uz*Tz)-ht3.Q-ht3.Qoop	W/m^3	Equation residual	Domain 8
ht3.porous5.pRef	model.input.pRef	Pa	Reference pressure level	Domain 8
ht3.porous5.dEiInt	ht3.porous5.intDom(d(ht3.rho*ht3.Ei,t)*ht3.porous5.varIntSpa)	W	Total accumulated heat rate	Global
ht3.porous5.dEi0Int	ht3.porous5.intDom(d(ht3.rho*ht3.Ei0,t)*ht3.porous5.varIntSpa)	W	Total accumulated energy rate	Global

Name	Expression	Unit	Description	Selection
ht3.porous5.ntfluxInt	ht3.porous5.intExtBnd(ht3.ntflux*ht3.porous5.varIntSpa)+ht3.porous5.intExtBndUp(ht3.ntflux_u*ht3.porous5.varIntSpa)+ht3.porous5.intExtBndDown(ht3.ntflux_d*ht3.porous5.varIntSpa)	W	Total net heat rate	Global
ht3.porous5.ntefluxInt	ht3.porous5.intExtBnd(ht3.nteflux*ht3.porous5.varIntSpa)+ht3.porous5.intExtBndUp(ht3.nteflux_u*ht3.porous5.varIntSpa)+ht3.porous5.intExtBndDown(ht3.nteflux_d*ht3.porous5.varIntSpa)	W	Total net energy rate	Global
ht3.porous5.QInt	ht3.porous5.intDom(ht3.Qtot*ht3.porous5.varIntSpa)-ht3.porous5.intIntBnd((ht3.ndflux_u+ht3.ndflux_d)*ht3.porous5.varIntSpa)	W	Total heat source	Global

Name	Expression	Unit	Description	Selection
ht3.porous5.WnsInt	ht3.porous5.intDom(ht3.pA*(d(ht3.ux,x)+d(ht3.uy,y)+d(ht3.uz,z))*ht3.porous5.varIntSpa)	W	Total work source	Global
ht3.porous5.WInt	0	W	Total work source	Global

A.1.6 Shape functions

Name	Shape function	Unit	Description	Shape frame	Selection
T	Lagrange (Linear)	K	Temperature	Material	Domain 8

A.1.7 Weak expressions

Weak expression	Integration order	Integration frame	Selection
(-(ht3.k_effxx*Tx+ht3.k_effxy*Ty+ht3.k_effxz*Tz)*test(Tx)-(ht3.k_effyx*Tx+ht3.k_effyy*Ty+ht3.k_effyz*Tz)*test(Ty)-(ht3.k_effzx*Tx+ht3.k_effzy*Ty+ht3.k_effzz*Tz)*test(Tz))*ht3.d	2	Material	Domain 8

Weak expression	Integration order	Integration frame	Selection
- ht3.rho*ht3.Cp*(ht3.ux*Tx+ht3.uy*T y+ht3.uz*Tz)*test(T)*ht3.d	2	Material	Domain 8
ht3.crosswind	2	Material	Domain 8
ht3.streamline	2	Material	Domain 8

A.2 Heat Source CCL

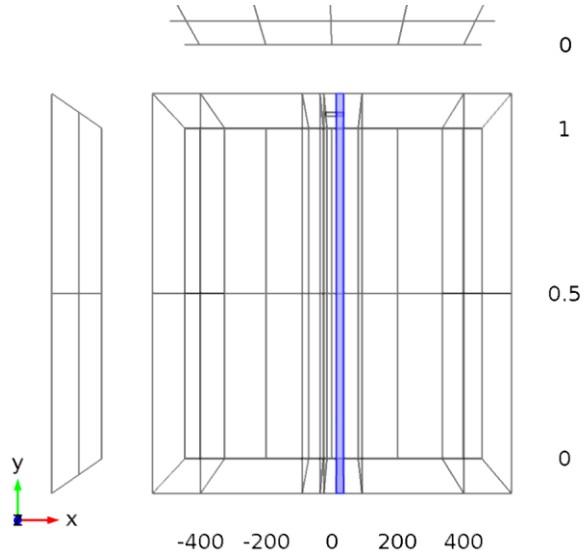

Figure 43: Heat Source CCL

A.2.1 Selection

Geometric entity level	Domain
Selection	Domain 8

A.2.2 Equations

$$Q = Q_0$$

A.2.3 Settings

Description	Value
Heat source	General source
Heat source	User defined
Heat source	s_rev_ccl + s_irrev_ccl + s_sorp

A.2.4 Variables

Name	Expression	Unit	Description	Selection
ht3.Q	ht3.hs2.Q	W/m^3	Heat source	Domain 8
ht3.Qtot	ht3.hs2.Q	W/m^3	Total heat source	Domain 8
ht3.hs2.Q	s_rev_ccl+s_irrev_ccl+s_sorp	W/m^3	Heat source	Domain 8

A.2.5 Weak expressions

Weak expression	Integration order	Integration frame	Selection
ht3.hs2.Q*test(T)*ht3.d	2	Material	Domain 8

A.3 Two-Phase Darcy Law: Fluid and Matrix Properties CCL

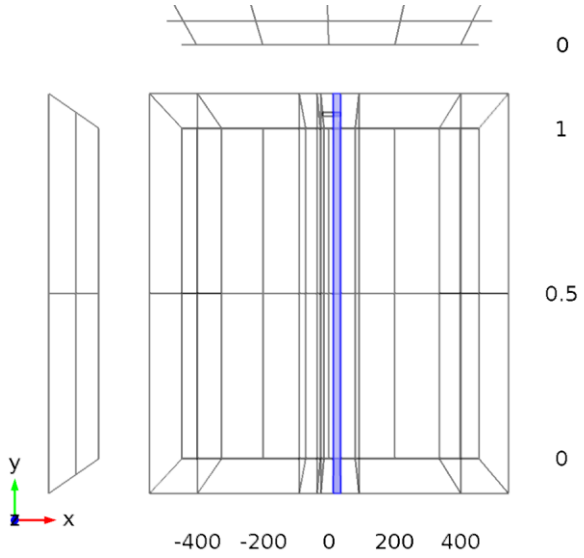

Figure 44: Fluid and Matrix Properties CCL

A.3.1 Selection

Geometric entity level	Domain
Selection	Domains 8–9

A.3.2 Equations

$$\nabla \cdot (\rho \mathbf{u}) = 0, \quad \mathbf{u} = -\frac{\kappa}{\mu} p$$

$$\rho = s_1 \rho_1 + s_2 \rho_2, \quad \frac{1}{\mu} = s_1 \frac{\kappa_{r1}}{\mu_1} + s_2 \frac{\kappa_{r2}}{\mu_2}, \quad s_1 + s_2 = 1$$

$$\nabla \cdot (c1\mathbf{u}) = \nabla \cdot (D_c \nabla c1), \quad c1 = s_1 \rho_1$$

$$D_c = \frac{\kappa_{r1}}{\mu_1}\kappa(s_1 - 1)\frac{\partial p_c}{\partial s_1}$$

A.3.3 Settings

Description	Value
Relative permeability	(tpdl.s1)^2.16
Relative permeability	(1 - tpdl.s1)^2.16
Fluid 1	Water (mat9)
Density	From material
Dynamic viscosity	From material
Fluid 2	Air (mat7)
Density	From material
Dynamic viscosity	From material
Porous material	PTL (mat5)
Porosity	User defined
Porosity	1 - phi_ccl
Permeability	User defined
Permeability	{{k_abs_ccl, 0, 0}, {0, k_abs_ccl, 0}, {0, 0, k_abs_ccl}}
Capillary model	Capillary pressure
Pressure model	User defined
Capillary pressure	J_ccl*gamma*cos(theta_ccl)*sqrt((1 - phi_ccl)/k_abs_ccl)

Description	Value
Capillary diffusion , xx component	{{1e-6[m^2/s], 0, 0}, {0, 1e-6[m^2/s], 0}, {0, 0, 1e-6[m^2/s]}}

A.3.4 Properties from material

Property	Material	Property group
Density	Air	Basic
Dynamic viscosity	Air	Basic
Density	Water	Basic
Dynamic viscosity	Water	Basic

A.3.5 Variables

Name	Expression	Unit	Description	Selection
tpdl.ux	(-tpdl.kappaxx*px-tpdl.kappaxy*py-tpdl.kappaxz*pz)/tpdl.mu	m/s	Velocity field, x component	Domains 8–9
tpdl.uy	(-tpdl.kappayx*px-tpdl.kappayy*py-tpdl.kappayz*pz)/tpdl.mu	m/s	Velocity field, y component	Domains 8–9
tpdl.uz	(-tpdl.kappazx*px-tpdl.kappazy*py-tpdl.kappazz*pz)/tpdl.mu	m/s	Velocity field, z component	Domains 8–9

Name	Expression	Unit	Description	Selection
tpdl.U	sqrt(tpdl.ux^2+tpdl.uy^2+tpdl.uz^2)	m/s	Velocity magnitude	Domains 8–9
tpdl.s1	min(max(eps,c1/tpdl.rho1),1-eps)	1	Saturation fluid 1	Domains 8–9
tpdl.s2	1-tpdl.s1	1	Saturation fluid 2	Domains 8–9
tpdl.rho1	material.rho1	kg/m^3	Density	Domains 8–9
tpdl.mu1	material.mu1	Pa*s	Dynamic viscosity	Domains 8–9
tpdl.kappar1	tpdl.s1^2.16	1	Relative permeability	Domains 8–9
tpdl.rho2	material.rho2	kg/m^3	Density	Domains 8–9
tpdl.mu2	material.mu2	Pa*s	Dynamic viscosity	Domains 8–9
tpdl.kappar2	(1-tpdl.s1)^2.16	1	Relative permeability	Domains 8–9
tpdl.rho	tpdl.s1*tpdl.rho1+tpdl.s2*tpdl.rho2	kg/m^3	Average density	Domains 8–9
tpdl.mu	1/(tpdl.s1*tpdl.kappar1/tpdl.mu1+tpdl.s2*tpdl.kappar2/tpdl.mu2)	Pa*s	Average dynamic viscosity	Domains 8–9
tpdl.epsilon	1-phi_ccl	1	Porosity	Domains 8–9
tpdl.kappaxx	k_abs_ccl	m^2	Permeability, xx component	Domains 8–9

Name	Expression	Unit	Description	Selection
tpdl.kappayx	0	m^2	Permeability, yx component	Domains 8–9
tpdl.kappazx	0	m^2	Permeability, zx component	Domains 8–9
tpdl.kappaxy	0	m^2	Permeability, xy component	Domains 8–9
tpdl.kappayy	k_abs_ccl	m^2	Permeability, yy component	Domains 8–9
tpdl.kappazy	0	m^2	Permeability, zy component	Domains 8–9
tpdl.kappaxz	0	m^2	Permeability, xz component	Domains 8–9
tpdl.kappayz	0	m^2	Permeability, yz component	Domains 8–9
tpdl.kappazz	k_abs_ccl	m^2	Permeability, zz component	Domains 8–9
tpdl.pc	J_ccl*gamma*cos(theta_ccl)*sqrt((1-phi_ccl)/k_abs_ccl)	Pa	Capillary pressure	Domains 8–9
tpdl.Dcxx	max(tpdl.kappar1,eps)*tpdl.kappaxx*(-1+tpdl.s1)*pd(tpdl.pc,tpdl.s1)/tpdl.mu1	m^2/s	Capillary diffusion , xx component	Domains 8–9

Name	Expression	Unit	Description	Selection
tpdl.Dcyx	max(tpdl.kappar1,eps)*tpdl.kappayx*(-1+tpdl.s1)*pd(tpdl.pc,tpdl.s1)/tpdl.mu1	m^2/s	Capillary diffusion , yx component	Domains 8–9
tpdl.Dczx	max(tpdl.kappar1,eps)*tpdl.kappazx*(-1+tpdl.s1)*pd(tpdl.pc,tpdl.s1)/tpdl.mu1	m^2/s	Capillary diffusion , zx component	Domains 8–9
tpdl.Dcxy	max(tpdl.kappar1,eps)*tpdl.kappaxy*(-1+tpdl.s1)*pd(tpdl.pc,tpdl.s1)/tpdl.mu1	m^2/s	Capillary diffusion , xy component	Domains 8–9
tpdl.Dcyy	max(tpdl.kappar1,eps)*tpdl.kappayy*(-1+tpdl.s1)*pd(tpdl.pc,tpdl.s1)/tpdl.mu1	m^2/s	Capillary diffusion , yy component	Domains 8–9
tpdl.Dczy	max(tpdl.kappar1,eps)*tpdl.kappazy*(-1+tpdl.s1)*pd(tpdl.pc,tpdl.s1)/tpdl.mu1	m^2/s	Capillary diffusion , zy component	Domains 8–9
tpdl.Dcxz	max(tpdl.kappar1,eps)*tpdl.kappaxz*(-1+tpdl.s1)*pd(tpdl.pc,tpdl.s1)/tpdl.mu1	m^2/s	Capillary diffusion , xz component	Domains 8–9

Name	Expression	Unit	Description	Selection
tpdl.Dcyz	max(tpdl.kappar1,eps)*tpdl.kappayz*(-1+tpdl.s1)*pd(tpdl.pc,tpdl.s1)/tpdl.mu1	m^2/s	Capillary diffusion , yz component	Domains 8–9
tpdl.Dczz	max(tpdl.kappar1,eps)*tpdl.kappazz*(-1+tpdl.s1)*pd(tpdl.pc,tpdl.s1)/tpdl.mu1	m^2/s	Capillary diffusion , zz component	Domains 8–9

A.3.6 Shape functions

Name	Shape function	Unit	Description	Shape frame	Selection
P	Lagrange (Quadratic)	Pa	Pressure	Material	Domains 8–9
c1	Lagrange (Linear)	kg/m^3	Fluid content 1	Material	Domains 8–9

A.3.7 Weak expressions

Weak expression	Integration order	Integration frame	Selection
-d(tpdl.epsilon*tpdl.rho,t)*test(p)+tpdl.rho*tpdl.ux*test(px)+tpdl.rho*tpdl.uy*test(py)+tpdl.rho*tpdl.uz*test(pz)	4	Material	Domains 8–9

Weak expression	Integration order	Integration frame	Selection
-d(tpdl.epsilon*c1,t)*test(c1)+test(c1x)*c1*tpdl.ux+test(c1y)*c1*tpdl.uy+test(c1z)*c1*tpdl.uz-test(c1x)*(tpdl.Dcxx*c1x+tpdl.Dcxy*c1y+tpdl.Dcxz*c1z)-test(c1y)*(tpdl.Dcyx*c1x+tpdl.Dcyy*c1y+tpdl.Dcyz*c1z)-test(c1z)*(tpdl.Dczx*c1x+tpdl.Dczy*c1y+tpdl.Dczz*c1z)	4	Material	Domains 8–9
tpdl.streamline*(isScalingSystemDomain==0)	4	Material	Domains 8–9

A.4 Uncharged Species distribution

Transport of concentrated species has been used on COMSOL because a solute-solvent relationship is inexistent since all the concentration of all species are of the same order of magnitude. The mass fraction of uncharged species (H_2, O_2, H_2O, N_2) is considered here.

Maxwell- Stefan Diffusion model will be considered since we have 4 components in total and it accounts for interactions of all species in a solution unlike Fick's law, one-way solute-solvent iterations.

On the cathode side, we have 3 components: O_2, H_2O, N_2, hence there are three pair-wise Fick analogous Maxwell-Stefan analogous diffusion coefficients $D_{O2\text{-}H2O}$, $D_{O2\text{-}N2}$, $D_{H2O\text{-}N2}$

On the anode side, we have 2 components: H_2, N_2, hence there is only one pair-wise Fick analogous Maxwell-Stefan analogous diffusion coefficient $D_{H2\text{-}H2O}$

Steady-state is assumed in this study

The layers into considerations are the PTL, MPL, CCL, ACL, Channels. Ribs and membrane does not allow diffusion of the components. In the presence of pinholes, there will be a diffusion flux through the pinhole in the membrane

A.4.1 Mass transport equation

The following mass transport equation are obtained by taking divergence of the mass flux through the diffusion and convection[103]:

$$\nabla \cdot \left[-\rho \omega_i \sum_{j=1}^{N} \tilde{D}_{ij} \left\{ \frac{M}{M_j} \left(\nabla \omega_j + \omega_j \frac{\nabla M}{M} \right) + (x_j - \omega_j) \frac{\nabla p}{p} \right\} + \omega_i \rho \mathbf{u} \right] = 0$$

M: Total mass of mixture (kg/mol)

M_j: Molar mass of species j (kg/mol)

ω_j: mass fraction of species j

x_j: mol fraction of species j

D_{ij}: Maxwell Stefan Diffusivities (m^2/s). These are given by the following empirical equation based on the kinetic gas theory and using Molecular volumes[103][1]:

$$D_{ij} = k\frac{T^{1.75}}{p(\nu_i^{1/3} + \nu_j^{1/3})^2}\left[\frac{1}{M_i} + \frac{1}{M_j}\right]^{1/2}$$

Where constant k: 3.16 x 10^{-8} $Pa.m^2/s$

T: Temperature (K)

p: Pressure(Pa)

M_j: Molar mass of species j (kg/mol)

v_j: molar diffusion volume of species j (m^3/mol).

At the cathode side, these are:

v_{O2}: m^3/mol

v_{H2O}: m^3/mol

v_{N2}: m^3/mol

At the anode side, these are:

v_{H2}: m^3/mol

v_{H2O}: m^3/mol

A.4.2 Boundary Conditions at the cathode side

Oxygen is consumed at the reactive interface at the cathode catalyst layer and membrane, where the flux of oxygen is given by:

$$\mathbf{n}_{O_2} \cdot \mathbf{n} = \left(-\frac{i_c}{4F}\right) M_{O_2}$$

Where,

n_j: mass flux of species j

i_c: local current given by Butler-Voltmer simplification, that is the Tafel expression;

$$i_c = \left(-\frac{S_a \delta i_0}{4F}\right) \frac{\omega_{O2}}{\omega_{O2_0}} \exp\left(\frac{0{,}5F\eta}{RT}\right).$$

Where,

S_a: Specific surface area(m^2/m^3)

δ_{io}: Thickness of the active layer(m)

F: Faraday's Number(C/mol)

R: Gas Constant(J/ mol K)

i_o: Exchange current density (A/m^2)

η: Overpotential

Mass fraction with the subscript zero is at the reference state.

Flux (mass) of water is given by,

$$\mathbf{n}_{H2O} \cdot \mathbf{n} = \frac{i_c}{F}\left(\frac{1}{2} + t_{H_2O}\right) M_{H_2O}$$

Where t_{H2O}: is the number of water molecules dragged with each proton migrating through the membrane.

There is no flux of nitrogen at the reactive interface since it is inert.

The gas velocity is given by:

$$\mathbf{u} = \left(-\frac{1}{\omega_{N_2}\rho}\right)\nabla\cdot\left[-\left(\rho\omega_{N_2}\sum_{j=1}^{IV} D_{N_2,j}\left\{\frac{M}{M_j}\left(\nabla\omega_j + \omega_j\frac{\nabla M}{M}\right) + (x_j - \omega_j)\frac{\nabla p}{p}\right\}\right)\right]$$

The inlet gas composition at the channels, by considering air saturated with steam at 80 ^{o}C, is applies as:

ω_{H2O_0}: 0.4764

ω_{N2_0}: 0.3789

ω_{O2_0}: 0.1447

A.4.3 Boundary Conditions at the anode side

Same as cathode except for value of number of electrons taking part in reaction at anode and that water is dragged from the anode catalyst layer to the Nafion membrane but no water is produced there.

A.4.4 Pinhole heat generation

Pinhole heat generation [W/m^2]

=Molar diffusion flux of limiting reactant [mol/m^2 s] x Heat of combustion between reactant and oxidant [KJ/mol]